



**HAL**  
open science

# Magnetron sputtered ZnO layers : synthesis, characterization and oxygen reduction investigations

Josiane Soares Costa

► **To cite this version:**

Josiane Soares Costa. Magnetron sputtered ZnO layers : synthesis, characterization and oxygen reduction investigations. Physics [physics]. Université de Bretagne occidentale - Brest, 2019. English. NNT : 2019BRES0037 . tel-02518586

**HAL Id: tel-02518586**

**<https://theses.hal.science/tel-02518586v1>**

Submitted on 25 Mar 2020

**HAL** is a multi-disciplinary open access archive for the deposit and dissemination of scientific research documents, whether they are published or not. The documents may come from teaching and research institutions in France or abroad, or from public or private research centers.

L'archive ouverte pluridisciplinaire **HAL**, est destinée au dépôt et à la diffusion de documents scientifiques de niveau recherche, publiés ou non, émanant des établissements d'enseignement et de recherche français ou étrangers, des laboratoires publics ou privés.

# THESE DE DOCTORAT DE

L'UNIVERSITE  
DE BRETAGNE OCCIDENTALE  
COMUE UNIVERSITE BRETAGNE LOIRE

ECOLE DOCTORALE N° 596  
*Matière, Molécules, Matériaux*  
Spécialité : Physique

Par

**Josiane SOARES COSTA**

**Magnetron sputtered ZnO layers : Synthesis, characterization and oxygen reduction investigations**

Thèse présentée et soutenue à Brest, le 12 juin 2019  
Unité de recherche : UMR 6285 LabSTICC

## Rapporteurs avant soutenance :

Nadine PEBERE Directrice de recherche CNRS, CIRIMAT, Toulouse  
Kévin OGLE Professeur, Chimie-Paris-Tech, PSL Université, Paris

## Composition du Jury :

Président : Bernard TRIBOLLET  
Examineurs : Nadine PEBERE  
Kévin OGLE  
Dominique THIERRY  
Dir. de thèse : Stéphane RIOUAL  
Co-dir. de thèse : Michel PRESTAT  
**Invité(s)**

Directeur de Recherche émérite LISE, Sorbonne Université, Paris  
Directrice de Recherche CNRS, CIRIMAT, Toulouse  
Professeur, Chimie-Paris-Tech, PSL Université, Paris  
Directeur, Institut de la Corrosion, Brest  
Université de Bretagne Occidentale, Brest  
Ingénieur de Recherche, Institut de la Corrosion, Brest

Benoît LESCOP

Université de Bretagne Occidentale, Brest



## Acknowledgments

---

Firstly, I would like to express my gratitude to Professor Dominique Thierry for giving me the opportunity to carry out my Ph.D. thesis within the French Corrosion Institute in Brest.

I would like to thank my academic supervisors, Dr. Stephane Rioual and Dr. Benoit Lescop from the Université of Bretagne Occidentale (UBO), for welcoming me in their group and introducing me to the fields of thin film synthesis and surface characterization analysis.

Many thanks to Dr. Michel Prestat, my supervisor at the French Corrosion Institute, for his guidance during this Ph.D. adventure and for teaching me electrochemistry in the lab and in the office.

I would also like to thank Dr. Bernard Tribollet, for his great support throughout the Ph.D. thesis, for sharing with me his huge knowledge of electrochemical impedance spectroscopy and for proof-reading the thesis manuscript. Dear Bernard, working with you was a pleasure, thank you for everything.

I am deeply grateful to Dr. Nadine Pébère (CIRIMAT, Toulouse) and Professor Kevin Ogle (Chimie ParisTech) who accepted to referee this Ph.D. thesis.

My warmest thanks also go to:

- Xavier Castel (professor at IETR) and Frederic Glouaguen (Research Director at CEMCA) for having accepted to participate as scientific members of the “Comité de Suivi Individuel”.

- Dr. Holzer Lorenz (Zurich University of Applied Sciences, Winterthur, Switzerland) for his valuable FIB-SEM and HAADF-STEM images and analyses. The technical support of the team of ScopeM (electron microscopy centre of ETH Zurich, Switzerland) is also gratefully acknowledged.

- Dr. Flavien Vucko (French Corrosion Institute) for training and help me with our in-house scanning electron microscope.

- Anne Le Gac (French Corrosion Institute) for her precious help and advices with the preparation and polishing of metal substrates.

- All my colleagues of the French Corrosion Institute (with special thanks to Fabienne, Krystel and Adrien) and UBO I had the good fortune to meet during the three years of this Ph.D. thesis.

Finally, I owe thanks to my family and friends who gave me a considerable emotional support (even remotely) and encouragements during my pursuit of Ph.D. degree that made the completion of thesis possible.

**Thank you! Merci beaucoup! Muito obrigada!**

The financial support of the “Association Nationale de la Recherche et de la Technologie” (ANRT, Paris, France) through the CIFRE contract #2016/0066 is gratefully acknowledged.

*“Never give up on what you really want to do. The person with big dreams is more powerful than the one with all the facts”.*

***Albert Einstein***

## Summary

---

<b>Chapter 1: Introduction and State-of-the-art of ORR on zinc (Zn) and Zinc oxide (ZnO)</b>	8
1.1. General aspects of corrosion .....	8
1.2. Zinc corrosion and zinc oxide .....	10
1.3. Oxygen reduction reaction (ORR) .....	12
1.4. State of the art of ORR on zinc and zinc oxide .....	13
1.5. Aim of the work and structure of the thesis .....	17
1.6 References .....	18
<b>Chapter 2: Experimental Techniques – Theory and Setups</b>	25
2.1. Substrate preparation .....	25
2.2. Sputtering technique .....	25
2.2.1. Deposition process .....	25
2.2.2. Structure of thin films deposited by sputtering .....	28
2.2.3. Sputtering setup .....	31
2.3. Electrochemical techniques .....	31
2.3.1 Rotating disk electrode (RDE) .....	31
2.3.2. Rotating ring disk electrode (RRDE) .....	34
2.3.3. Rotating disk electrode (RDE) and Rotating ring disk electrode (RRDE) setups ...	36
2.4. Electrochemical Impedance Spectroscopy (EIS) .....	36
2.4.1. Impedance definition: concept of complex impedance .....	36
2.4.2. Electrochemical Impedance Spectroscopy (EIS) setup .....	43
2.5. Surface characterization techniques .....	43
2.5.1. Atomic Force Microscopy (AFM) .....	43
2.5.2. Profilometer .....	44
2.5.3. X-ray diffraction (XRD) .....	44
2.5.4. Scanning Electron Microscopy (SEM) .....	45
2.5.5. Scanning transmission electron microscope (STEM) .....	47
2.5.6. Energy Dispersive spectroscopy (EDS) .....	47
2.5.7. Focused ion beam (FIB) .....	48
2.5.8. X-ray Photoelectron Spectroscopy (XPS) .....	49
2.6. References .....	50

<b>Chapter 3: DC study of ORR on textured ZnO layer</b>	54
3.1. Introduction .....	54
3.2. Experimental .....	56
3.2.1 Synthesis of the ZnO layers .....	56
3.2.2 Characterization of the ZnO layers .....	56
3.2.3 Electrochemical measurements .....	57
3.3. Results and discussion .....	57
3.3.1 Film characterization .....	57
3.3.2 Electrochemical behaviour .....	60
3.4. Conclusions .....	65
3.5. References .....	66
<b>Annex I – Additional information of Chapter 3</b>	69
<b>Chapter 4: Impedance analysis of the degradation of textured ZnO films</b>	73
4.1. Introduction .....	73
4.2. Experimental Section .....	74
4.2.1. Synthesis and characterization of the ZnO layers .....	74
4.2.2. Electrochemical measurements .....	75
4.3. Results and discussion .....	76
4.3.1 Physical characterization of the ZnO layers .....	76
4.3.2. Electrochemical results .....	77
4.4. Conclusions .....	87
4.5. References .....	88
<b>Chapter 5: Microstructural and electrochemical investigations on non-textured ZnO layers</b>	90
5.1. Introduction .....	90
5.2. Experimental Section .....	92
5.2.1. Synthesis of the ZnO layers .....	92
5.2.2. Characterization of the ZnO layers .....	93
5.2.3. Electrochemical measurements .....	94
5.3. Results and discussion .....	94
5.4. Conclusions .....	116
5.5. References .....	117
<b>Chapter 6: Conclusions and outlook</b>	120
<b>Annex II</b>	128



### Abstract

Oxygen reduction is the most common fundamental reaction with some applications for photocatalysis and corrosion. In the present chapter, we consider the corrosion of zinc leading to the formation of ZnO. After describing properties of ZnO and the general oxygen reduction mechanism, an extensive review of ORR on Zn/ZnO surface is presented.

### 1.1. General aspects of corrosion

Corrosion of metals affects many domains of industry. Its economic impact is of considerable importance, about 3 or 4% of gross domestic product in industrial countries [1,2]. Corrosion is a chemical term commonly used to refer the process of total, partial, superficial or structural destruction of a given material (usually metals) caused by the aggressive influence of the environment. It is a complex electrochemical process. Many metals corrode when they are exposed to high relative humidity in air. Moreover, the process is also strongly affected by exposure to certain substances (acid or alkaline species, pollutants, chloride, bacteria...). Corrosion can be considered to modify the initial material locally at the micro or nanoscale or can extend across a wide area more or less uniformly, leading to localized or uniform types of corrosion. The presence of corroded species at the surface also plays an important role in the process and impacts strongly the material's corrosion resistance.

There are different forms of corrosion, among the most important [3-6]:

- **Uniform or generalized** corrosion is a (more or less) regular loss of material across the surface;
- **Galvanic or bimetallic** corrosion is due to the formation of a battery between two metals. The metal with the most negative corrosion potential plays the role of anode and therefore undergoes accelerated corrosion;
- **Cavernous** corrosion is due to a difference in oxygen accessibility between two parts of a structure, creating an electrochemical cell;

- **Pitting** corrosion is produced by some anions, especially halides and more particularly chlorides, in metals protected by very fine oxide films;
- **Corrosion under stress** is a metal saturation resulting from the joint action of mechanical stress and electrochemical reaction.

Fundamentally, it is a local electrochemical process which involves an oxidation reaction (e.g. the dissolution of the metal) balanced by a reduction reaction (most often the oxygen reduction) [3-5]. This means that fighting against corrosion can be oriented towards the inhibition of the oxidation reaction or the reduction reaction (or both simultaneously). The comprehension of the mechanisms and kinetics of both electrochemical reaction is thus of great interest.

For a metal M in near-neutral or alkaline electrolyte, the corrosion reactions can be written as follows:



The products of the reactions (1) and (2) react to form corrosion products can precipitate on the surface, as reaction 3:



An hydrolysis step might follow:



Those reactions are illustrated in Figure *I.1* in the case of zinc corrosion.

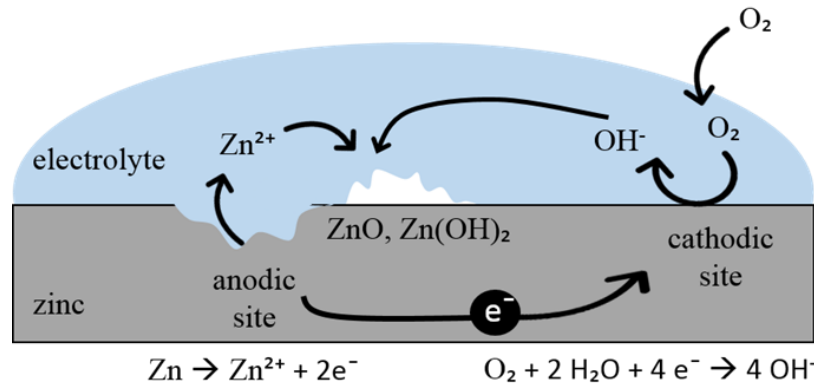


Figure 1.1: Basic principle of corrosion applied to zinc.

## 1.2. Zinc corrosion and zinc oxide

Zinc corrosion in the natural environment depends heavily on the composition of the environment [3-7]. The factors that determine the corrosivity of an atmosphere include industrial pollution, marine pollution, humidity, temperature (especially the spread between daily highs and lows that influence condensation and evaporation of moisture) and rainfall. Table 1.1 shows the zinc consumption measured in different environments reported by Graedel *et al.* [7].

In dry air, zinc is slowly attacked by atmospheric oxygen. A thin, dense layer of oxides is believed to form on the zinc surface, and outer layer then forms on top of it. Although outer layer breaks away occasionally, the under layer remains and protects the metal restricting its interaction with the oxygen. Under continued exposure, this film is transformed into various other atmospheric products. Zinc exposure in near neutral or alkaline electrolyte form: ZnO [8,9], Zn(OH)<sub>2</sub> [10,11], smithsonite ZnCO<sub>3</sub> [8,11] and hydrozincite Zn<sub>4</sub>CO<sub>3</sub>(OH)<sub>6</sub>.H<sub>2</sub>O [12,13]. In media containing low chloride and sulphate, respectively, the products formed are: simonkolleite Zn<sub>5</sub>(OH)<sub>8</sub>Cl<sub>2</sub> [10,13] and hydroxisulfates Zn<sub>4</sub>SO<sub>4</sub>(OH)<sub>6</sub>.nH<sub>2</sub>O [14,15].

Environments	Consumed zinc
Rural	0.2 to 3 μm / year
Urban	2 to 16 μm / year
Industrial	2 to 16 μm / year
Marine	0.5 to 8 μm / year

Table 1.1: Zinc atmospheric corrosion consumption in different environments [7].

ZnO is a material frequently found in the corrosion products of zinc. In the following, the property of this semiconducting material is presented.

Typically, the ZnO film is an n-type transparent semiconductor with a wide band gap of about 3.4 eV. The conductivity is strongly affected by defects and doping as detailed by A. Janotti *et al.* [16 and references therein]. Even relatively small concentrations of native point defects such as vacancies or doping can significantly affect the electrical and optical properties of semiconductors [16]. Therefore, depending on the synthesis method, thin films can present very different electronic resistivities.

ZnO films have different structures, the most common is the wurtzite type hexagonal (thermally stable structure at ambient conditions). However, there are also the cubic structures of zinc blende and rocksalt, as shown in Figure 1.2.

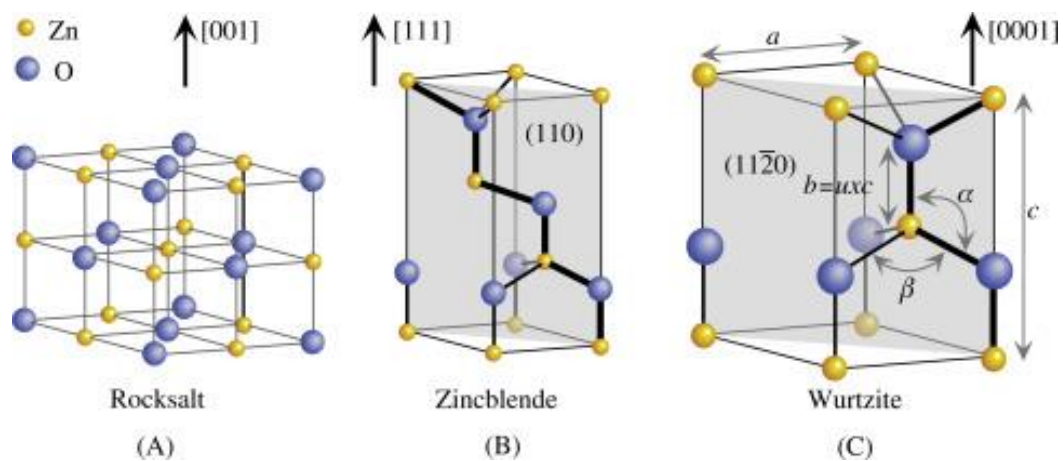


Figure 1.2: ZnO crystalline structures: (a) Rocksalt, (b) Zinc blende and (c) wurtzite [17].

The zinc blende structure can be stable only in epitaxial growth in cubic substrates and rocksalt is obtained only under relatively high pressures [18]. ZnO has a relatively open crystalline structure with a hexagonal network of dense packaging, in which the Zn atoms occupy half of the tetrahedral sites. All octahedral interstitial sites are empty and therefore many ZnO sites can accommodate intrinsic defects (particularly interstitial Zn) and extrinsic dopants [19]. In semiconductors the free surface energy, which affects the preferred orientation of each crystalline plane, depends strongly on the hybridized orbital.

The ZnO films tend to grow in the direction and plane of the lowest surface energy that is the direction [0001] and the plane (002). The ZnO synthesis can be done through several techniques including chemical and physical routes such as pulsed laser deposition

[20], thermal evaporation [21], chemical vapor deposition [22] and magnetron sputtering [23-32].

### 1.3. Oxygen reduction reaction (ORR)

The ORR is an important cathodic reaction in many different domains, such as biological respiration [33,34] fuel cells [35-37], metal-air batteries [38,39] and photocatalysis [40-43]. The interest for ORR gained momentum in the 1960's due to the development of fuel cells. It was generally observed that the kinetics and reduction mechanism depend on several factors: electrocatalytic material, type of electrolyte and particle size. Several models for ORR have been proposed and published [44-48].

Many ORR models have therefore been reported in the literature. However, there is an agreement on the occurrence of the following reaction steps:

- Direct pathway



- Indirect pathway



The reaction (5) involves four electrons and is known as the direct reduction of O<sub>2</sub>. It is in competition with the parallel indirect pathway that consists of two steps of two electrons (reactions (6) and (7)) involving the generation of hydrogen peroxide as intermediate species. The latter might chemically decomposes into oxygen. The production of hydrogen peroxide is a relevant aspect in corrosion since its oxidizing power may lead to the degradation of organic protective coatings (cathodic disbondment) [49-51].

The ORR mechanism is strongly dependent on the electrode material. The 4-electron pathway appears to be predominant in the case of several transition metals such as: Pt, Pd, Ag

and Ru, Cu and perovskite oxides [52]. In contrast, the indirect 2-electron pathway is the predominant path for different types of carbon, metals such as Au, Hg and in metallic oxides of Co and Ni [53,54].

The set of four steps presented above constitutes a basis ORR model that is actually utilized in the Chapters 3 and 5 of this Ph.D. thesis. Many authors have proposed more complex reactions mechanisms, involving forward and backward reactions with additional pathways [55-59]. However, the common point observed in all these cases is the competition between direct and indirect reduction.

Experimentally, the most frequently used techniques to investigate the ORR mechanism and kinetics are the rotating disk electrode (RDE) and rotating ring-disk electrode (RRDE) [60-63] because they allow to evaluate the average number of exchanged electrons per reduced oxygen molecule (RDE) and the relevance of the indirect pathway by measuring the amount of generated hydrogen peroxide (RRDE).

### 1.4. State of the art of ORR on zinc and zinc oxide

Though ZnO is one of the most common corrosion products of zinc, its electrochemical behavior is not well understood yet, in particular towards ORR. There is still a debate for results obtained in both immersion and atmospheric conditions, as recalled by Cole's recent review [64]. Different results were also obtained with native (passive) zinc oxide layers on bare zinc and thicker ZnO coatings (ca. hundreds of nanometers) that were artificially produced as well as under immersion or atmospheric conditions, as summarized in the next lines.

These dependence of the ORR mechanism on the passive/active state of zinc was first shown by Delahay [65] who observed the peroxide formation in zinc electrodes by a polarographic method in phosphate solution (pH 6.9). Their results indicate that, at cathodic potentials (-1 to -1.1 V vs. saturated calomel electrode) the oxygen can be reduced in 2-electrons pathway (indirect reduction with hydrogen peroxide as intermediate at low overpotentials) and direct reduction (4-electron pathway) when the potential is more negative.

The same trend was found in alkaline solutions by Wroblowa *et al.* [60,66] and Dafydd *et al.* [67] under controlled hydrodynamic conditions (using the rotating ring disk electrode and the rotating disk electrode, respectively). Using RRDE in 0.05 M NaCl solution, Yadav *et al.* [68] also observed a direct reduction of oxygen on active zinc. Yet on passive zinc, the reaction did not yield only hydrogen peroxide but also partly direct reduction, which differ slightly from the results presented above.

The cathodic behavior of zinc in passive and active state was more recently modeled by Flitt *et al.* [69]. As shown in Figure 1.3, the authors were capable of fitting experimental data from the literature (here the experimental polarization curves of Leidheiser *et al.* [70]) by implementing in their model a two-electron oxygen reduction at low overpotentials and a four-electron reaction is related to the effective zinc surface covered with zinc oxide to bare surface. This transition was experimentally evidenced by a reduction peak in the polarization curves (recorded potentiodynamically in the cathodic direction) that was reported in other works as well [71,72].

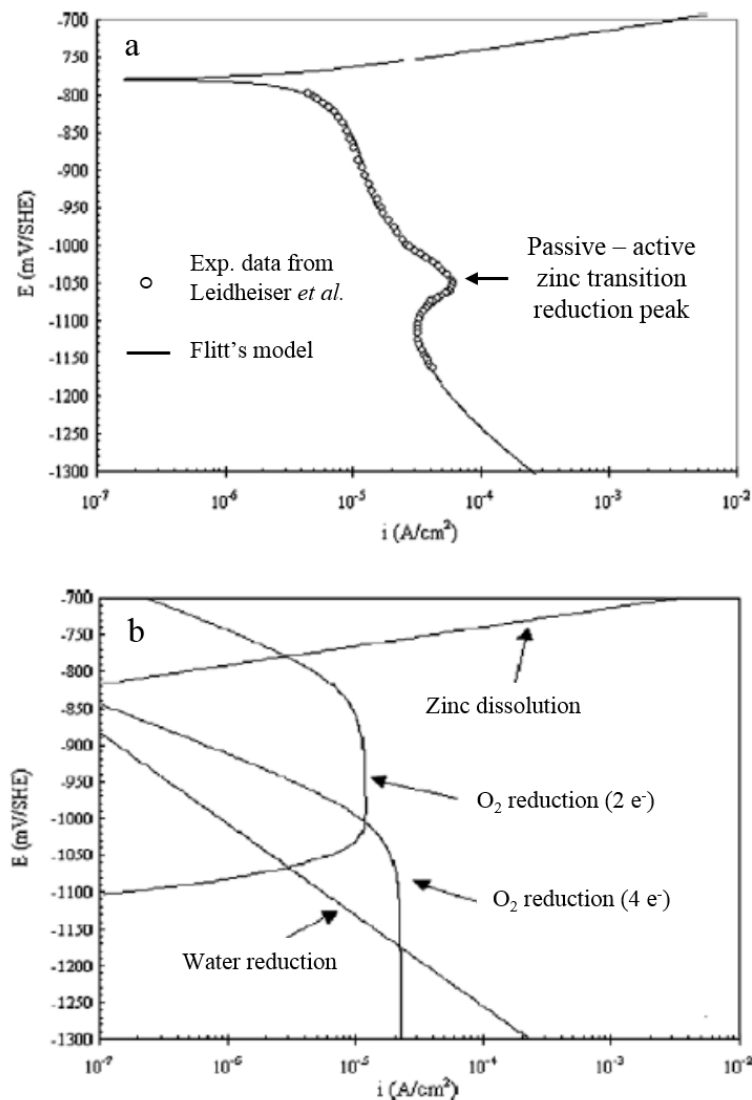


Figure 1.3: Oxygen reduction on zinc in 3% NaCl electrolyte (pH = 6.4) modelled by Flitt *et al.* [69] using the experimental data of Leidheiser *et al.* [70]: (a) experimental and simulated curves and (b) “deconstruction” of the simulated curve showing the 2-electron oxygen reduction (leading to hydrogen peroxide) on passive zinc and the 4-electron (direct) reduction on active zinc.

In contrast, on thicker ZnO films (ca. 1200 nm) prepared by electrodeposition, the ORR kinetics was shown to be governed (partially or mostly) by the direct reduction pathway [73,74]. Goux *et al.* [73] investigated ORR in 0.1M KCl at 70 °C using the rotating disk electrode (RDE) technique on ZnO thin film deposited on platinum substrate. The number of exchanged electrons were found to increase with increasingly negative potential. The polarization curves exhibited large overpotentials (ca 0.6 V, Figure I.4)

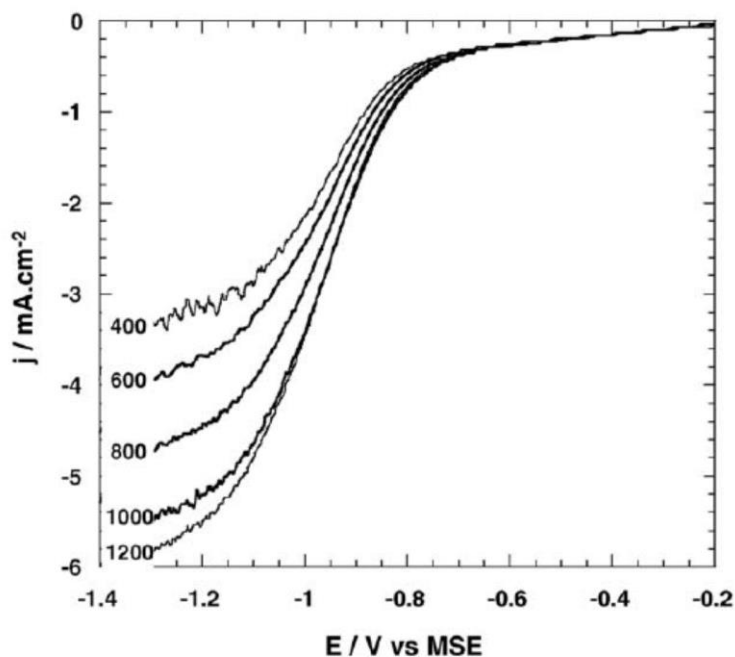


Figure I.4: Cathodic polarization curves recorded with a RDE on electrodeposited ZnO (platinum substrate) in near-neutral 0.1 M KCl solution at 70°C [73]. The reference electrode was a mercurous sulfate electrode (MSE). The number associated to each curve indicates the rotation rate in rpm.

In alkaline solutions at room temperature, Prestat *et al.* [74] also found that electrodeposited ZnO films has a relatively poor electrocatalytic activity towards oxygen reduction reaction. ORR occurred via the direct pathway at the oxygen diffusion plateau with a number of exchanged electrons close to four and almost no hydrogen peroxide was detected at the ring electrode in RRDE experiments.

The barrier properties of ZnO layers (or ZnO-containing) patinas formed on zinc have also been reported in the literature. Recently, Prestat *et al.* [76] grew ZnO patinas by cathodic corrosion of zinc in NaCl solutions. Despite the fine nanostructured morphology of the deposits developing large electrode/electrolyte surface area (see Figure I.5), the cathodic activity of the patina-covered zinc was lower than that of the pristine substrate, suggesting a protective effect of the ZnO layer.



Another reduction of ORR activity was reported on zinc covered by simonkolleite/ZnO bilayers formed by electrochemical oxidation of zinc in NaCl solution [75]. As the uppermost simonkolleite exhibited a very open microstructure, the barrier effect was assigned to the thin nanoporous ZnO-rich film in contact with the substrate.

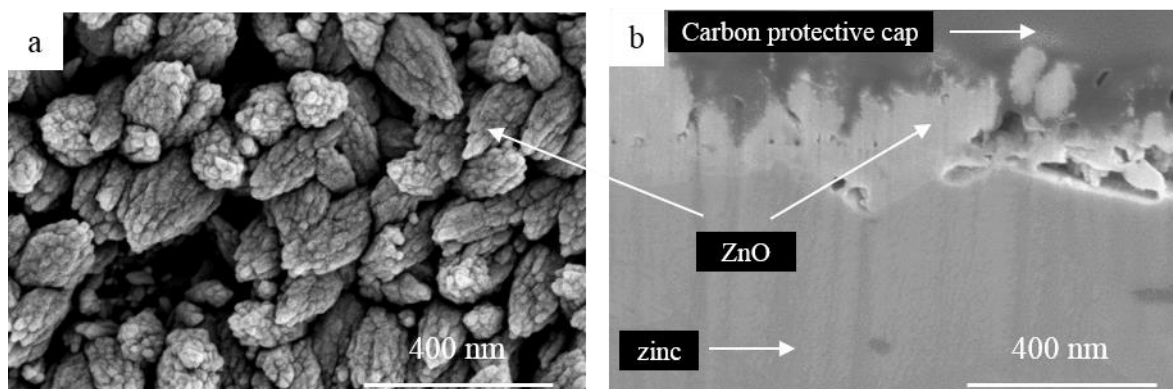


Figure 1.5: High-resolution SEM analysis of nanostructured ZnO patinas grown by cathodic corrosion of zinc in NaCl 0.6 M at -1.2 V (vs SCE) for 17 hours. (a) top-view micrograph and (b) FIB-SEM cross-sectional image [76].

A different viewpoint was proposed in the field of atmospheric corrosion. Some authors have formulated the hypothesis that the degradation of zinc (and zinc alloys) coatings could be cathodically enhanced by the presence of ZnO [77-79]. In a scanning Kelvin probe study, Nazarov *et al.* demonstrated an increase of surface potential of “thick” ZnO films (ca. 200 nm, prepared by thermal oxidation) [80] compared to native films (several nanometers thin) under droplets of zinc sulfate. The authors suggested a greater ability of the thick layers to reduce oxidizing species (such as O<sub>2</sub> molecules).

In contrast, Thomas *et al.* evidenced a protective effect of ZnO patinas grown under artificial seawater droplets [81]. Cross-sectional electron microscopy imaging has found that the passive film that forms in zinc at alkaline pH consists of two layers, exhibiting a significant gradient of porosity with an open structure on the electrolyte side and a compact one close to the zinc substrate [81-83]. Also, a dependence was observed between the patinas formed and the electrolyte pH. At pH 13 solution, formation of soluble Zn(OH)<sub>3</sub><sup>-</sup> and Zn(OH)<sub>4</sub><sup>2-</sup> phases render the precipitated layer unstable increasing zinc corrosion, whereas, at pH 12, the precipitated layer (ZnO/Zn(OH)<sub>2</sub>) is more stable making it an effective anodic barrier upon zinc. These precipitated oxides formed at pH 12 support cathodic reactions on their surface which in turn catalyze further oxide growth by a cathodically driven process. A

model describing the involvement of ORR in the development of such layers was proposed by Venkatraman et al. [84].

### 1.5. Aim of the work and structure of the thesis

This Ph.D. thesis aims at gaining fundamental knowledge on the oxygen reduction at ZnO electrodes using the rotating ring disk electrode (RRDE, described in more details in Chapter 2). This technique allows to detect the hydrogen peroxide generated when oxygen reduction follows (fully or partially) the indirect reaction pathway. This valuable information helps quantifying the prevalence of the direct or indirect pathways that are parallel and therefore in competition. Ideally RRDE requires to have dense and smooth disk electrodes. Radio-frequency magnetron sputtering was used to synthesize such ZnO layers since this technique allows to produce a large variety of coatings by changing experimental parameters such as target composition, reactive gas composition, gas fluxes and power. Two types of layers were prepared and compared: textured (columnar) ZnO with (002) orientation and non-textured ZnO with nano-granular structure.

These films were characterized by different techniques, such as scanning electron microscopy (SEM), X-ray diffraction (XRD), X-ray photoelectron spectroscopy (XPS), energy-dispersive X-ray spectroscopy (EDX), atomic force microscopy (AFM), focused ion beam scanning electron microscope (FIB-SEM) and high-angle annular dark-field scanning transmission electron microscopy (HAADF-STEM). Electrochemical measurements were conducted at room temperature under controlled hydrodynamic conditions using RRDE, linear sweep (potentiodynamic) voltammetry and electrochemical impedance spectroscopy (EIS). The electrolyte was a KOH solution at pH 10 with KCl 0.2 M as supporting electrolyte.

Following the present introduction, the Ph.D. thesis is structured as follows:

Chapter 2 presents the experimental techniques used in this research work: rf-magnetron sputtering (for the synthesis of the ZnO films), characterization techniques and electrochemical methods.

Chapter 3 deals with the synthesis, the characterization and the ORR activity of textured films with (002)-orientation. Those layers degraded quickly under DC cathodic polarization leading to partial delamination. First results on the cathodic activity and on the

ORR reaction mechanism are reported. The Annex I documents preliminary experiments related to this chapter.

Chapter 4 investigates the degradation of the textured ZnO films observed in Chapter 3 by combining electrochemical impedance spectroscopy experiments, equivalent circuit modelling and electron microscopy imaging at the microscale and the nanoscale. Notably, the capacitance of the ZnO layer is shown to describe well the crack propagation during polarization.

Chapter 5 is dedicated to the investigation of non-textured ZnO layers that exhibit good mechanical stability. Relevant quantitative results on the competition between direct and indirect oxygen reduction pathways obtained with RRDE are presented. Comparisons between textured and non-textured layers are made in terms of nanostructure, capacitance and ORR activity are made

Chapter 6 summarizes the findings of this Ph.D. thesis, draw the main conclusions and proposes ideas for continuing research on oxygen reduction at ZnO electrodes.

Finally, the Annex II is an already published paper on the barrier properties of ZnO grown by cathodic corrosion of zinc. For this type of ZnO coating was not produced by rf-magnetron sputtering and was not suitable for RRDE investigations, this article, co-authored by J. Soares Costa, is not integrated in the main structure of this Ph.D. thesis. Yet, as it provides some information of the cathodic behavior of one kind of nanostructured ZnO, it was included in the state of the art above [76].

Modified versions of Chapters 3, 4 and 5 have been or will be submitted as original research manuscripts to peer-reviewed scientific journals focusing on electrochemistry, thin films and materials science.

### 1.6. References

- [1] D. Landolt., *Traité des matériaux: Corrosion et chimie de surfaces des métaux*, PPUR (1997);
- [2] G.H. Koch et al., *Corrosion costs and preventive strategies in the United States*, by CC Technologies Laboratories, Inc. to Federal Highway Administration, 2001;
- [3] M. G. Fontana. *Corrosion engineering*. McGraw-Hill, 1987;
- [4] P. A. Schweitzer. *Corrosion Engineering Handbook - 2nd Edition*, CRC Press, 2006;

- [5] P. A. Schweitzer. Fundamentals of Corrosion: Mechanisms, Causes, and Preventative Methods, 1st Edition, CRC Press, 2009;
- [6] P. R. Roberge. Handbook of Corrosion Engineering, 2<sup>nd</sup> Edition, 2012, McGraw-Hill;
- [7] T. E. Graedel. Corrosion mechanisms for zinc exposed to the atmosphere, Journal of the Electrochemical Society, 136 (1989) 193;
- [8] A. M. Beccaria, Zinc layer characterization on galvanized steel by chemical methods, Corrosion, 46 (1990) 906-912;
- [9] J. J. Friel, Atmospheric corrosion products Al, Zn, and AlZn metallic coatings, Corrosion 42 (1986) 422-426;
- [10] S. Koizumi, S. Shima, Y. Matsushima, A development of black chromate oxide niches by baking process for galvanized steel. In International Conference on Zinc and Zinc Alloy Coated Steel Sheet\_Galvatech'89, (1989) 246-253;
- [11] E. Schedin, G. Engberg, S. Karlsson, R. Kiusalaas, H. Klang. Plasticity of pure zinc hot-dip galvanized coatings. In International Conference on Zinc and Zinc Alloy Coated Steel Sheet Galvatech'89 (1989) 493-499;
- [12] E. Johansson, J. Gullman, Corrosion study of carbon steel and zinc-comparison between exposure and accelerated tests. ASTM special technical publication (1995) 240-256;
- [13] I. Odnevall, C. Leygraf. Formation of  $\text{NaZn}_4\text{Cl}(\text{OH})_6\text{SO}_4 \cdot 6\text{H}_2\text{O}$  in a marine atmosphere, Corrosion science 34 (1993) 1213-1229;
- [14] T. Biestek, M. Drys, N. Sokolov, D. Knotkova, R. Ramishvili, V. Kozhukharov, M. Zeidel, Atmospheric corrosion of metallic systems. v. identification of the chemical compounds in the corrosion products of zinc. PROTECT. METALS. 19 (1984) 612-615;
- [15] I. Odnevall C. Leygraf, A comparison between analytical methods for zinc specimens exposed in a rural atmosphere. Journal of the Electrochemical Society 138 (1991) 1923;
- [16] A. Janotti and C. G. Van de Walle, Fundamentals of zinc oxide as a semiconductor, Rep. Prog. Phys. 72 (2009) 126501;
- [17] Ü. Özgür, V. Avrutin, H. Morkoç, Chapter 16 - Zinc Oxide Materials and Devices Grown by Molecular Beam Epitaxy, Molecular Beam Epitaxy 2<sup>nd</sup> Edition, (2018) 343-375;
- [18] H. Morkoç, U. Özgür. Zinc oxide: fundamentals, materials and device technology, ed. Wiley- VCH, Weinheim (2007) 1-2;
- [19] L. Schmidt-Mende, J. L. Macmanus-Driscoll. ZnO – nanostructures, defects, and devices. Materials Today, 10 (2007) 40-48;
- [20] E. Vasco, Growth evolution of ZnO films deposited by pulsed laser ablation. Journal of Physics: Condensed Matter 13 (2001) 63-72;

- [21] W. Mtangi, A comparative study of the electrical properties of Pd/ZnO Schottky contacts fabricated using electron beam deposition and resistive/thermal evaporation techniques. *Journal of Applied Physics* 110 (2011) 1-5;
- [22] Y. S. Choi, Effect of VI/II gas ratio on the epitaxial growth of ZnO films by metalorganic chemical vapor deposition. *Japanese Journal of Applied Physics* 50 (2011);
- [23] H. F. Liu, Effects of substrate on the structure and orientation of ZnO thin film grown by rf-magnetron sputtering. *Journal of Applied Physics* 102 (2007);
- [24] R. Ondor-Ndong, Properties of RF magnetron sputtered zinc oxide thin films. *Journal of Crystal Growth* 255 (2003) 130-135;
- [25] I.-S. Kim, Magnetron sputtering growth and characterization of high-quality single crystal ZnO thin films on sapphire substrates. *Semiconductors Science and Technology* 19 (2004) 29-31;
- [26] S.-S. Lin, J.-L. Huang. Effect of thickness on the structural and optical properties of ZnO films by rf. magnetron sputtering. *Surface & Coatings Technology* 185 (2004) 222-227;
- [27] W. K. Burton, N. Carberra, F. C. Frank, The growth of crystals and the equilibrium structure of their surfaces, *Philosophical Transactions of the Royal Society of London A* 243 (1951) 299;
- [28] S. Y. Chu, W. Water, J.T. Liaw, Influence of postdeposition annealing on the properties of ZnO films prepared by RF magnetron sputtering, *Journal of the European Ceramic Society* 23 (2003) 1593–1598;
- [29] Z. Onuk, N. Rujisamphan, R. Murray, M. Bah, M. Tomakin, S. I. Shah, Controllable growth and characterization of highly aligned ZnO nanocolumnar thin films, *Applied Surface Science* 396 (2017) 1458-1465;
- [30] K. B. Sundaram, A. Khan, Characterization and optimization of zinc oxide films by rf. magnetron sputtering, *Thin Solid Films* 295 (1997) 87-91;
- [31] D. L. Cheng, K. S. Kao, C. H. Liang, Y. C. Wang, Y. C. Chen, W. C. Shih, L. P. Chan, Piezoelectric Response Evaluation of ZnO Thin Film Prepared by RF Magnetron Sputtering, *MATEC Web of Conferences* 109 (2017) 04001;
- [32] N. H. Al-Hardan, M. J. Abdullah, A. A. Aziz, H. Ahmad, M. Rashid, The effect of oxygen ratio on the crystallography and optical emission properties of reactive RF sputtered ZnO films, *Physica B: Condensed Matter* 405 (2010) 1081-1085;
- [33] G. T. Babcock, M. Wikstrom, Oxygen activation and the conservation of energy in cell respiration, *Nature* 356 (1992) 301–309;
- [34] P. G. Falkowski, Y. Isozaki, The story of O<sub>2</sub>, *Science* 322 (2008) 540–542;

- [35] C. Song, J. Zhang, Chapter: Electrocatalytic Oxygen Reduction Reaction, PEM Fuel Cell Electrocatalysts and Catalyst Layers, Springer (2008) 89-134;
- [36] M. Lefevre, E. Proietti, F. Jaouen, J.P. Dodelet, Iron-based catalysts with improved oxygen reduction activity in polymer electrolyte fuel cells, *Science* 324 (2009) 71–74;
- [37] J. A. Cracknell, K.A. Vincent, F.A. Armstrong, Enzymes as working or inspirational electrocatalysts for fuel cells and electrolysis, *Chem. Rev.* 108 (2008) 2439–2461;
- [38] J. Zhang, Z. Zhao, Z. Xia, L. Dai, A metal-free bifunctional electrocatalyst for oxygen reduction and oxygen evolution reactions, *Nat. Nanotechnol.* 10 (2015) 444–452;
- [39] Y. Li, M. Gong, Y. Liang, J. Feng, J.E. Kim, H. Wang, G. Hong, B. Zhang, H. Dai, Advanced zinc-air batteries based on high-performance hybrid electrocatalysts, *Nat. Commun.* 4 (2013) 1805;
- [40] M. R. Hoffmann, S.T. Martin, W. Choi, D.W. Bahnemann, Environmental application of semiconductor photocatalysis, *Chem. Rev.* 95 (1995) 69–96;
- [41] Q. Xiang, J. Yu, M. Jaroniec, Graphene-based semiconductor photocatalysts, *Chem. Soc. Rev.* 41 (2012) 782–796;
- [42] A. Fujishima, X. Zhang, D.A. Tryk, TiO<sub>2</sub> photocatalysis and the related surface phenomena, *Surf. Sci. Rep.* 63 (2008) 515–582;
- [43] D. Ravelli, D. Dondi, M. Faqnoni, A. Albini, Photocatalysis. A multi-faceted concept for green chemistry, *Chem. Soc. Rev.* 38 (2009) 1999–2011;
- [44] X. Ge, A. Sumboja, D. Wu, T. An, B. Li, F.W.T. Goh, T.S.A. Hor, Y. Zong, Z. Liu, Oxygen reduction in alkaline media: from mechanisms to recent advances in catalysts, *ACS Catalysis* 5 (2015) 4643;
- [45] K. Kinoshita, *Electrochemical oxygen technology*, John Wiley, 1992;
- [46] A. Damjanovic, J. O'M Bockris and B.E Conway, *Modern aspects of electrochemistry*, vol. 5, Ed. Plenum. N.Y., USA, (1992) 107;
- [47] J. O'M. Bockris and S.U.M. Khan. *Surface Electrochemistry: A Molecular Level Approache*. Vol. 2. Springer Science & Business Media, 1993;
- [48] A. Damjanovic, O.J. Murphy, S. Srinivasan, B.E. Conway, *Electrochemistry in transition*, Plenum. N.Y., USA, (1992) 107;
- [49] P. A. Sorensen, S. Kiil, K. Dam-Johansen, C. E. Weinell, Anticorrosive coatings: A review, *J. Coat. Technol. Res.* 6 (2009) 135;
- [50] D. Gervasio, I. Song, J. H. Payer, Determination of the oxygen reduction products on ASTM A516 steel during cathodic protection, *J. Appl. Electrochem.*, 28 (1998) 979–992;

- [51] M. Stratmann, R. Feser, A. Leng, Corrosion protection by organic films, *Electrochim. Acta* 39 (1994) 1207-1214;
- [52] A. K. Shukla, R.K. Raman, Methanol-resistant oxygen-reduction catalysts for direct methanol fuel cells, *Annual review of materials research* (2003) 155-168;
- [53] D. R. Sena, E. A. Ticianelli, E. R. Gonzalez, Characterization of the limiting structural effects on the electrochemical behavior of porous gas diffusion electrodes. *Journal of Electroanalytical Chemistry* 357.1-2 (1993) 225-236;
- [54] J. Perez, E.R. Gonzalez and E.A. Ticianelli, Impedance studies of the oxygen reduction on thin porous coating rotating platinum electrodes, *Journal of The Electrochemical Society* 145.7 (1998) 2307-2313;
- [55] A. Damjanovic, M. A. Genshaw, and J. O'M. Bockris, The Mechanism of Oxygen Reduction at Platinum in Alkaline Solutions with Special Reference to H<sub>2</sub>O<sub>2</sub>, *J. Electrochem. Soc.* (1967) 1107-1112;
- [56] H.S. Wroblowa, Y.C. Pan, G. Razumney, Electroreduction of oxygen: a new mechanistic criterion, *J. Electroanal. Chem.* 69 (1976) 195-201;
- [57] A. J. Appleby, M. Savy, Kinetics of oxygen reduction reactions involving catalytic decomposition of hydrogen peroxide: application to porous and rotating ring-disk electrodes, *Journal of Electroanalytical Chemistry and Interfacial Electrochemistry* 92.1 (1978) 15-30;
- [58] R. W. Zurilla, R. K. Sen and E. Yeager, The kinetics of the oxygen reduction reaction on gold in alkaline solution, *Journal of the Electrochemical Society* 125.7 (1978) 1103-1109;
- [59] V. S. Bagotzky, N.A. Shumilova, G.P. Samoilov, E.I. Khrushcheva, Electrochemical oxygen reduction on nickel electrodes in alkaline solutions—II, *Electrochimica Acta* 17.9 (1972) 1625-1635;
- [60] H. S. Wroblowa, S. B. Qaderi, The mechanism of oxygen reduction on zinc, *Journal of Electroanalytical Chemistry and Interfacial Electrochemistry* 295 (1990) 153-161;
- [61] K.-H. Wu, Da-Wei Wang, and Dang-Sheng Su, An Extension to the Analytical Evaluation of the oxygen reduction reaction based on the electrokinetics on a rotating ring-disk electrode 3 (2016) 622-628;
- [62] F. Van den Brink, E. Barendrecht, W. Visscher, Hydrogen peroxide as an intermediate in electrocatalytic reduction of oxygen. – A new method for the determination of rate constants, *J. Electrochem. Soc.* 9 (2003);
- [63] Y. Li, D. Zhang, J. Wu, Study on kinetics of cathodic reduction of dissolved oxygen in 3.5% sodium chloride solution, *Journal of Ocean University of China* 9 (2010) 239;

- [64] I. S. Cole, Recent Progress and Required Developments in Atmospheric Corrosion of Galvanised Steel and Zinc, *Materials* 10 (2017) 1288;
- [65] P. Delahay, A Polarographic Method for the Indirect Determination of Polarization Curves for Oxygen Reduction on Various Metals II. Application to Nine Common Metals, *Journal of the Electrochemical Society* 97 (1950) 205–212;
- [66] H. S. Wroblowa, Intermediate products of atmospheric oxygen reduction and the integrity of metal-organic coating interface, *Journal of Electroanalytical Chemistry* 339 (1992) 31-41;
- [67] H. Dafydd, D. A. Worsley, H. N. McMurray, The kinetics and mechanism of cathodic oxygen reduction on zinc and zinc–aluminium alloy galvanized coatings, *Corrosion Science* 47 (2005) 3006-3018;
- [68] A. P. Yadav, A. Nishikata, T. Tsuru, Oxygen reduction mechanism on corroded zinc, *Journal of Electroanalytical Chemistry* 585 (2005)142-149;
- [69] H. J. Flitt, D. P. Schweinsberg, Synthesis, matching and deconstruction of polarization curves for the active corrosion of zinc in aerated near-neutral NaCl solutions, *Corrosion Science* 52 (2010) 1905–1914;
- [70] H. Leidheiser, I. Suzuki, Technical note: Towards a more corrosion resistant galvanized steel, *Corrosion* 36 (1980) 701-702;
- [71] W. J. Tomlinson, D. R. Breary, Technical Note: Cathodic polarization and corrosion of Zn and ZnAl in 3% NaCl solution, *Corrosion* 44 (1988) 62-63;
- [72] H. Leidheiser, Y. Momose, R. D. Granata, Technical note: Inhibition of the cathodic reaction on zinc in aerated 3% NaCl solution, *Corrosion* 38 (1982) 178-179;
- [73] A. Goux, T. Pauporte, D. Lincot, Oxygen reduction reaction on electrodeposited zinc oxide electrodes in KCl solution at 70°C, *Electrochimica Acta*, 51 (2006) 3168–3172;
- [74] M. Prestat, F. Vucko, B. Lescop, S. Rioual, F. Peltier, D. Thierry, Oxygen reduction at electrodeposited ZnO layers in alkaline solution, *Electrochimica Acta* 218 (2016) 228-236;
- [75] M. Prestat, L. Holzer, B. Lescop, S. Rioual, C. Zaubitzer, E. Diler, D. Thierry, Microstructure and spatial distribution of corrosion products anodically grown on zinc in chloride solutions, *Electrochemistry Communications* 81 (2017) 56–60;
- [76] M. Prestat, J. S. Costa, B. Lescop, S. Rioual, L. Holzer, D. Thierry, Cathodic Corrosion of Zinc under Potentiostatic Conditions in NaCl Solutions, *ChemElectroChem* 5 (2018) 1203-1211;



- [77] T. Prosek, D. Persson, J. Stouilil, D. Thierry, Composition of corrosion products formed on Zn–Mg, Zn–Al and Zn–Al–Mg coatings in model atmospheric conditions, *Corrosion Science* 86 (2014) 231-238;
- [78] T. Prosek, J. Hagström, D. Persson, N. Fuertes, F. Lindberg, O. Chocholaty, C. Taxén, J. Serák, D. Thierry, Effect of the microstructure of Zn-Al and Zn-Al-Mg model alloys on corrosion stability, *Corrosion Science* (2016);
- [79] J. Stouilil, T. Prosek, A. Nazarov, J. Oswald, P. Kriz, D. Thierry, Electrochemical properties of corrosion products formed on Zn-Mg, Zn-Al and Zn-Al-Mg coatings in model atmospheric conditions, *Materials and Corrosion* 66 (2015) 777-782;
- [80] A. Nazarov, E. Diler, D. Persson, D. Thierry, Electrochemical and corrosion properties of ZnO/Zn electrode in atmospheric environments, *Journal of Electroanalytical Chemistry* 737 (2015) 129-140;
- [81] S. Thomas, I. S. Cole, N. Birbilis, Compact oxides formed on zinc during exposure to a single sea-water droplet, *Journal of the Electrochemical Society* 160 (2013) 59;
- [82] S. Thomas, I. S. Cole, M. Sridhar, N. Birbilis, Revisiting zinc passivation in alkaline solution, *Electrochimica Acta* 97 (2013) 192;
- [83] S. Thomas, N. Birbilis, M. S. Venkatraman, I. S. Cole, Self-repairing oxides to protect zinc: Review, discussion and prospects, *Corrosion Science* 69 (2013) 11;
- [84] M. S. Venkatraman, I. S. Cole, B. Emmanuel, Corrosion under a porous layer: A porous electrode model and its implications for self-repair, *Electrochimica Acta* 56 (2011), 8192-8203.

### Experimental Techniques – Theory and Setups

---

#### Abstract

In this chapter, the main experimental techniques used in this Ph.D. thesis are briefly described: substrate preparation, RF magnetron sputtering, electrochemical methods (RDE, RRDE, EIS) and characterization techniques (AFM, profilometer, XRD, SEM, STEM, EDX, FIB, XPS).

#### 2.1. Substrate preparation

For this work, ZnO films were deposited on copper substrates using the radio-frequency magnetron sputtering technique. Copper cylinders substrates (5 mm diameter, 4 mm height) were micro-machined from commercially available rods (purity > 99.95%) to be suitable for the RRDE setup. After machining, they were pre-polished with SiC paper (P2500, P4000 for 60s each one) in a Stuers Tegramin-25 polishing machine using water as a lubricant. Then, they were polished with MasterTex 10" paper with polycrystalline diamond suspension (3  $\mu\text{m}$  and 1  $\mu\text{m}$  for 180 s each one). Copper substrates were ultrasonically cleaned in ethanol, rinsed in deionized water and air-dried before the deposition.

#### 2.2. Sputtering technique

"Sputtering" is the phenomenon in which atoms are ejected from a solid target material due to bombardment of the target by energetic particles. The effect occurs through the transfer of energy between the particles of the solid target material and the incoming particles [1-3]. It only happens when the kinetic energy of the incoming particles is much higher than conventional thermal energies ( $\gg 1$  eV). If the ionic bombardment or plasma process of a material is prolonged, significant erosion of the material will occur, and this may be dangerous.

##### 2.2.1. Deposition process

This technique consists of removing atoms from a solid target material and then depositing them on a substrate. The entire process occurs in vacuum chambers with low pressure gases. A large negative potential between target and substrate initiates the process

and electrons will be emitted from the target surface. The ejected electrons are accelerated due to the potential and get a very high kinetic energy. They collide with the gas molecules and ionize them. The positive ions are accelerated towards the cathode. On hitting the target surface, part of the energy is transformed into heat and part is transferred to other particles. These particles can eventually get enough energy to leave the target surface. Various particles are eventually emitted: neutral atoms which will eventually reach the substrate and build the film, negative ions, photons and secondary electrons.

The secondary electrons will again be accelerated from the target and ionize more gas atoms that will sputter the target and so on. The secondary electron yield needs to be high enough in order to maintain the plasma. When the substrate is immersed into the plasma (shutter removed), the electrons cover the surface much faster than the ions. A negative potential is created, which attracts the ions and repels the electrons. Around the substrate an electron depleted sheet is formed, up to a steady state condition when the ionic current equals to the electron current. In the absence of oxygen, the plasma is confined within the chimney near the cathode and only illuminates the exposed face of the substrate holder. The introduction of a low oxygen flow induces a change in the plasma color. For high oxygen flow rates, the plasma completely changes and is no longer localized in the chimney vicinity but fills the entire reactor. The oxygen flow thus plays a major role on the expansion of the plasma emitting zone. The target has always the strongest negative potential [4-7]. A schematic of the sputtering deposition process is shown in Figure 2.1.

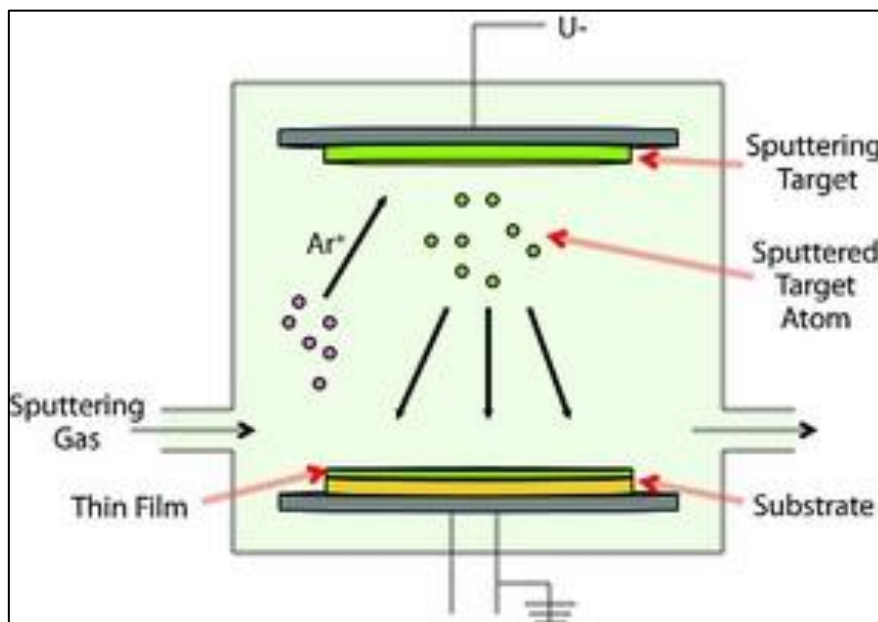


Figure 2.1: Schematic of the sputtering deposition process [8].

### **DC-sputtering (DC voltage)**

The deposition process explained was for DC sputtering (in which case the voltage source is DC) being used for the deposition of conductive materials. DC sputtering technique for insulating or semiconducting materials will cause a positive charge accumulation on the target surface and consequently will occur an efficiency reduction in the process, extinguishing the plasma [5, 11].

### **RF-sputtering (AC voltage)**

The RF-sputtering technique is used in the case of non-conductive or low conductivity targets. In this technique a high frequency alternating signal is applied from an alternating current source. When negative potential is applied, positive ions are attracted to the target by positively charging it, during positive alternation of the source, electrons are attracted to the surface of the target discharging the same. Due to the constant discharge of electrons, the target behaves like a cathode for most of the process [7, 11].

### **Magnetron sputtering**

In conventional sputtering (not all electrons contribute to working gas ionization) some electrons are accelerated towards the wall chamber, producing heating and radiation. To optimize the deposition process and to avoid possible problems, the magnetron sputtering technique was developed. In this technique, a magnetic field is applied perpendicular to the voltage applied on the target. The intersection between these fields (magnetic and electric fields) will produce the confinement of the secondary electrons emitted in a region close to the target. These electrons accumulation will cause a significant increase in the probability of a collision between electrons and atoms of the gas. Consequently, there will be an increase in ionization, making the plasma denser. A schematic of the process is shown in Figure 2.2. The use of this method allows the reduction of gas pressure. At lower pressures the number of collisions is also reduced, making the sputtering more directional [3].

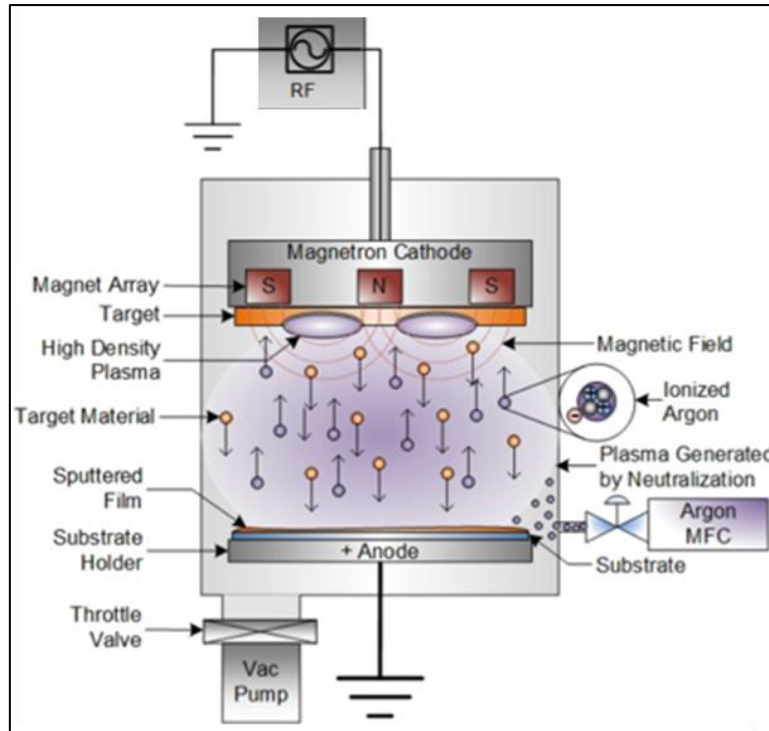


Figure 2.2: Diagram of the RF magnetron sputtering process [12].

Magnetic fields perpendicular to the electric field are used to confine the plasma near the target surface. The magnetic field is created by set magnets that are below the target. Thus, the secondary electrons (emitted by the target during the bombardment) do not bombard the substrate because they are trapped in helical trajectories close to the target and consequently do not contribute to the increase on the substrate temperature [13-18]. This allows use temperature-sensitive substrates (as plastic materials) and sensitive surfaces (as semiconductor oxide metal), producing minimal defects [16].

The main disadvantage of this technique is the non-uniform erosion of the target, which leads to use about 30% of the target, and decreases the deposition rate. Almost all non-ferromagnetic metals can be pulverized.

### 2.2.2. Structure of thin films deposited by sputtering

In general, two stages are significant in growth evolution of thin films: initial stage (nucleation and coalescence) and intermediate growth. During the initial stage, the physical and chemical properties of the substrate, and the interaction between the substrate and the particles that reach it, play an important role. After the first layers are formed covering the substrate, the intermediate growth begins, during which the interaction occurs only between

the particles and the film. Thus, during the growing evolution of the films, the physical surface processes determine the grain structure and surface morphology. Are they:

- Bombardment on the substrate surface/film;
- Adsorption of the atoms in the collision;
- Diffusion of the atoms on the surface of films.

These processes are related to the absorption energy at the moment of collision and the angle of atoms incidence, physical and chemical interaction between the atoms and the substrate/film surface, and especially the substrate temperature. A model that correlates the grain structure and surface morphology was proposed by Thornton in 1974 [19] and is called "zonal structure model". This model explains the growth of the grain structure in four different zones: Zone I, Zone T, Zone II and Zone III, as a function of the argon pressure and the TS/T<sub>m</sub> ratio, where TS is the substrate temperature and T<sub>m</sub> is the melting temperature of the material to be deposited. Originally, this model was developed to describe the growth of metals deposited via sputtering. However, in the literature, this model is also widely used to describe the film growth of different materials deposited by the same technique.

There are fundamental differences between TCOs and metals, so Kluth *et al.* [20] suggested modifications of the original Thornton model. First, the ZnO exhibits a high melting temperature (1975°C) when compared to the typical metal temperature. However, the ratio between the substrate temperature TS and melt temperature of the material to be deposited T<sub>m</sub> (considered in the Thornton model) becomes very small at typical TS (80-400°C) intervals during sputtering deposition. In this case, the modified Thornton model is analyzed as a function of substrate temperature and not as a function of TS/T<sub>m</sub> ratio.

Figure 2.3 shows the three zones present in the modified model as a function of the working pressure and the substrate temperature (TS). From this, it is noted that due to the high melting point of ZnO (1975 °C) the Zone III, which corresponds to the grain recrystallization in the original model, is not present in the range temperature used in this case, since recrystallization appears at elevated substrate temperature. One point of the Thornton model is maintained: the increase in TS and the reduction of working pressure lead to an increase in the compaction and density of the film structure. For a better understanding, the characteristics of each zone are detailed below [19,20]:

- Zone I: low atom diffusion, narrow conical crystallite structures separated by voids (Figure 2.3a);
- Zone T is the transition region: the atoms diffusion is large and there is filling of voids found in zone I. So, it is difficult to identify outline grains. The structures are dense with "V" -type fiber-like grains and exhibit a relatively smooth surface;
- Zone II: high diffusion and the migration effect on grain boundary become dominant. In this case, the larger grains grow at the expense of smaller grains and follow a preferential orientation, resulting in a columnar structure of crystals of the same orientation. This zone is shown in Figure 2.3b.

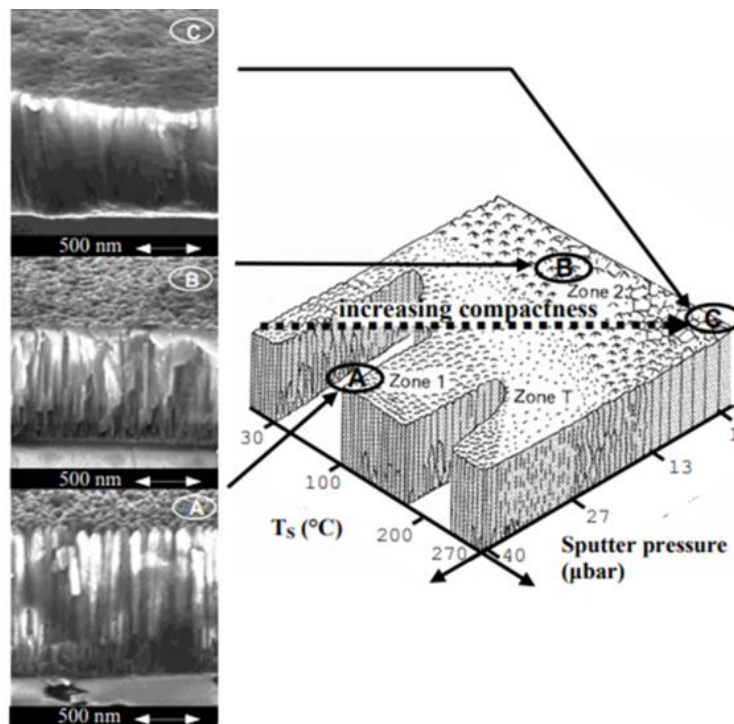


Figure 2.3: Adapted scheme of the modified model of zone structure proposed by Kluth *et al.* [20] for the ZnO: Al films. The micrographs illustrate the morphology of these films and indicate the growth zone.

Because of collisions with the argon atoms, the energy of the particles arriving at the substrate/film surface decreases with increasing argon pressure, leading to a decrease in energy for diffusion surface. In addition, at high pressures, the adsorbed argon atoms limit the mobility of the atoms. Therefore, the temperature transition between Zones I, T and II increase with the argon pressure. On the other hand, the transition temperature between Zones II and III is independent of the argon pressure, since this transition is determined by the internal material diffusion. ZnO thin films grown by sputtering have a polycrystalline

surface morphology. The individual grains are strongly oriented with their crystallographic c-axis parallel to the substrate. Different surface morphological structures are developed during deposition. For example, in crystalline substrates such as silicon, the growth evolution occurs in structures with small grains. On the other hand, in amorphous substrates such as glass there is growth in columnar grains that increase in size with film thickness.

### 2.2.3. Sputtering setup

For this research the radio-frequency magnetron sputtering (Univex 350, Oerlikon) has been used. The pump system is a turbomolecular with the primary system. The RF source is 350W, 13,56 Hz, with 4 targets with shutters. The base pressure choose was  $3 \cdot 10^{-7}$  mbar.

Figure 2.4 shows an overview of the sputtering system (a) and the components in the vacuum chamber (b).

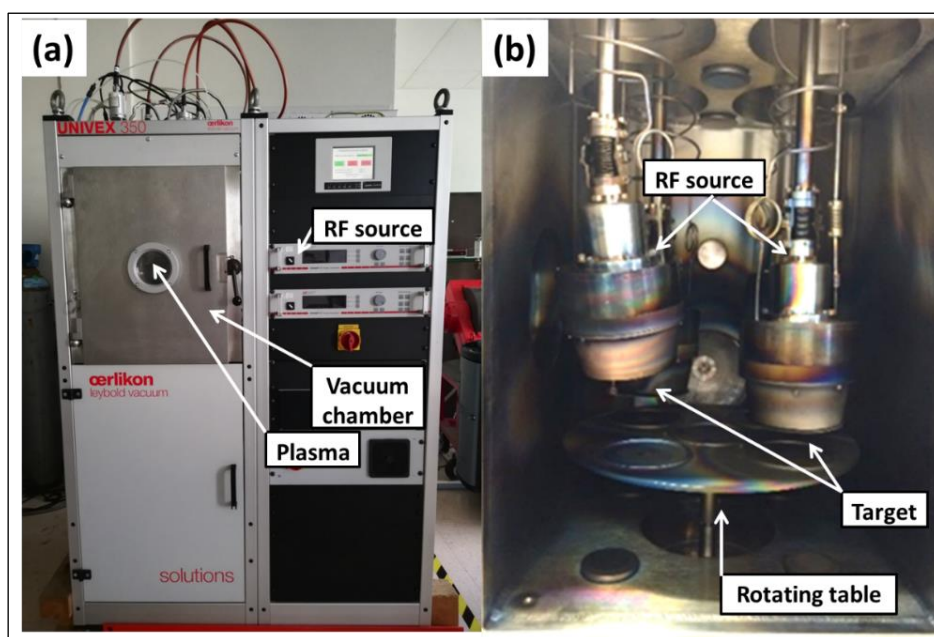


Figure 2.4: Overview Univex 350, Oerlikon radio-frequency magnetron sputtering system.

## 2.3. Electrochemical techniques

### 2.3.1 Rotating disk electrode (RDE)

The rotating disk electrode (RDE) method has been widely used for electrochemical analysis as it enables to work under well-controlled hydrodynamic conditions by adjusting the convective-diffusive transport of electroactive species towards the electrode surface [21]. Figure 2.5 shows the working principle of the RDE.



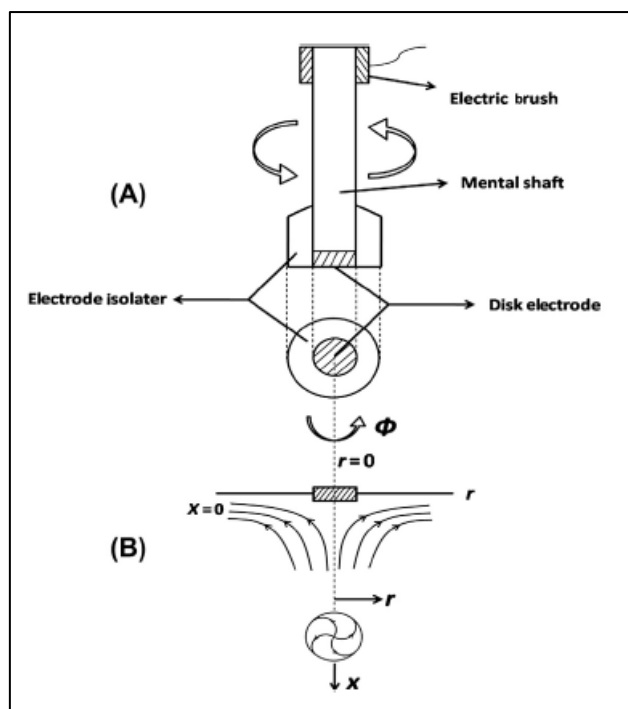


Figure 2.5: Sketch of the working principle (A) and the hydrodynamic profile (B) of the RDE [22-24].

The forced convection (rotation) causes a suction of the liquid towards the electrode. Simultaneously, the radial movement moves the electrolyte out of the center towards the edge of the electrode. The flow conditions lead to the formation of a uniform diffusion film of homogeneous thickness [22-24]. The diffusion layer thickness depends on the rotation rate, the kinematic viscosity of the solution and the diffusion coefficient of the reactive species. Typically, the rotation rate varies between ca. 30 and 2000 rpm and the thickness of the diffusion layer,  $\delta$ , decreases with increasing rotation rate [22,25]:

$$\delta = 0.201 D^{1/3} \nu^{1/6} \omega^{-1/2} \quad (1)$$

where  $\nu$  is the kinematic viscosity,  $D$  the diffusion coefficient of the electroactive species and  $\omega$  the rotation rate of the electrode (expressed in rpm). When the reaction is fully controlled by mass transport, the limiting current,  $I_L$ , is:

$$I_L = n F S D C / \delta \quad (2)$$

where  $n$  is the number of electrons involved in the reaction,  $F$  the Faraday constant,  $S$  the electrode surface area and  $C$  the concentration of the electroactive species. Rearranging Eqs.

(1) and (2), one obtains the Levich equation, where the limiting current for the RDE is [25,26]:

$$I_L = 0.201 n F S D^{2/3} \nu^{-1/6} C \omega^{1/2} \quad (3)$$

In contrast, when a reaction is fully controlled by charge transfer (in absence of mass transport limitations), the current,  $I_k$ , is a function of the electrode overpotential as expressed by the Butler-Volmer equation:

$$I_k = I_0 \left( \exp\left(\frac{\alpha_a n F}{RT} \eta\right) - \exp\left(\frac{-\alpha_c n F}{RT} \eta\right) \right) \quad (4)$$

with  $I_0$  being the exchange current density,  $\alpha_a$  and  $\alpha_c$  the anodic and cathodic charge transfer coefficients, respectively,  $\eta$  the overpotential, the  $R$  the universal gas constant and  $T$  the temperature.

If both mass transport and charge transfer controls the process, the reciprocal of the current,  $I$ , will be the sum of each reciprocal contribution:

$$\frac{1}{I} = \frac{1}{I_k} + \frac{1}{I_L} \quad (5)$$

By combining Eqs. (3) and (5), one obtains the Koutecky-Levich equation:

$$\frac{1}{I} = \frac{1}{I_k} + \frac{1}{0.201 n S F C D^{2/3} \nu^{-1/6} \omega^{1/2}} \quad (6)$$

Note that Eq. (3) is a particular case of Eq. (6) when  $I_k \rightarrow \infty$ .

Figure 2.6 shows some simulated RDE data to illustrate how Eqs. (3) and (6) can be exploited. The RDE polarization curves for various rotation rates,  $\omega$ , are displayed in Figure 2.6a. Under mass transport control, the dependance of the limiting current,  $I_L$ , on  $\omega^{1/2}$  (Figure 2.6c) allows to draw the Levich plot (Figure 2.6b) based on Eq. (3). The slope of the straight line yields the number of exchanged electrons,  $n$ , if  $S$ ,  $C$ ,  $D$  and  $\nu$  are known. Under mixed control by mass transport and charge transfer, the plot of  $1/I_L$  vs.  $\omega^{-1/2}$  (Figure 2.6d) is called

the Koutecky- Levich plot that is based on Eq. (6). The slope of the straight line enables to determine the number of exchanged electrons,  $n$ , if  $S$ ,  $C$ ,  $D$  and  $\nu$  are known. The intercept on the vertical axis (i.e. at infinite rotation rate) gives  $1/I_k$ .

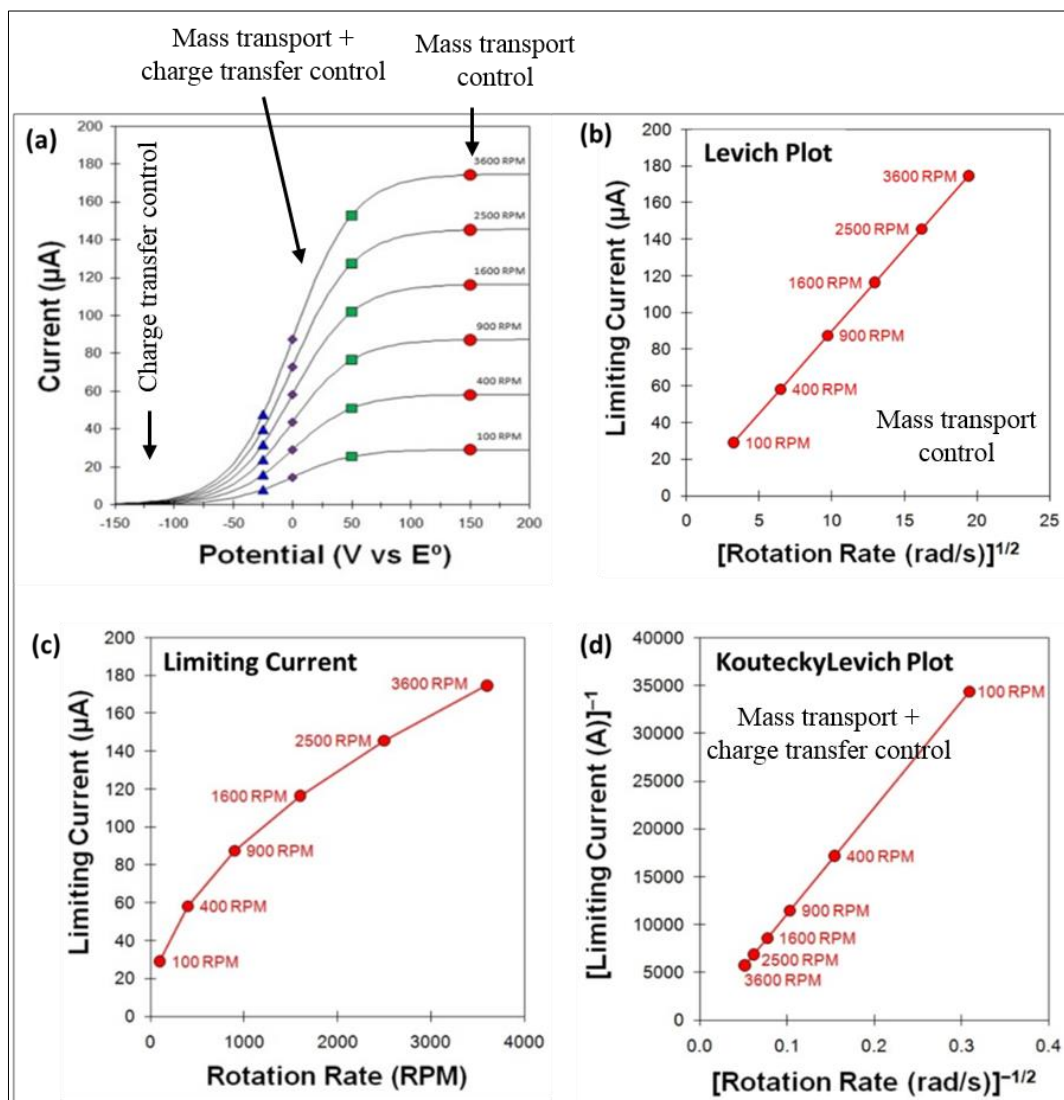


Figure 2.6: Simulated example of a RDE experiment. (a) Polarization curves recorded at different rotation rates; (b) Levich plot corresponding to Eq. (3); (c) Dependence of the limiting current on the square root of the rotation rate (Eq. (3)); (d) Koutecky-Levich plot corresponding to Eq. (6).

### 2.3.2. Rotating ring disk electrode (RRDE)

When one adds a concentric and coplanar ring electrode around the disk (separated from it by a small insulating gap), one obtains a rotating ring-disk electrode (RRDE), as shown Figure 2.7. Due to the electrode rotation, the reaction products generated at the upstream disk are transported toward the downstream ring, where it can be detected if the appropriate potential is chosen (the ring current is under mass transport control) [27]. In this

Ph.D. thesis, the hydrogen peroxide of the indirect oxygen reduction pathway (on the ZnO disk) is detected by re-oxidation (into oxygen) at the gold ring. The higher the ring current, the more relevant the indirect reduction is. The RRDE is characterized the collection efficiency,  $N$ , which is the fraction of the intermediate species generated at the disk that reacts at the ring. In principle,  $N$  depends only on the size of the disk, the ring and the gap that separates. In practice, most researchers use the reduction of (potassium) ferricyanide to ferrocyanide to measure  $N$ . The reaction is assumed to occur in one single step without intermediate species.



The potential of the ring is fixed to carry out the opposite reaction (oxidation of ferrocyanide to ferricyanide). In that case:

$$N = \frac{I_r}{I_d} \quad (8)$$

with  $I_r$  being the ring current and  $I_d$  the (modulus of) of the disk current.

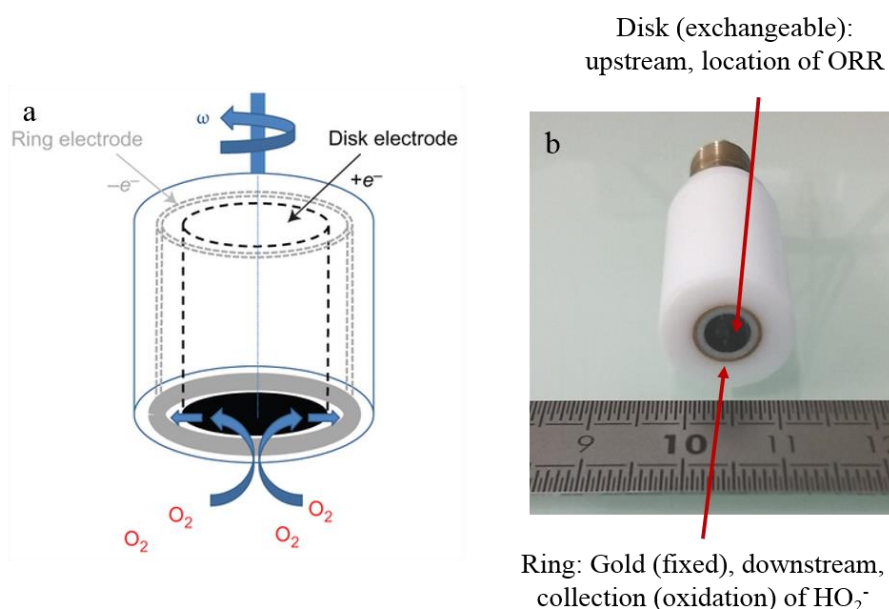


Figure 2.7: Rotating ring disk electrode (RRDE): (a) Sketch of the working principle; (b) Photograph of the RRDE used in this Ph.D. thesis for ORR investigations.

### 2.3.3. RRDE and RDE setups

The RRDE setup was acquired from Pine Research Instrumentation, Durham, NC, USA (Figure 2.8). A bipotentiostat is needed to control the two independent working electrodes (ring and disk) that “share” the same reference electrode (in our case, Hg-HgO, KOH 1M). The bipotentiostat was formed by two synchronized Gamry Reference 600 potentiostats. The collection efficiency of the ring was measured to be 23 % 5with the ferro/ferricyanide experiment mentionned above).

The RDE configuration is obtained by disconnecting the ring (and the attached potentiostat) and works as a classical three-electrode cell.

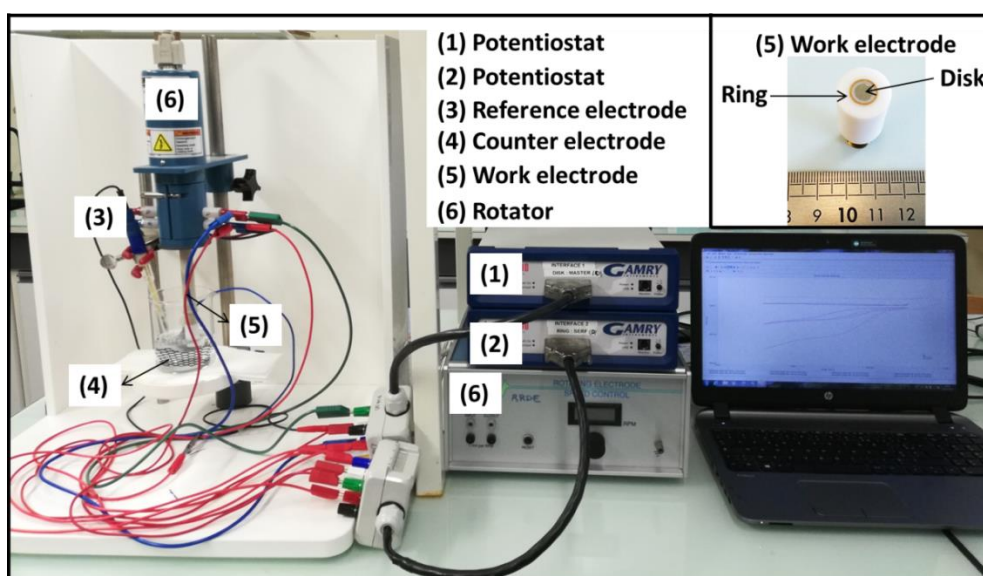


Figure 2.8: Photograph of the RRDE setup used during this Ph.D. thesis. Inset: photograph of the RRDE head (see also Figure 2.7b).

## 2.4. Electrochemical Impedance Spectroscopy (EIS)

### 2.4.1. Impedance definition: concept of complex impedance

EIS is a non-destructive technique used to understand the interfacial behavior of electrochemical systems, being so one of the most common techniques in corrosion studies. Electrical resistance is the ability of a circuit element to resist the flow of electrical current. Ohm's law defines resistance in terms of the ratio between voltage,  $E$ , and current,  $I$ . The use of this relationship is limited to only one circuit element (ideal resistor).

An ideal resistor has several simplifying properties: it follows Ohm's law at all current and voltage levels, its value is independent of frequency, and AC current and voltage signals though a resistor are in phase with each other [28–31]. However, there are circuit elements that exhibit much more complex behavior, so that the simple concept of resistance must be

replaced by impedance. Electrochemical impedance is usually determined by applying an AC (sinusoidal) potential or current to an electrochemical cell and then measuring the current or the potential, respectively, through the cell.

The response to this perturbation potential/current signal is an AC current/potential signal that can be analyzed as a sum of sinusoidal functions (Fourier series) [28–31]. EIS is usually measured using a small excitation signal, so that the cell response is pseudo-linear. For a linear system, the current response to a sinusoidal potential is a sinusoidal signal with the same frequency as the potential but shifted in phase (Figure 2.9).

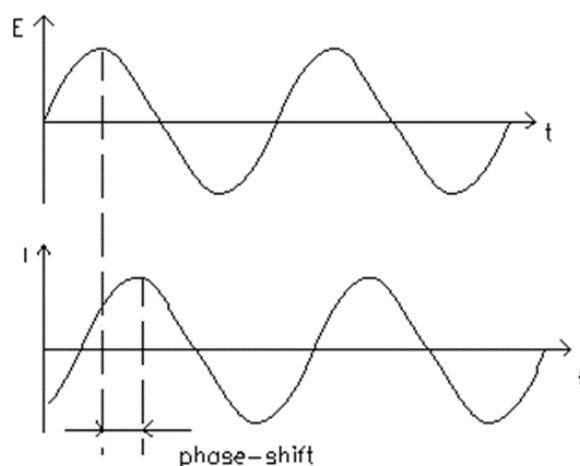


Figure 2.9: Sinusoidal current response of a linear system [28–31].

The excitation time signal,  $E_t$ , at a constant polarization potential, is given by:

$$E_t = E_0 \sin(\omega t) \quad (9)$$

Where  $E_0$  is the amplitude of the signal (independent of frequency) and  $\omega$  is the angular frequency. The relationship between the angular frequency  $\omega$  (in  $\text{rad}\cdot\text{s}^{-1}$ ) and the frequency  $f$  (in Hz) is:

$$\omega = 2\pi f \quad (10)$$

For a linear system, the response signal,  $I_t$ , is given by:

$$I_t = I_0 \sin(\omega t + \phi) \quad (11)$$

With  $I_0$  the amplitude (dependent on  $\omega$ ) and  $\phi$  the phase-shift. An expression analogous to Ohm's law allows calculating the impedance of the system (complex number) defined at each frequency by:

$$Z(\omega) = |Z(\omega)|e^{-j\phi} = \frac{E_0}{I_0} (\cos\phi - j \sin\phi) \quad (12)$$

The impedance is therefore expressed in terms of a modulus,  $|Z|$ , and a phase shift,  $\phi$ , or in terms of a real part,  $Z_r$ , and an imaginary part,  $Z_j$ .

$$|Z(\omega)| = Z_r(\omega) + jZ_i(\omega) \quad (13)$$

In a three-electrode system, the potentiostat applies (at a constant DC potential) a sinusoidal potential of small amplitude. Then the current response is compared with original input signals in the analyzer. Through the response analyzer, the real and imaginary parts of the electrochemical impedance of the system are obtained.

This method is appropriate for a frequency range between  $10^{-4}$  and  $10^6$  Hz. If we plot the applied sinusoidal signal  $E_t$  on the x-axis of a graph and the sinusoidal response signal  $I_t$  on the y-axis, the result is an ellipse (Figure 2.10). This ellipse is known as a “Lissajous figure”. Analysis of Lissajous figures on oscilloscope screens was the accepted method of impedance measurement prior to the availability of modern EIS instrumentation [28–31].

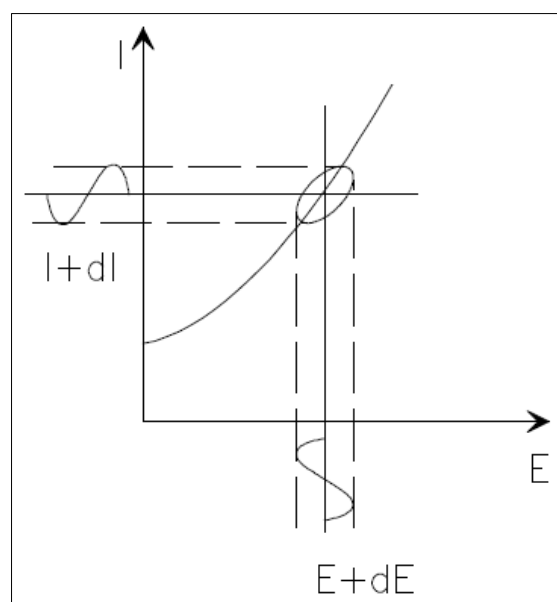


Figure 2.10: Origin of Lissajous Figure [28–31].

**Data representation**

The expression for  $Z(\omega)$  is composed of a real and an imaginary part. Plotting the real part on the x-axis and the opposite of the imaginary part on the y-axis of a chart, we get a Nyquist Plot. The Nyquist plot shown in Figure 2.11a exhibits one semicircle (characteristic of a single time constant) but could also contain several semi-circles [28-31].

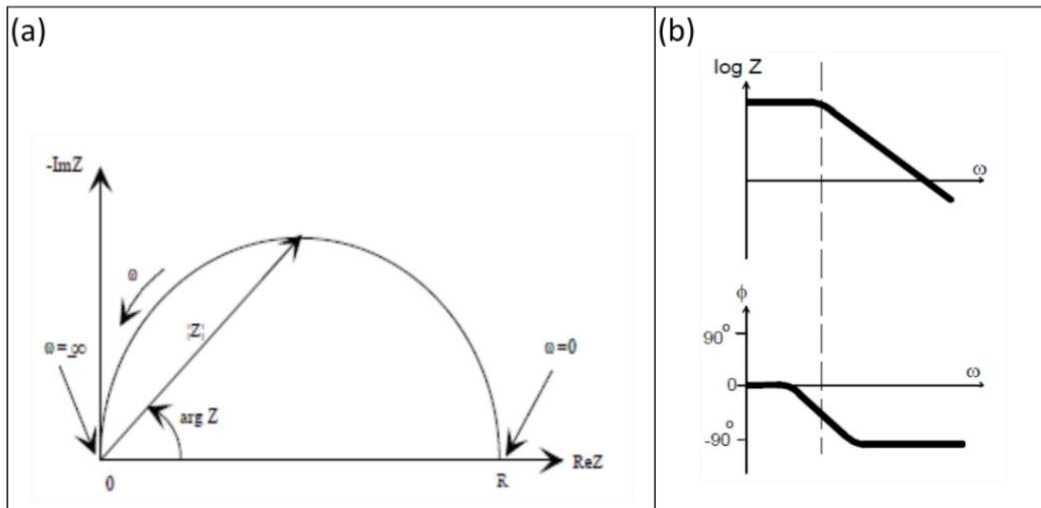


Figure 2.11: EIS representation: (a) Nyquist plot with impedance vector (b) Bode plots (with one time constant) [28-31].

On the Nyquist plot, the impedance can be represented as a vector (arrow) of length  $|Z|$ . The angle between this vector and the x-axis (phase angle) is  $\phi = \arg Z$ . One major shortcoming of Nyquist plots is that the frequency is an implicit parameter. Another representation of impedance data is Bode plots (Figure 2.11b). The logarithm of the frequency is plotted on the x-axis and both the modulus of the impedance and the phase-shift are plotted on the y-axis.

**Analysis of EIS data**

EIS data are commonly analyzed by fitting them, to an equivalent electrical circuit. Most of the elements in the model are common electrical elements (resistances, capacitances and inductances). Table 2.1 lists the common electrical elements, the equation for their current versus voltage relationship, their impedance and some characteristics.




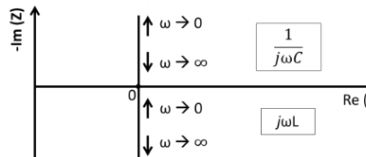
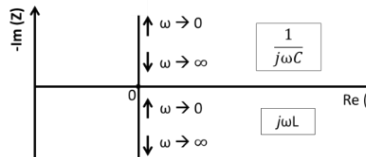
Element	I vs E	Z	Notes	Nyquist representation
<b>Resistor</b>	$E = IR$	$Z = R$	Z is independent of frequency, since it has no imaginary component, but only a real component. The current through a resistor stays in phase with the voltage across the resistor.	
<b>Inductor</b>	$E = L \frac{di}{dt}$	$Z = j\omega L$	Z increases with the frequency. Inductors have only an imaginary component. The current is 90 degrees phase-shifted with respect to the voltage.	
<b>Capacitor</b>	$I = C \frac{dE}{dt}$	$Z = \frac{1}{j\omega C}$	Frequency behavior of C is opposite to that of L. Z decreases with increasing frequency. Capacitors have only an imaginary component. The current is -90 degrees phase-shifted with respect to the voltage.	

Table 2.1: Common electrical elements, equations for their current vs voltage relationship, their impedance, their characteristics and their Nyquist representation.

The general equivalent circuit of the electrode/electrolyte interface consists of three parts: a resistor representing the electrolyte resistance,  $R_e$ , in series with the parallel combination of a capacitor representing the double layer capacitance,  $C_{dl}$ , and Faradaic impedance,  $Z_F$ , describing the electrochemical reaction (Randles circuit – Figure 2.12). The electrolyte resistance,  $R_e$  ( $\Omega \cdot \text{cm}^2$ ) is the resistance to current flow through the electrolyte. It is proportional to the electrolyte resistivity  $\rho$ .

The charge transfer resistance,  $R_t$ , is the resistance associated with the charge transfer mechanism for electrode reactions. This is the resistance to electrons crossing the interface. It is defined as the inverse of the partial derivative of the Faradaic current density ( $j_F$ ) with respect to potential ( $E$ ):

$$R_t = \left( \frac{\partial j_F}{\partial E} \right)^{-1} \quad (14)$$

Combinations of pure resistors, capacitors, or inductors do not necessarily describe the response of all systems. To model the behavior of real electrochemical systems,

distributed elements are used, among which the constant-phase element (CPE) and the Warburg impedance.

### **Constant Phase Element (CPE)**

The impedance response for electrochemical systems often reflects a distribution of time constants that is commonly represented in equivalent electrical circuits as a constant-phase element (CPE). The impedance of a CPE is given by:

$$Z_{\text{CPE}} = \frac{1}{Q(j\omega)^\alpha} = \left( \frac{1}{Q\omega^\alpha} \times \left[ \cos\left(\frac{\alpha\pi}{2}\right) - j\sin\left(\frac{\alpha\pi}{2}\right) \right] \right) \quad (14)$$

It is defined by two parameters  $Q$  and  $\alpha$ . It can be reduced to a pure resistor, capacitor or inductor when  $\alpha = 0$ ,  $\alpha = 1$  and  $\alpha = -1$ , respectively. When  $\alpha = 1$ ,  $Q$  has units of a capacitance ( $\text{F}\cdot\text{cm}^{-2}$ ), when  $\alpha \neq 1$ ,  $Q$  has units of  $\text{s}^\alpha\Omega^{-1}\text{cm}^{-2}$ . If plotting the absolute value of the imaginary part of the impedance as a function of frequency, in logarithmic coordinates the resulting curve is a straight line with a slope equal to  $-\alpha$ . This  $\log|Z_j|$  vs  $\log f$  representation is recommended since it allows to get rid of the electrolyte resistance. The  $Q$  parameter can be obtained from the imaginary part of the impedance as follows:

$$Q = \frac{1}{Z_j(f)(2\pi f)^\alpha} \times \sin\left(\frac{\alpha\pi}{2}\right) \quad (15)$$

A CPE behavior can be attributed to a distribution of time constant either along the area of the electrode (surface distribution) or along the electrode axis (normal distribution) [28-31]. A surface distribution could arise from surface heterogeneities (grain boundaries, etc), or from geometry-induced non-uniform current and potential distributions. A normal distribution may be attributed to changes in the conductivity of films or porosity. If the CPE behavior is assumed to be associated with surface distributed time constants for charge-transfer reactions, then it is possible to apply the equation derived by Brug *et al.* to calculate the effective capacitance,  $C_{\text{eff}}$ , associated with the CPE:

$$C_{\text{eff}} = Q^{1/\alpha} (R_e^{-1} + R_t^{-1})^{(\alpha-1)/\alpha} \quad (16)$$

In the case of a blocking electrode ( $R_t \rightarrow \infty$ ) this equation becomes:

$$C_{\text{eff}} = Q^{1/\alpha} (R_e^{-1})^{(\alpha-1)/\alpha} \quad (17)$$

In the case of an R//CPE circuit, the CPE parameters  $\alpha$  and  $Q$  can be graphically obtained following the method presented by Orazem *et al.* [28]. The parameter  $\alpha$  is calculated from the slope of the  $\log |Z_j|$  vs  $\log f$  curve in the high frequency range and  $Q$  is obtained from  $\alpha$ . They may be interpreted in terms of dielectric properties of the material. If the dielectric response can be associated with an effective capacitance  $C_{\text{eff}}$ , the dielectric constant  $\epsilon$ ,  $\epsilon_0$  (the permittivity of vacuum  $\approx 8.854 \times 10^{-14}$  F.cm<sup>-1</sup>) and film thickness  $d$  may be obtained from:

$$C_{\text{eff}} = \frac{\epsilon \epsilon_0}{d} \quad (18)$$

### Warburg

The Warburg impedance is associated with one-dimensional diffusion of  $X_i$  species, in an infinite stagnant medium and is given by:

$$Z_i = \frac{1}{(k_i \sqrt{j\omega})} \quad (19)$$

where  $k_i$  is a Warburg coefficient, dependent on many parameters such as the diffusion of species  $X_i$ , the reaction rate, the bulk concentration of species  $X_i$  and the potential.

### Equivalent circuit

One of the problems with the use of equivalent circuits is that different circuits can have the same impedance signature. This raise questions about the physical meaning of model parameters. The Randles circuit, shown in Figure 2.12, can be used in the description of simple electrochemical systems, such as those represented by the impedance diagrams shown above.

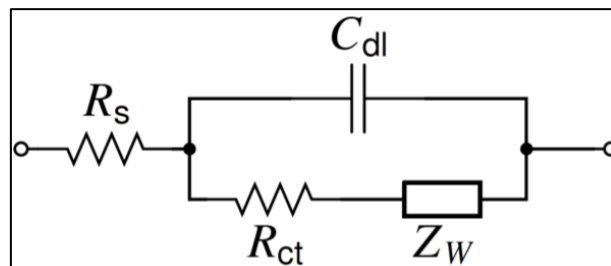


Figure 2.12: Randles circuit [28].

Although the Randles circuit satisfactorily represents many electrochemical systems, more elaborate models become necessary in the description of more complex systems, in which adsorption and/or diffusion effects, surface heterogeneity, among others may be present. Whenever the speed of an electrochemical reaction is strongly influenced by the diffusion of a chemical species to or from the electrode surface, it is necessary to include a new element in the proposed equivalent circuit called the Warburg impedance ( $Z_w$ ). Such a situation may occur when the surface of the electrode is coated with some type of film. In these cases, the potential and current are out of phase by  $45^\circ$ , causing the real and imaginary components of the impedance to have the same values over a frequency range. The extent of this range may be higher or lower, depending on the characteristics of the system.

### 2.4.2. Electrochemical Impedance Spectroscopy (EIS) setup

The electrochemical experiments were conducted at room temperature in KOH solutions at pH 10 +/- 0.1 with KCl 0.2 M as supporting electrolyte. EIS measurements were carried out under controlled hydrodynamic conditions using the RDE technique (Pine Research Instrumentation, Durham, NC, USA). The counter-electrode was a large titanium-based metallic grid placed below the working electrode. The reference electrode was a mercury/mercury oxide electrode (Hg-HgO, KOH 1M). This three-electrode setup was controlled by a Gamry Reference 600 potentiostat (same configuration as Figure 2.8) however, one potentiostat was used. The applied frequency ranged used was  $10^5$  Hz to 1 Hz with 10 points per decade. The sinusoidal perturbation was 10 mV.

## 2.5. Surface characterization techniques

### 2.5.1. Atomic Force Microscopy (AFM)

The surface topography of the films was studied with an atomic force microscope (Multimode 8 FM from Bruker) in tapping mode. This technique is used to evaluate the surface morphology of nanometric films and, consequently, to investigate three-dimensional nanostructures. It is possible to obtain the average grain size and surface roughness. The microscope consists of a flexible cantilever, with silicon or silicon nitride probes, with have a conical or pyramidal shape. The microscope also contains a scanning system, which generally uses piezoelectric ceramics capable to moving in three dimensions (x, y and z) with angstroms accuracy. The analysis consists of sweeping the sample surface, with the probe located in the cantilever. During the scanning the probe approaches the sample and begins to deflect due to the forces (attraction or repulsion) between sample and probe, and this

deflection will be detected by a laser beam that is incident on the upper side of the cantilever and reflected to a four-quadrant sensor. This sensor provides the deflection information for the feedback system, thereby correcting the vertical movement of the piezoelectric ceramic so that the tip remains in contact with the sample. The image will be formed according to the number of steps relative to the vertical movement of the piezoelectric ceramic that was recorded in a matrix [32,33].

### 2.5.2. Profilometer

This technique consists of sweeping the sample surface with a diamond-tip needle. When the tip needle locates the film substrate interface, it begins to move vertically. A linear variable differential transformer (LVTD) sensor coupled to the tip needle produces the electrical signals corresponding to the tip needle movement. These analog signals are then converted into a digital format and the software provides the thickness values [34,35]. In this research a profilometer Tencor P-10 was used.

### 2.5.3. X-ray diffraction (XRD)

X-ray diffraction (XRD) measurements were done to analyze the crystalline structure of the ZnO layers using PANalytical Empyrean apparatus with CuK radiation (1.5408 Å). This technique is used to identify the crystalline phases present in the material, preferential orientation of the planes, analysis of the composition and size of the crystallite, as long as the structure of the material presents a long-range organization. A monochromatic X-ray beam reaches the surface of the material, and an atomic distribution of the crystalline materials will cause the phenomenon of incident X-ray diffraction. From the measurement of the diffraction angles and their intensities it is possible to identify the crystalline structure of the material. After the beam incidence, scattered waves must interact constructively between them (the scattered waves across the planes of the atoms of a crystal must be in phase). Figure 2.13 shows a schematic of the diffraction phenomenon [36–39].

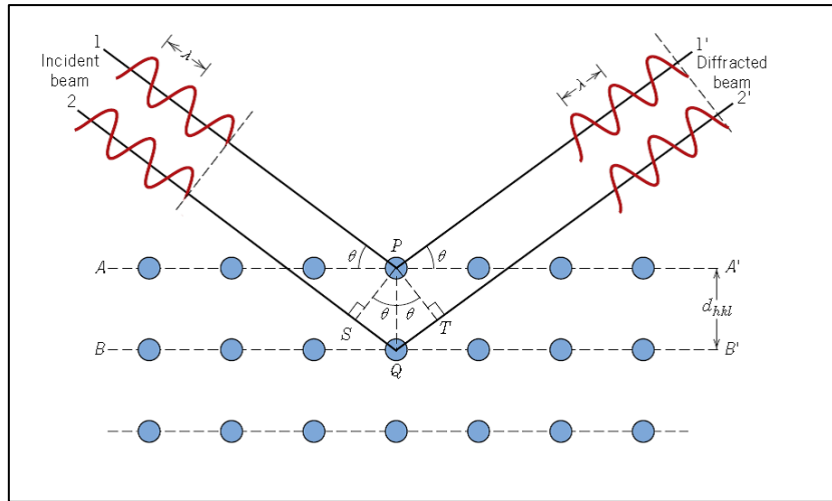


Figure 2.13: X-ray diffraction by a crystal to demonstrate Bragg's law [36-39].

The diffraction conditions are expressed by the Bragg equation 20, where  $n$  is a positive number related to the diffraction,  $\lambda$  is the wavelength of X-rays and  $d$  is the interplanar distance of the crystal.

$$2d \sin \theta = n\lambda \quad (20)$$

When  $n$  is an integer (1, 2, 3 etc.) the reflected waves from different layers are perfectly in phase with each other and produce a bright point on a piece of photographic film. Otherwise the waves are not in phase and will either be missing or feint.

#### 2.5.4. Scanning Electron Microscopy (SEM)

Top-view imaging was performed by conventional scanning electron microscopy (SEM, SU3500, Hitachi). This technique is used to evaluate the surface of materials from high resolution images of the area to be analyzed. The images are obtained from the incidence of an electron beam that scanner the sample surface (Figure 2.14) [40-42].

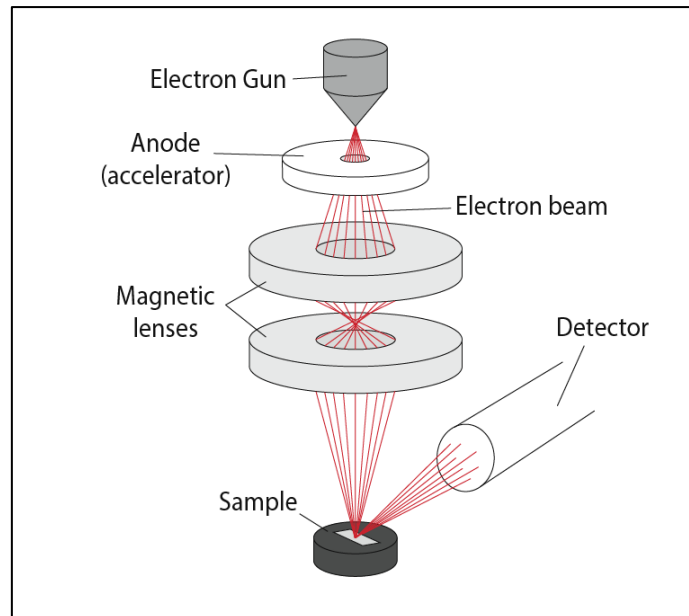


Figure 2.14: Schematic of scanning electron microscope [40-42].

The electron beam is generated from a filament, usually tungsten, by thermionic effect. The beam is then accelerated in a high vacuum through a difference potential, being focalized through electromagnetic lenses at a point on the surface of the sample, where the scanning process will begin at the desired region of the sample. The interaction between the electron beam and the surface atoms will produce various phenomena such as: secondary electron emission, electron backscattering, Auger electron, characteristic X-rays, or another photon emission. From the detection of secondary and backscattered electrons it is possible to form the image of the topography of the sample or to obtain a chemical contrast of the material, respectively. The distinction of the type of electrons is made by the difference of energies. The most common imaging mode collects low-energy ( $<50$  eV) secondary electrons. Consequently, they can produce very high-resolution images of a sample surface, revealing details less than 1 nm in size. Backscattered electrons are incident electron beam that suffered elastic collisions (when there is a change of direction without significant energy loss) with surface atoms. The backscattering will occur from the collision between the electrons and elements present in the material that has a high atomic number (the higher the atomic number of the material in a region, the brighter the image obtained after the signal detection). Thus, it is possible to acquire images with different contrasts, depending on the atomic number of the atoms present in each surface region [40–42].

### 2.5.5. Scanning transmission electron microscope (STEM)

This technique is similar to scanning electron microscope (SEM). An electron gun generates a beam of electrons that is focused by a series of lenses to form an image of the electron source at a specimen [43,44]. This equipment generally uses FEG electron sources because of its consistency and high brightness characteristics. The resolution of the STEM is determined mainly by the diameter of the beam. Due to the use of lenses to focus the beam, the resolution is limited by spherical aberration. However, STEM aberration correctors are already incorporated into the microscope column to minimize this problem. The beams that leave the interaction with the sample are collected by special detectors. These detectors process the information to form the image or obtain compositional information. The main detectors are lightfield (BF), annular darkfield (ADF) and high angle annular darkfield (HAADF). When the electron beam interacts with a sample, the Rutherford's scattering phenomenon occurs, where incoherent beams are scattered at high angles. These beams are collected by the HAADF detector and are of great importance as they provide information on the chemical composition of the sample. The type of contrast that is formed is called contrast "Z", and this type of contrast is sensitive to the thickness variation of the material [43,44].

### 2.5.6. Energy Dispersive spectroscopy (EDX)

The “bulk” composition of the films was determined by energy dispersive X-ray spectroscopy (EDX, UltraDry EDX detector and Thermo Scientific software NSS 312) with an acceleration voltage of 5 kV. Using such low voltage, information is limited to the top layer of the analyzed sample, which is rather important for investigation of thin films. In return, only low energy X-rays are detected, and some elements are not visible.

The EDX is a SEM attachment that allows a fast analysis of the composition of the sample with micrometric resolution. It is a mainly qualitative technique, but also quantitative under controlled conditions, being able to identify elements from atomic numbers of boron to uranium. The analysis basically consists of the beam incidence on a given material. By focusing a beam on the surface of the sample, the incident electron can interact with an electron from the inner shell of the electronic cloud of an atom, and as a result, the ejection of an electron can occur, creating an electron hole. In consequence electrons belonging to external layers or sublayers transit to the internal layer to fill the vacancy left by the ejected electron. This energy gap (from the transition of electrons from outer layers to inner layers) is released in the form of an X-ray. Thus, for each atom the energy levels are well defined and characteristic, the energy of the X-ray is also specific for each atom. In other words, the X-



ray energy contains information about the atom from which it was emitted, and it is possible to identify the chemical composition of the sample [45].

### 2.5.7. Focused ion beam (FIB)

Some high-resolution cross-sectional images of this thesis were obtained with a focused ion beam scanning electron microscope (FIB-SEM, FEI Helios NanoLab 600i, TLD, 2kV). This technique is a high-resolution microscopy system that consists of two different analysis devices, the FIB that generates an ion beam, and the SEM that generates an electron beam (Figure 2.15). This microscope has the ability to micro-usinate samples with high precision and generate images provided by the ion beam or the electron beam in conjunction with non-destructive analysis (imaging and spectroscopy), preserving the possibility of both beams operating independently or simultaneously in the same sample area [46-48]. The specialty of the FIB is the combination of high image resolution (less than 10 nm) with the topographic and contrast information of the materials analyzed. The ion beam is generated from a source of liquid metal ions (LMIS). This liquid metal ion flows through a thin needle of Tungsten until its tip, from where it is extracted by an emission field. The large negative potential between the needle and the electrode generates an electric field at the tip needle. The equilibrium between the electrostatic force and the surface tension of the tip needle wetted by the liquid metal, results the formation of the Taylor cone at the tip needle, from where the ion beam is emitted. The ion column consists of two lenses, a condenser and an objective, to define the beam and then focus it on the sample. The diameter and shape of the beam determine the resolution of the image and the accuracy of the micro-machining performed on the sample. Generally, the smaller diameter beam has the better resolution achieved and more precise the chopping will be. Detectors such as SEM can be used to detect electrons and X-rays emitted through the interaction between ions and sample. The ions that are scattered from the sample are also detected by several types of detectors, such as electronic charge multipliers and scatter particles mass selection [46-48].

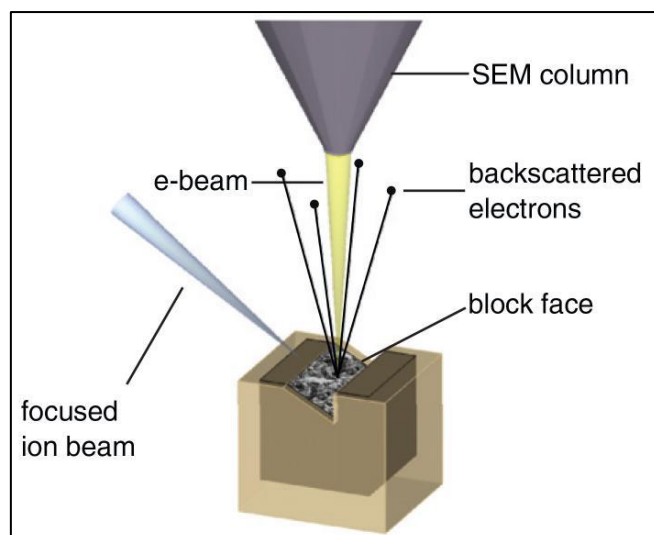


Figure 2.15: Schematic of a FIB-SEM microscope [46].

### 2.5.8. X-ray Photoelectron Spectroscopy (XPS)

The chemical composition of the surface was assessed by X-ray photoelectron spectroscopy (XPS) using an Al-K $\alpha$  X-ray source (Thermo VG) and a cylindrical mirror analyzer (RIBER). When a surface is excited by photons, the emitted electrons are designated by photo-electrons, being the energy of these electrons characteristic of the element from where they were emitted. The XPS spectra are obtained by irradiating a sample surface with a beam of X-rays while simultaneously measuring the kinetic energy and electrons that are emitted from the top (1-10 nm) of the sample under analysis (Figure 2.16). This spectrum is recorded by counting ejected electrons over a range of electron kinetic energies. Peaks appear in the spectrum from atoms emitting electrons of a particular characteristic energy. The energies and intensities of the photoelectron peaks enable identification and quantification of all surface elements [49,50]. The limit of detection of this technique is usually not more than 1% in atomic percentage, with the analysis thickness is 5 nm. When carrying out the quantitative analysis, attention must be paid to the peak intensities of the photoelectrons. The sensitivity (element detection) depends on the effective section of this element and the background noise produced by the other elements [49–52].

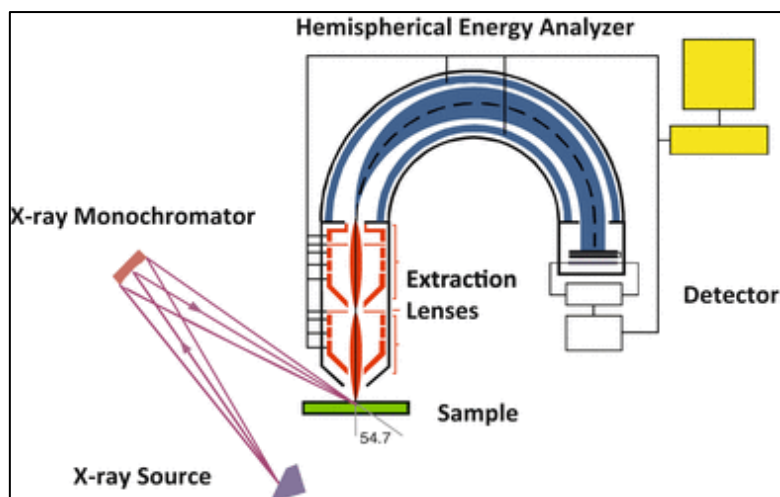


Figure 2.16: Schematic of a typical modern high-resolution X-ray photoelectron spectrometer [52].

In XPS measurements, following core ionization by a photoelectron emission, an outer shell electron can fill the created vacancy and the energy released can result in the emission of an Auger electron. This latter is defined by its kinetic energy. The Auger parameter ( $\alpha$ ) is then defined by the sum of the kinetic energy of the Auger electron and the binding energy of the photoelectron. This parameter is particularly useful for chemical state analysis and can be used without interference of surface charging. Moreover, it is of high interest when studying corrosion of zinc. Indeed, as shown by the PhD. thesis of B. Lefevre [53] and more recently of E. Diler [54], only this parameter is useful to identify the different species.

## 2.6. References

- [1] K. Wasa, Handbook of Sputtering Technology, 2nd Edition, 2012;
- [2] R. Behrisch, Sputtering by Particle bombardment, Springer, Berlin, 1981;
- [3] K. Seshan, Handbook of thin film deposition processes and techniques, William Andrew Publishing, Norwich, EUA, 2002;
- [4] D. Depla, S. Mahieu, J. E. Greene, Handbook of Deposition Technologies for Films and Coatings, 3rd Edition, Chapter 5 - Sputter Deposition Processes, 2010;
- [5] K. Seshan, Handbook of thin-film deposition processes and techniques – Principles, methods, equipment and applications, 2nd Edition, Noyes Publications/William Andrew Publishing, Norwich, New York, 2002;
- [6] B. E. Aufderheide, Coatings Technology Handbook. Sputtered Thin Film Coatings, (available in): <http://www.crcnetbase.com>;

- [7] Bunshad, R.F. Deposition Technologies for Films and Coatings. USA: Noyes Publications, 1982;
- [8] Available in: <https://www.sigmaaldrich.com/materials-science/material-science-products.html>.
- [9] E. Alfonso, J. Olaya, and G. Cubillos, Thin film growth through sputtering technique and its applications, Science and Technology, InTech, 2012;
- [10] A. Znamenskii, V. Marchenko, Thin film materials technology: sputtering of compound materials, Technical physics, Vol. 43, No 7 (1998);
- [11] B. N. Chapman, Glow discharge processes: sputtering and plasma etching, Wiley, New York, 1980;
- [12] Available in: <http://www.semicore.com/news/94-what-is-dc-sputtering>;
- [13] M. Ohring, The Materials Science of Thin Films, Academic Press Inc., San Diego, 1992;
- [14] S.Y. Chu, W. Water, J.T. Liaw, Journal of the European Ceramic Society 23 (2003) 593–1598;
- [15] G. Cao, Nanostructures & Nanomaterial: Synthesis, properties & applications, Imperial College Press, 2004;
- [16] Available in: [http://www.msi-pse.com/magnetron\\_sputtering.htm](http://www.msi-pse.com/magnetron_sputtering.htm);
- [17] C. A. Bishop, Vacuum Deposition onto Webs, Films and Foils (Second Edition), 20 - Magnetron Sputtering Source Design and Operation, 2011;
- [18] Van de Pol, F. C. M.; Blom, F.R.; Popma, J.A. R.F. planar magnetron sputtered ZnO films I: structural properties. Thin Solid Films, v. 204, p. 349-364, 1991;
- [19] J. A. Thornton. Influence of apparatus geometry and deposition conditions on structure and topography of thick sputtered coatings. Journal of Vacuum Science & Technology 11 (1974) 666-670;
- [20] O. Kluth et al. Modified Thornton model for magnetron sputtered zinc oxide: film structure and etching behavior. Thin Solid Films 442 (2003) 80-85;
- [21] J. Zhang, PEM Fuel Cell Electrocatalysts and Catalysts Layers Fundamentals and Applications, 2008;
- [22] K. Kinoshita, Electrochemical oxygen technology. John Wiley, New York, 1992;
- [23] D. A. Pletcher, First course in electrode processes. London: Electrochemical Consultancy, 1991;
- [24] A. J. Bard, Electroanalytical chemistry. Marcel Dekker, New York, 1982;
- [25] V. G. Levich, Physicochemical Hydrodynamics. Prentice-Hall, New York, 1962;

- [26] P. T. Kissinger, W. R. Heineman, Laboratory techniques in electroanalytical chemistry. Marcel Dekker, New York, 1996. P. 986;
- [27] F. Opekar, P. Beran, Rotating disk electrodes. *Journal of Electroanalytical Chemistry*, v.69, n. 1;
- [28] M. E. Orazem, B. Tribollet, *Electrochemical Impedance Spectroscopy*, Wiley, 2nd edition, 2017;
- [29] E. Barsoukov, J. R. Macdonald, *Impedance spectroscopy theory, experimental, and Applications*, 2nd, 2005;
- [30] M. E. Orazem, B. Tribollet, *Tutorials in Electrochemical Technology: Impedance Spectroscopy*, 2008;
- [31] Available in: [www.gamry.com](http://www.gamry.com);
- [32] P. Eaton, P. West, *Atomic Force Microscopy*, OUP Oxford, 2010;
- [33] G. Binnig, C. F. Quate, Ch. Gerber, Atomic Force Microscope, *Physical Review Letters*, 56 (9): 930–933, (1986);
- [34] J. M. Bennett, L. Mattsson, *Introduction to Surface Roughness and Scattering*, Optical Society of America, Washington, D.C;
- [35] K. J Stout, L. Blunt, *Three-Dimensional Surface Topography*, 2nd ed., Penton Press. p. 22 (2000);
- [36] B. Cullity, *Elements of X-ray Diffraction*, Addison-Wesley Publishing Company, 1956;
- [37] V. Pecharsky and P. Zavalij, *Fundamentals of powder diffraction and structural characterization of materials*, Springer, 2004;
- [38] M. Birkholz, *Thin film Analysis by X-ray Scattering*, Wiley, 2006;
- [39] U. Pietsch, V. Holy, and T. Baumbach, *High-resolution X-ray scattering: From thin films to lateral nanostructures*, *Advanced texts in physics*, Springer, New York, 2004;
- [40] D. J. Stokes, *Principles and Practice of Variable Pressure Environmental Scanning Electron Microscopy (VP-ESEM)*. Chichester: John Wiley & Sons (2008);
- [41] G. I. Goldstein, D. E. Newbury, P. Echlin, D. C. Joy, C. Fiori, E. Lifshin, *Scanning electron microscopy and x-ray microanalysis*, Plenum Press, New York, 1981;
- [42] J. Goldstein, *Scanning electron microscopy and x-ray microanalysis*, Springer US, 2003;
- [43] J. J. Friel, C. E. Lyman, *Tutorial Review: X-ray Mapping in Electron-Beam Instruments, Microscopy and Microanalysis*. 12 (1): 2–25, 2006;
- [44] L. Reimer, R. Kohl, *Transmission Electron Microscopy Physics of Image Formation*. Springer, 2008;
- [45] J. Goldstein, *Scanning Electron Microscopy and X-Ray Microanalysis*. Springer, 2003;

- [46] Available in: <http://www.fibics.com/fib/tutorials/introduction-focused-ion-beam-systems/4/>;
- [47] J. Orloff; M. Utlaut; L. Swanson, High Resolution Focused Ion Beams: FIB and Its Applications. Springer Press, 2003;
- [48] Available in: [https://www.embl.de/services/core\\_facilities/em/services/fibsem/](https://www.embl.de/services/core_facilities/em/services/fibsem/);
- [49] Handbook of The Elements and Native Oxides, Available in: [http://www.xpsdata.com/Handbook\\_Details.pdf](http://www.xpsdata.com/Handbook_Details.pdf);
- [50] Available in: <https://xpssimplified.com/whatisxps.php>;
- [51] J.F.Watts, J.Wolstenholme, An Introduction to Surface Analysis by XPS and AES, Wiley & Sons, Chichester, UK, 2003;
- [52] R. T. Haasch, X-Ray Photoelectron Spectroscopy (XPS) and Auger Electron Spectroscopy (AES). Springer, New York, NY, 2014;
- [53] B. Lefevre. Corrosion des aciers revetus de zinc dans les zones confinées des carrosseries automobiles (2004). <https://pastel.archives-ouvertes.fr/pastel-00002339/document>;
- [54] E. Diler. Étude de la corrosion atmosphérique du zinc et zinc-magnésium, en milieu marin (2014). <https://tel.archives-ouvertes.fr/tel-00725313/document>;

---

DC study of ORR on textured ZnO layers

---

**Abstract**

In this chapter, thin smooth columnar ZnO films were deposited by rf-magnetron sputtering on copper substrates. The layers were characterized by XRD, XPS, EDX, FIB-SEM and AFM. Oxygen reduction at the ZnO surface was investigated in alkaline electrolyte under controlled hydrodynamic conditions using the rotating disk electrode (RDE) and the rotating ring disk electrode (RRDE) techniques. It was shown that ORR follows both the direct and indirect reaction pathways as a non-negligible flux of hydrogen peroxide was evidenced. The textured layers suffered from mechanical instability that was found to be potential-dependent. Also, an Annex was added with additional information about the first measurements to find the best conditions to obtain well-oriented ZnO films.

*A modified version of this chapter has been submitted to Materials Chemistry and Physics: Synthesis, characterization and oxygen reduction activity of textured ZnO films, J. Soares Costa, M. Prestat, B. Lescop, S. Rioual, L. Holzer, B. Tribollet, D. Thierry.*

**3.1 Introduction**

As mentioned in Chapter 1, the oxygen reduction reaction (ORR) is one of the major cathodic reactions in corrosion science and more generally in electrochemistry. Although various reaction mechanisms have been proposed in the literature depending on the electrode material and testing conditions [1-3], a common feature consists of the competition between two parallel pathways, as shown in Figure 3.1.

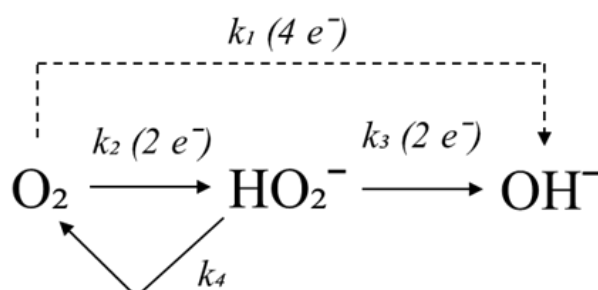
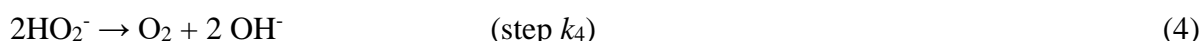
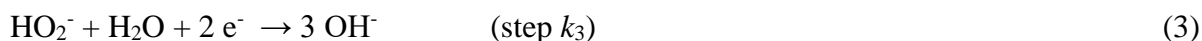
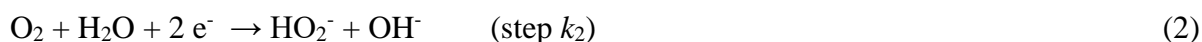
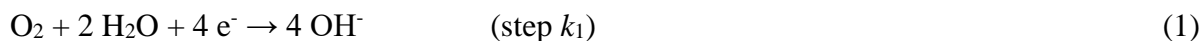


Figure 3.1: Simplified oxygen reduction reaction mechanism in alkaline medium.

Oxygen can be reduced directly into hydroxyl ions (step  $k_1$ ) or indirectly with hydrogen peroxide as intermediate species (steps  $k_2$  and  $k_3$ ). Hydrogen peroxide may also be chemically decomposed on the electrode surface (step  $k_4$ ) [3]. The (electro)chemical reactions are written as follows:



Depending on the reaction pathway, the number,  $n$ , of electrons (per reduced molecule of oxygen) varies between 2 and 4. The detection of hydrogen peroxide and therefore the relevance of the indirect pathway is usually carried out by collection-based techniques, such as rotating-ring disk electrode (RRDE) [4,5] and double-channel electrode flow cell [6-8]. Ideally this is done with a smooth dense working electrode (where ORR takes place) that is coplanar with the collecting electrode at which oxidation of hydrogen peroxide occurs.

The electrochemical behavior of ZnO towards ORR is not well understood yet as described in the analysis of the state-of-the-art and as recalled by Cole's recent review [9]. Notably different results were also obtained with native (passive) zinc oxide layers on bare zinc [10-11] and thicker ZnO coatings (ca. hundreds of nanometers) that were artificially produced [12-13]. In almost all these studies, the ZnO layers displayed a rather complex microstructure with *e.g.* multi-scale porosity, heterogeneous thickness or rough surface.

The aim of the present work was to prepare a first type of ZnO layers that could serve as model electrodes to study ORR under controlled hydrodynamic conditions using the rotating disk electrode (RDE) and rotating ring disk electrode (RRDE) techniques in alkaline solution at room temperature. The targeted nanostructure was dense and columnar with a (002) orientation. Hence the layers were referred to as "textured ZnO". The films were produced by radio-frequency (rf) magnetron sputtering using a ZnO target. The crystalline structure and the chemical composition of the films were investigated with X-ray diffraction (XRD), X-ray photoelectron spectroscopy (XPS) and energy-dispersive X-ray spectroscopy (EDX). Their morphology and their microstructure were characterized by atomic force microscopy (AFM), conventional scanning electron microscopy (SEM) and focused ion beam



scanning electron microscope (FIB-SEM). Results on the mechanical stability and electrochemical activity of the ZnO films as well as on the relevance of the direct reduction pathway are presented and discussed.

### 3.2. Experimental

#### 3.2.1 Synthesis of the ZnO layers

ZnO films were deposited on copper substrates by radio-frequency magnetron sputtering (Univex 350, Oerlikon) using a ZnO target. The procedure to determine the sputtering parameters for ZnO deposition is described in the Annex of this Chapter. Copper cylinders substrates (5 mm diameter, 4 mm height) were micro-machined from commercially available rods (purity > 99.95%, GoodFellow) to fit the (RRDE) setup that exposes only the top surface. After machining, the substrates were grinded with SiC paper (P2500 and P4000 for 60 s each) using water as a lubricant. The finishing of the surface was done with a polishing cloth and polycrystalline diamond suspensions (3  $\mu\text{m}$  and 1  $\mu\text{m}$ , each for 180 s). The substrates were then ultrasonically cleaned in ethanol, rinsed in deionized water and air-dried.

For sputtering deposition, the working chamber which was vacuumed to reach a base pressure of  $3 \times 10^{-7}$  mbar. The substrates were fixed at a distance of ca. 10 cm parallel to the ZnO target surface. The films were deposited for 90 minutes with a mixture of reactive gas (Argon: O<sub>2</sub>, 2:1) inside the chamber. The gas purities were 99.9996% for Argon and 99.9995% for O<sub>2</sub>. Pre-sputtering was carried out for 30 min to clean and equilibrate the target surface prior to deposition. The same conditions were used for pre-sputtering and sputtering, except deposition time. During deposition, the total pressure was kept at  $2 \times 10^{-2}$  mbar. The input power at the target was 75 W.

#### 3.2.2 Characterization of the ZnO layers

X-ray diffraction (XRD) measurements were done to analyze the crystalline structure of the ZnO layers using PANalytical Empyrean apparatus with CuK radiation (1.5408 Å). The chemical composition of the surface was assessed by X-ray photoelectron spectroscopy (XPS) using an Al-K $\alpha$  X-ray source (Thermo VG) and a cylindrical mirror analyzer (RIBER). The “bulk” composition of the films was determined by energy dispersive X-ray spectroscopy (EDX, UltraDry EDX detector and Thermo Scientific software NSS 312) with an acceleration voltage of 5 kV. The surface topography of the films was studied with an atomic force microscope (Multimode 8 FM from Bruker) in tapping mode. Top-view imaging

was performed by conventional scanning electron microscopy (SEM, SU3500, Hitachi) to evaluate the aspect of the layers. High-resolution cross-sectional images obtained with a focused ion beam scanning electron microscope (FIB-SEM, FEI Helios NanoLab 600i, TLD, 2kV) enabled to characterize the internal microstructure of the ZnO layers and to measure their thickness.

### 3.2.3 Electrochemical measurements

All electrochemical experiments were conducted at room temperature in KOH solutions at pH 10 +/- 0.1 with KCl 0.2 M as supporting electrolyte. ORR was investigated under controlled hydrodynamic conditions using the (R)RDE technique (Pine Research Instrumentation, Durham, NC, USA). The working electrode (ZnO thin film on top of the copper substrate, diameter 5 mm) was surrounded by a concentric gold ring (width 1 mm) separated from the disk by a 0.75 mm wide Teflon gap. The collection efficiency of the ring was beforehand estimated to be 23 %. The counter-electrode was a large titanium-based metallic grid placed below the working electrode. The reference electrode was a mercury/mercury oxide electrode (Hg-HgO, KOH 1M). This four-electrode arrangement was controlled by a bipotentiostat formed by two synchronized Gamry Reference 600 potentiostats. The potential of the ring electrode was set at + 0.950 V (vs. Hg-HgO). Disk polarization curves were recorded with a scan rate of 0.5 to 1 mVs<sup>-1</sup>. All the electrochemical measurements were done in triplicate.

## 3.3. Results and discussion

### 3.3.1 Film characterization

Figure 3.2 shows the XRD patterns of the ZnO films. Although a minor diffraction peak at 62.7° associated with (103) planes is observed, the presence of the strong (002) peak at 34° indicates a clear preferred orientation along the c-axis of the wurtzite structure. This is explained by the minimization of the surface free energy during the growth process [14]. This finding is in good agreement with the results reported in the literature [15-19] using similar conditions as in the present work.

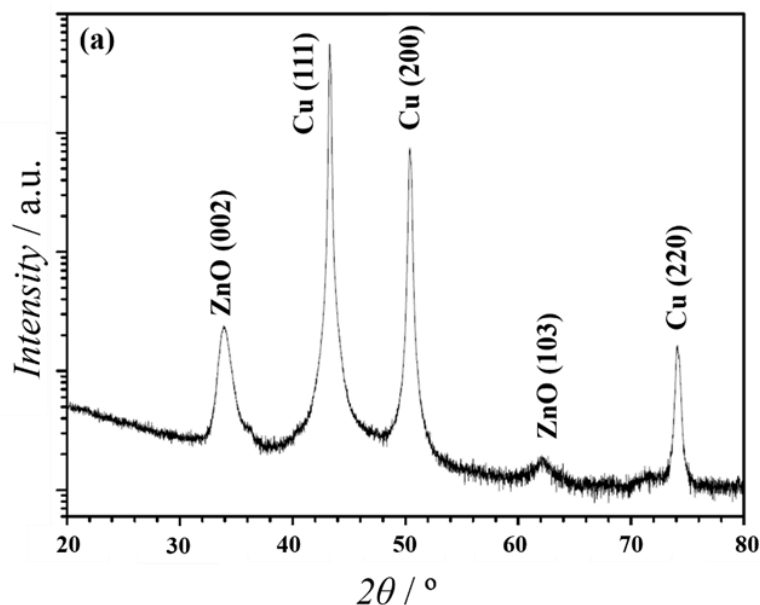


Figure 3.2: XRD diffractogram of the ZnO thin films deposited on copper substrates. Note the log-scale of the y-axis.

The XPS and Auger spectra are depicted in Figure 3.3. The O (1s) peak is located at 529.7 eV and is related to the  $O^{2-}$  in the ZnO structure (Figure 3.3a). The asymmetric tail observed at high binding energy is explained by the contribution of hydroxyl groups at the surface. The Zn ( $2p_{3/2}$ ) and Auger Zn (LMM) spectra display structures centered at 1021.46 and 989.1 eV, respectively (Figure 3.3b and 3.3c). The derived  $\alpha$  Auger parameter is thus 2010.6 eV, close to the value expected for ZnO (2010.4 eV) [13].

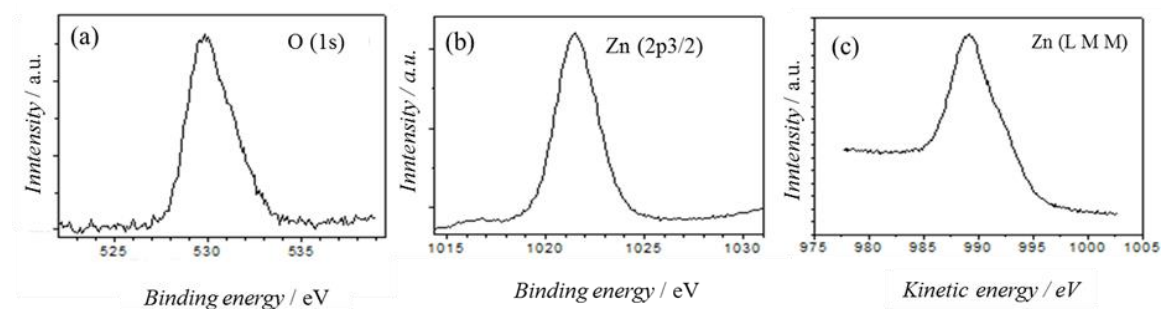


Figure 3.3: Surface analysis of the ZnO films: a) XPS spectrum of O (1s); b) XPS spectrum of Zn ( $2p_{3/2}$ ); c) Auger spectrum of Zn (LMM).

The chemical composition of the films was also measured by EDX (Figure 3.4). The results are quite reproducible (contains 5 EDX spot analysis) showing good Zn/O ratios, confirming the deposition of ZnO on the surface. The composition of the as-deposited ZnO films is close to the nominal 50:50 Zn:O atomic ratio (55:45 for the ZnO layer) within the accuracy limits of this technique.

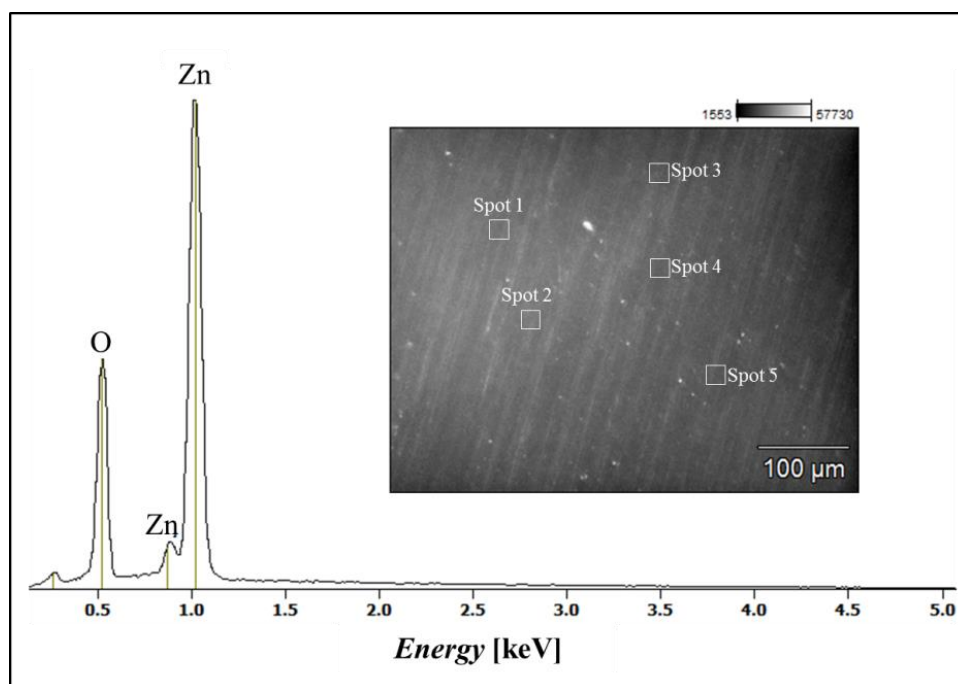


Figure 3.4: EDX spectra of ZnO films.

The microstructure of the as-deposited thin films was studied by AFM, SEM and FIB-SEM. Top-view images obtained by both SEM and AFM (Figure 3.5a and 3.5b) show “grains” of about 40 - 150 nm (for most of them) that actually corresponds to the top of ZnO columns with the (002) orientation evidenced by XRD. The internal microstructure of the ZnO layers was documented by FIB-SEM cross-sectional micrographs that gave further evidence for the columnar growth (Figure 3.6). The inset of Figure 3.6 also shows that the columns have a thickness of ca. 300 nm (for 90 min of deposition). No hint of porosity could be resolved with FIB-SEM imaging, which indicates the deposition of compact ZnO layers at the nanoscale.

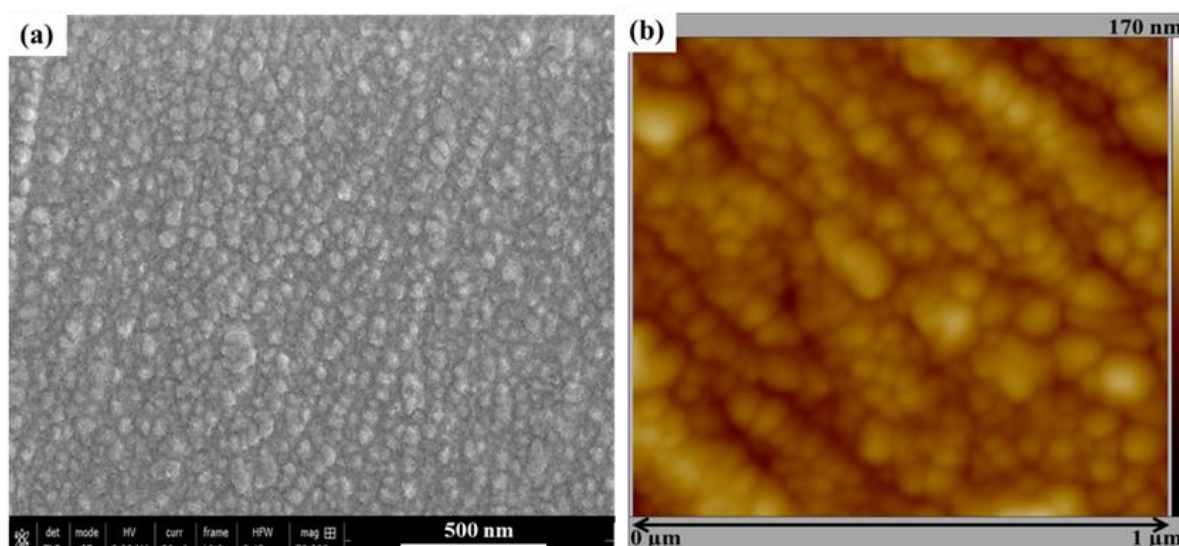


Figure 3.5: Microscopic analysis of the ZnO films: (a) SEM top-view image (b) AFM image.

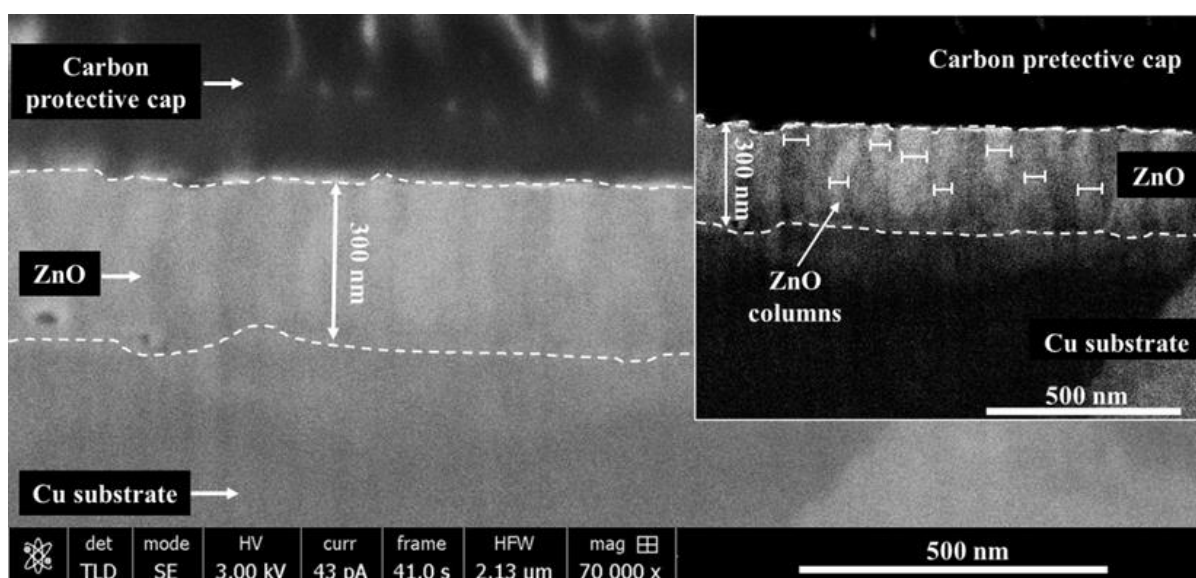


Figure 3.6: Cross-sectional FIB-SEM images of the ZnO films. Inset image (same figure revealing the columnar structure after contrast increase).

### 3.3.2 Electrochemical behaviour

The electrochemical behavior of the ZnO films towards ORR was investigated in alkaline KOH at pH 10 using the RDE technique. Based on preliminary measurements (better described in Chapter 4), the resistance ( $R$ ) of the film was measured in transverse mode.  $R$  was found to be ca. 0.3 - 0.4  $\Omega$ , and the resistivity,  $\rho$ , was therefore estimated to be ca.  $10^2 \Omega$  cm. This low resistivity value suggests high conductivity value for textured ZnO films, and being high enough was neglected the ohmic drop within the layers.

Figure 3.7 compares the polarization curves of the ZnO films and the copper substrates between open circuit potential till -0.8 V. A significant difference of activity

between ZnO and copper is observed. At -0.8 V, the current density obtained for ZnO was ca.  $-50 \mu\text{A}/\text{cm}^2$  while that of copper was ca.  $-950 \mu\text{A}/\text{cm}^2$ . This result shows that ZnO is not an efficient electrocatalyst for ORR and is in good agreement with the reports of Goux *et al.* [12] and Prestat *et al.* [13] obtained with electrodeposited ZnO.

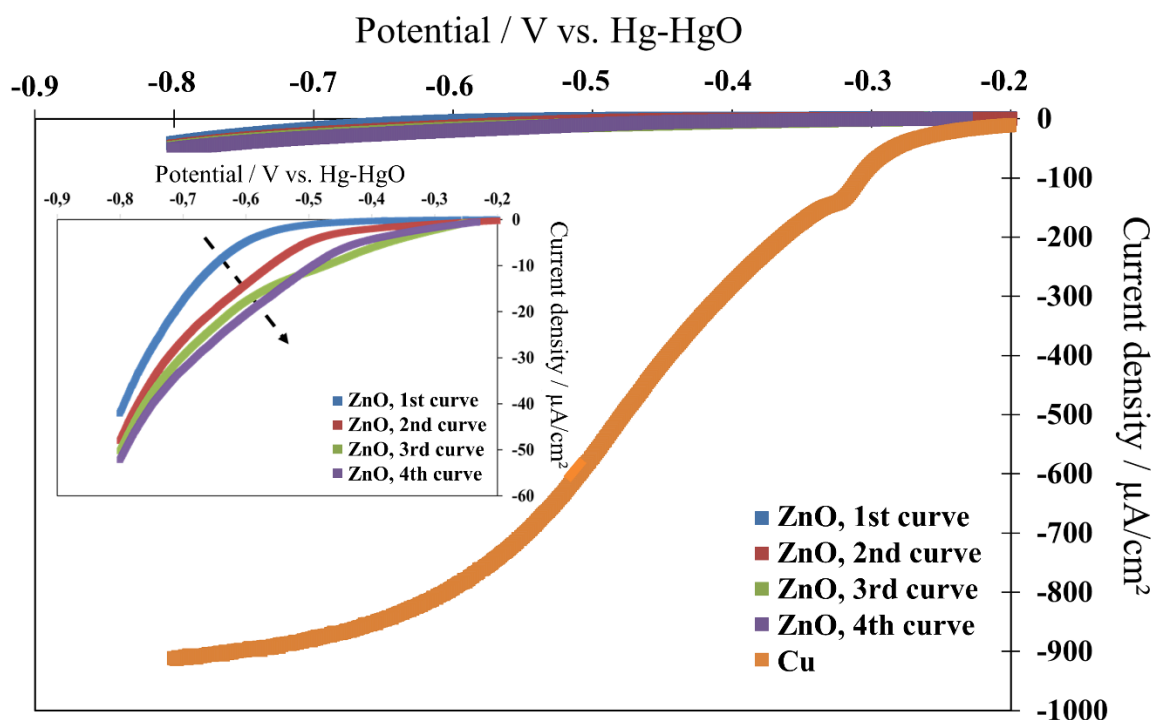


Figure 3.7: Typical disk polarization curves of ZnO and bare copper substrates. For ZnO, four consecutive curves were recorded to evaluate the ZnO stability. Inset: zoom on the polarization curves of ZnO. The arrow illustrates the steady current density increase from one curve to the next. For all curves, the disk potential scan rate was  $1 \text{ mV s}^{-1}$  and the rotation rate was 1000 rpm.

For ZnO electrodes, the polarization experiment was repeated four times (Figure 3.7 inset). It appears that the DC behavior is not stable. The increase of current density from one curve to the next suggests that the electrolyte reaches the more electrochemically active copper substrate and thereby a degradation of the ZnO films. Two hypotheses were then formulated to explain this phenomenon: polarization-induced film rupture and chemical dissolution against the electrolyte.

In order to test the first hypothesis, several polarization curves were recorded (starting from open circuit potential) till -0.2 V, -0.5 V, -0.8 V and -1.1 V on a single ZnO electrode (Figure 3.8a). After each polarization, the samples were rinsed with distilled water and dried. Then the surface of the ZnO film was investigated by SEM to search for degradation evidence (Figure 3.8b).



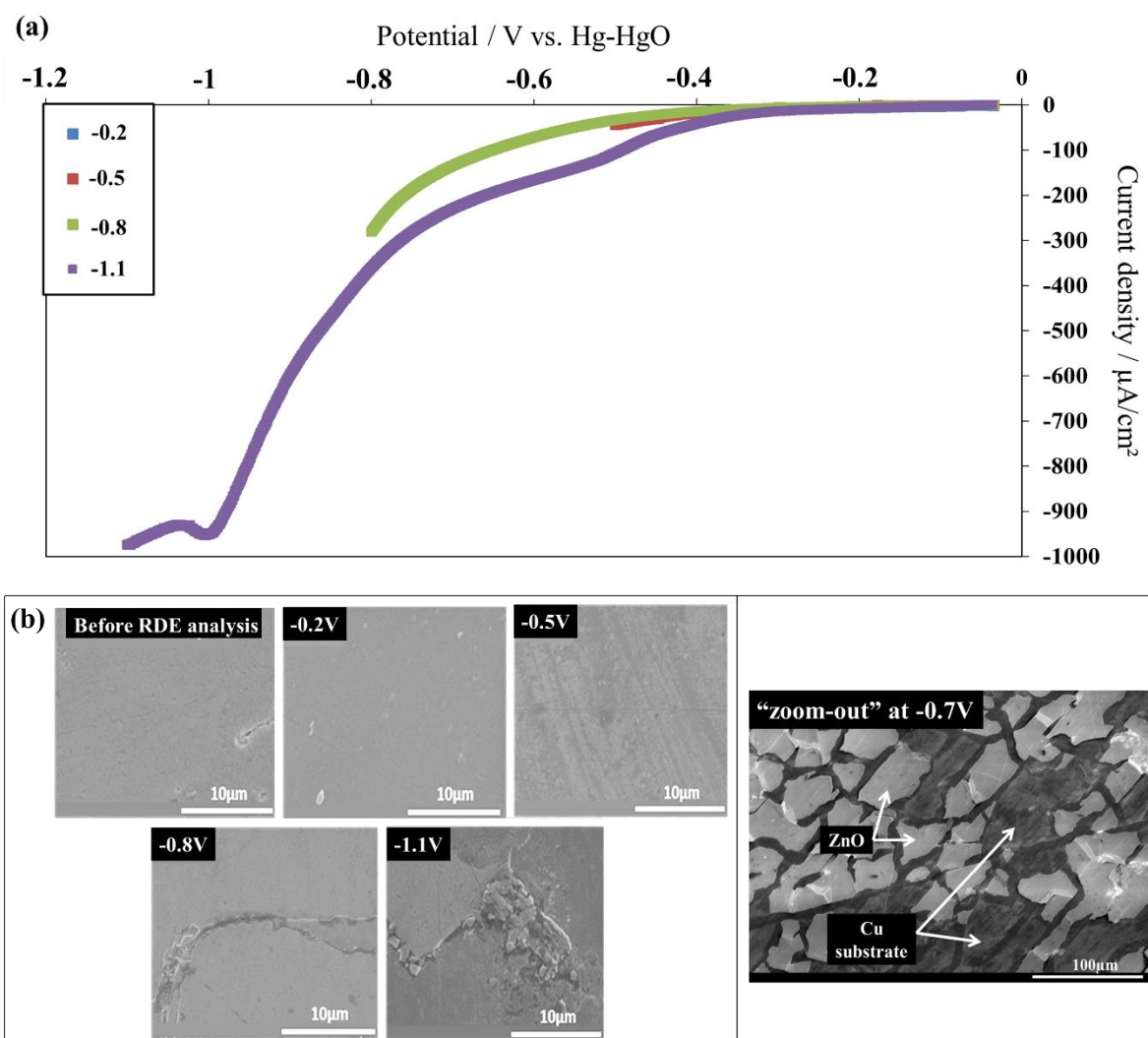


Figure 3.8: Evaluation of the critical potential for ZnO film rupture. (a) Polarization curves of a single ZnO electrode between open-circuit potential and various increasingly negative end-potentials: -0.2 V, -0.5 V, -0.8 V and -1.1 V. (b) Corresponding top-view SEM micrographs taken after each polarization. Zoom-out: example of a significant film rupturing with delamination after polarization at -0.7 V (corresponding polarization curve not shown).

At -0.2 and -0.5 V, no change of the ZnO surface is noticed and the polarization curves overlap. After the -0.8 V polarization, large cracks are visible, leading in some cases to local delamination of the ZnO film that is generally better observed with lower magnification micrographs. Typically, large cracks are found at potential more negative than ca. -0.6 V. Yet the rupture potential and the degree of damage of the layers varied from one sample to another. At the beginning of the fourth experiment (polarization till -1.1 V), the film was already cracked and exposed the underlying copper substrate. This resulted in an increase of the current density in the polarization curve. Unsurprisingly post-mortem SEM observations revealed more important damages. Since the rupture of the films clearly depends on the applied potential, it can be postulated that the stress necessary to generate the cracks might

originate from the piezoelectric properties of columnar ZnO that have been reported in the literature [15, 20-22]. This may add up to the residual stress already present in the films after deposition. It is known that, during rf-magnetron sputtering, the ZnO film formation is governed by different critical parameters such as power, sputtering pressure and gas composition [23-26]. These parameters govern the quality, the stress and the nanostructure of the deposited films. Progress in terms of mechanical stability of the films might be achieved by optimizing those parameters (provided that the compactness of the films is retained). This research activity is however beyond the scope of this Chapter.

The hypothesis of ZnO degradation due to the chemical dissolution was also considered for such phenomenon and has been reported in the literature [17, 18]. Hüpkes *et al.* in a recent review, proposed a model for the chemical etching of ZnO thin films based on the assumption that each grain boundary has a certain inherent probability to serve as an active site for etching depending on the structural material properties and etching agent [17]. Han *et al.* evaluated the dissolution of sputtered ZnO films at different pH (between 3 and 12) by measuring the concentration of  $Zn^{2+}$  cations in the solution by atomic absorption spectroscopy [18]. They demonstrated a minimal dissolution level (ca. 1 %) for 24 h of immersion at pH = 10. After a week of exposure, the same films exhibited a dissolution level of ca. 30%, indicating a slow but non-negligible chemical dissolution at this pH. Dissolution rates were higher for all other pH. In the present work, the ZnO films were exposed for 24 hours and 1 week in the same KOH solution used for the electrochemical measurements. The samples were analyzed by SEM and EDX technique (see Annex I). No change in the ZnO surface was observed regardless of duration of immersion. Though the hypothesis of a very slow dissolution (in terms of weeks) cannot be totally excluded, it cannot account for the rapid degradation of the films (in terms of minutes and hours) observed in the present study. Moreover, it is believed that chemical dissolution would lead to a more homogenous degradation of the films at the micron or submicron scale, as reported by Becker *et al.* [27] unlike the cracks shown in Figure 3.8 that clearly suggest a mechanical stress issue.



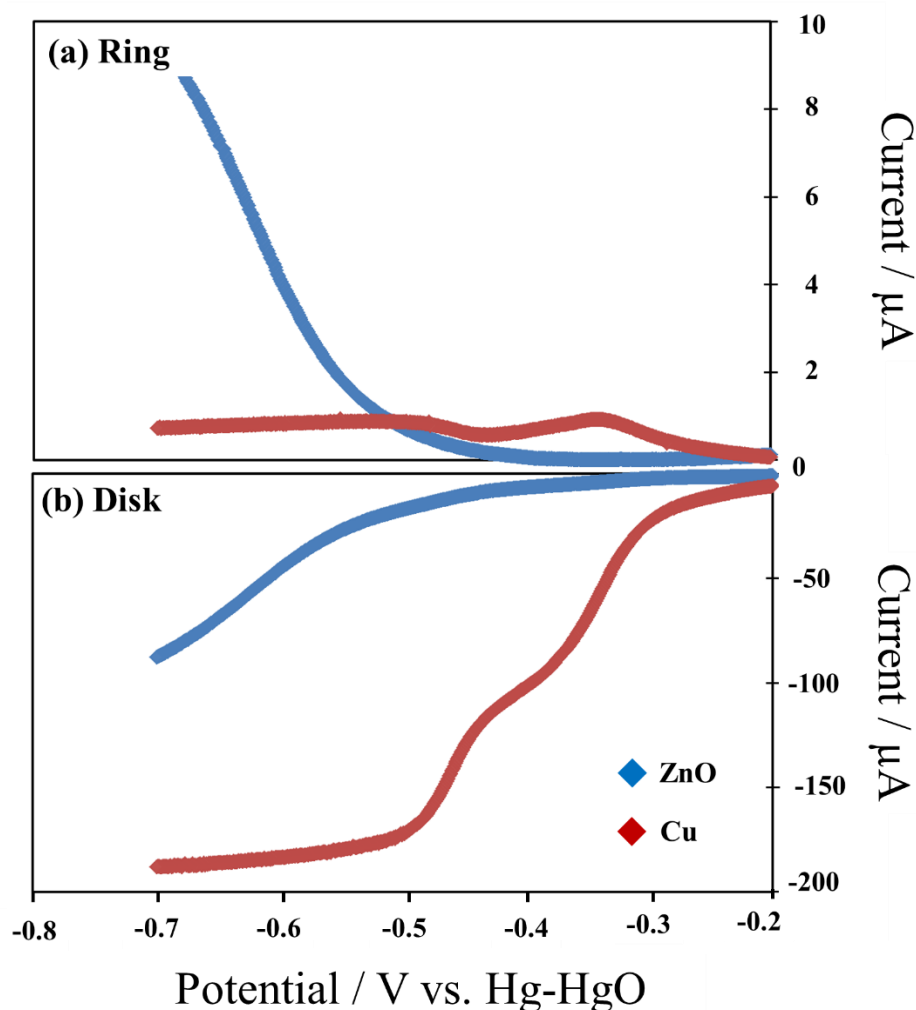


Figure 3.9: Typical ring (a) and disk (b) curves recorded during the RRDE study of ORR on ZnO thin films (blue) and Cu reference (red) in alkaline electrolyte. The potential scan rate was  $0.5 \text{ mV s}^{-1}$  and the rotation rate 1000 rpm. Note the difference of scales of the y-axis for ring and disk currents.

Figure 3.9 shows the RRDE curves of the copper substrate and the ZnO layers recorded from OCP till  $-0.7 \text{ V}$ . Due to the rupturing of the ZnO layers described above, only one scan at one rotation rate was performed, excluding thus the possibility of a Koutecky-Levich analysis for determining the mean number of exchanged electrons,  $n$ , during ORR. A first estimate of the relevance of the direct ORR pathway can be provided by the  $\left| \frac{NI_d}{I_r} \right|$  ratio where  $I_r$  is the ring current and  $I_d$  the disk current. Large values of  $\left| \frac{NI_d}{I_r} \right|$  indicate the prevalence of the direct pathway (step  $k_1$ ) while  $\left| \frac{NI_d}{I_r} \right| = 1$  evidences a 2-electron reduction through the indirect pathway (step  $k_2$  only). For copper, the ring current is very small compared to the strong ORR activity of the disk.  $\left| \frac{NI_d}{I_r} \right|$  is large (around 50) evidencing a direct reduction of oxygen. For the ZnO layers, the ring current increases steadily from  $-0.4 \text{ V}$  and

cannot be neglected. Even if the ZnO layer starts to degrade (around -0.6 V) and exposes part of the copper substrate, the generation of  $\text{HO}_2^-$  can only be attributed to ORR on ZnO. Lower  $\left|\frac{Nl_d}{l_r}\right|$  values (from 2 to 10) were obtained. At this point of our research, it can only be concluded that ORR on ZnO follows both the direct and indirect reduction pathways.

A refined quantitative estimation of the relevance of the direct pathway vs. the indirect pathway would require the recording of ring and disk curves at different convection-diffusion transport rates, as shown in [4,6,8] and therefore ZnO layers with higher mechanical stability. This type of experiments is performed in the Chapter 5 of this Ph.D. thesis in which non-textured ZnO layers are investigated.

When comparing the present findings with literature results, it seems that the way oxygen is reduced on ZnO greatly depend on the thickness (thin passive layers or “thick” deposited films) and on the growth method. Prestat *et al.* [13] studied ORR on 1200 nm thick ZnO layers electrodeposited on copper substrates with RRDE in KOH solutions (pH = 11) at room temperature. The films did not exhibit any preferential crystallographic orientation. Only a small production of hydrogen peroxide was detected at the ring electrode. The Levich equation applied under mass transport control (current plateaux) showed that the number of exchanged electrons,  $n$ , was around 4 evidencing thus the direct 4-electron pathway.

Using RDE technique, Goux *et al.* [12] investigated ORR kinetics on ZnO electrodeposited on platinum substrates in near-neutral KCl electrolyte at 70°C. The context of their work was to better understand ORR under the conditions of the ZnO synthesis, ORR being part of the electrodeposition process [28]. Koutecky-Levich plots evidenced a regular increase of the  $n$  value (from 2.2 to ca. 4) with increasingly cathodic overvoltage. Hence, while ZnO passive layers favour a 2-electron reaction with hydrogen peroxide generation [4,10,11], the 300 nm textured ZnO films of this study, like other “thick” coatings [12,13], promotes the direct reduction with a more or less significant indirect reduction contribution. The latter probably depends on parameters, such as nanostructure and texture (that are related to the growth method), as well as electrolyte composition, pH, thickness and temperature.

#### 3.4. Conclusions

ZnO thin films were produced by rf-magnetron sputtering on copper substrates. The films grow columnarly along the c-axis of the wurtzite structure perpendicular to the surface as shown by XRD and FIB-SEM analyses. The width of the columns ranges around 40 to 150 nm. AFM top-view and FIB-SEM cross-sectional images show uniform, smooth and dense

as-deposited layers with a thickness of ca. 300 nm. The chemical composition of those ZnO layers films was verified by XPS and EDX analyses. The analysis of the electrochemical behaviour was made arduous by the mechanical instability of the layers characterized by large cracks and local delamination. The film rupturing was found to be potential-dependent (occurring mainly at potential more negative than ca. -0.6 V) and might be related to the piezoelectric properties of columnar ZnO.

Oxygen reduction polarization curves were recorded in alkaline electrolyte at pH 10 under controlled hydrodynamic conditions. Despite the relatively fast degradation of the layers, important features of ORR could be identified. Notably it was found that textured ZnO has a poor activity towards ORR (when compared to that of the copper substrates).

Furthermore, it was evidenced that a non-negligible amount of hydrogen peroxide is generated indicating that both the direct and indirect reaction pathway are followed. These results are in line with previous reports on “thick” ZnO deposits and stand in contrast with those obtained with ultrathin (nanometric) passive ZnO layers that promote indirect oxygen reduction and hydrogen peroxide generation. A more quantitative analysis of the RRDE results was not possible since, during cathodic polarization, the layers ruptured while the ORR kinetics was mostly under charge transfer control.

In the next chapter, electrochemical impedance spectroscopy is used to characterize the ZnO textured layers and analyse more finely the onset of their degradation as function of potential.

### 3.5. References

- [1] X. Ge, A. Sumboja, D. Wu, T. An, B. Li, F.W.T. Goh, T.S.A. Hor, Y. Zong, Z. Liu, Oxygen reduction in alkaline media: from mechanisms to recent advances in catalysts, *ACS Catalysis* 5 (2015) 4643;
- [2] K. Kinoshita, *Electrochemical oxygen technology*, Chapter 1, John Wiley, New York, 1992, 4;
- [3] W. Xing, G. Yin, J. Zhang, *Rotating electrode methods and oxygen reduction electrocatalysts*, Chapter 4 – Electrochemical Oxygen Reduction Reaction, Elsevier, 2014 133–170;
- [4] H. S. Wroblowa, S. B. Qaderi, The mechanism of oxygen reduction on zinc, *Journal of Electroanalytical Chemistry and Interfacial Electrochemistry*, 295 (1990) 153-161;
- [5] Y. Li, D. Zhang, J. Wu, Study on kinetics of cathodic reduction of dissolved oxygen in 3.5% sodium chloride solution, *Journal of Ocean University of China* 9 (2010) 239;

- [6] N. Heller-Ling, M. Prestat, J. L. Gautier, J. F. Koenig, G. Poillerat, P. Chartier, Oxygen electroreduction mechanism at thin  $\text{Ni}_x\text{Co}_{3-x}\text{O}_4$  spinel films in a double channel electrode flow cell (DCEFC), *Electrochimica Acta* 42 (1997) 197-202;
- [7] R. G. Compton, G. M. Stearn, P. R. Unwin, A. J. Barwise, Double channel electrodes and the measurement of heterogenous reaction rates at the solid-liquid interface, *Journal of Applied Electrochemistry* 18 (1988) 657-655;
- [8] N. Heller-Ling, G. Poillerat, J. F. Koenig, J. L. Gautier, P. Chartier, Double channel electrode flow cell (DCEFC): application to the electrocatalysis of the oxygen reduction on oxide films, *Electrochimica Acta* 39 (1994) 1669;
- [9] I. S. Cole, Recent Progress and Required Developments in Atmospheric Corrosion of Galvanised Steel and Zinc, *Materials* 10 (2017) 1288;
- [10] H. Dafydd, D. A. Worsley, H. N. McMurray, The kinetics and mechanism of cathodic oxygen reduction on zinc and zinc–aluminium alloy galvanized coatings, *Corrosion Science* 47 (2005) 3006-3018;
- [11] H. J. Flitt, D. P. Schweinsberg, Synthesis, matching and deconstruction of polarization curves for the active corrosion of zinc in aerated near-neutral NaCl solutions, *Corrosion Science* 52 (2010) 1905–1914;
- [12] A. Goux, T. Pauporte, D. Lincot, Oxygen reduction reaction on electrodeposited zinc oxide electrodes in KCl solution at 70°C, *Electrochimica Acta*, 51 (2006) 3168–3172;
- [13] M. Prestat, F. Vucko, B. Lescop, S. Rioual, F. Peltier, D. Thierry, Oxygen reduction at electrodeposited ZnO layers in alkaline solution, *Electrochimica Acta* 218 (2016) 228-236;
- [14] W. K. Burton, N. Carberra, F. C. Frank, The growth of crystals and the equilibrium structure of their surfaces, *Philosophical Transactions of the Royal Society of London A* 243 (1951) 299;
- [15] S.Y. Chu, W. Water, J.T. Liaw, Influence of postdeposition annealing on the properties of ZnO films prepared by RF magnetron sputtering, *Journal of the European Ceramic Society* 23 (2003) 1593–1598;
- [16] S. S. Lin, J. L. Huang, Effect of thickness on the structural and optical properties of ZnO films by r.f. magnetron sputtering, *Surface & Coatings Technology* 185 (2004) 222– 227;
- [17] J. Hüpkes, J. I. Owen, S. E. Pust, E. Bunte, Chemical etching of zinc oxide for thin-film silicon solar cells, *ChemPhysChem* 13 (2012) 66-73;
- [18] J. Han, W. Qiu, W. Gao, Potential dissolution and photo-dissolution of ZnO thin films, *Journal of hazardous materials* 178 (2010) 115-122;

- [19] Z. Onuk, N. Rujisamphan, R. Murray, M. Bah, M. Tomakin, S. I. Shah, Controllable growth and characterization of highly aligned ZnO nanocolumnar thin films, *Applied Surface Science* 396 (2017) 1458-1465;
- [20] K. B. Sundaram, A. Khan, Characterization and optimization of zinc oxide films by r.f. magnetron sputtering, *Thin Solid Films* 295 (1997) 87-91;
- [21] D. L. Cheng, K. S. Kao, C. H. Liang, Y. C. Wang, Y. C. Chen, W. C. Shih, L. P. Chan, Piezoelectric Response Evaluation of ZnO Thin Film Prepared by RF Magnetron Sputtering, *MATEC Web of Conferences* 109 (2017) 04001;
- [22] Y. H. Hsu, J. Lin, W. C. Tang, RF sputtered piezoelectric zinc oxide thin film for transducer applications. *Journal of Materials Science: Materials in Electronics* 19 (2008) 653-661;
- [23] S. Kunj, K. Sreenivas, Residual stress and defect content in magnetron sputtered ZnO films grown on unheated glass substrates, *Current Applied Physics* 16 (2016) 748-756;
- [24] K. Zhang, J. Qi, Y. Tian, S. Lu, Q. Liang, Y. Zhang, Influence of piezoelectric effect on dissolving behavior and stability of ZnO micro/nanowires in solution, *RSC Advances* 5 (2015) 3365-3369;
- [25] A. J. Bard, L. R. Faulkner, *Electrochemical Methods: Fundamentals and Applications*, 2nd Edition, Chapter 9, Wiley, 2001;
- [26] N. H. Al-Hardan, M. J. Abdullah, A. A. Aziz, H. Ahmad, M. Rashid, The effect of oxygen ratio on the crystallography and optical emission properties of reactive RF sputtered ZnO films, *Physica B: Condensed Matter* B 405 (2010) 1081-1085;
- [27] J. P. Becker, S. E. Pust, J. Hupkes, Effects of the electrolyte species on the electrochemical dissolution of polycrystalline ZnO:Al thin films, *Electrochimica Acta* 112 (2013) 976-982;
- [28] A. Goux, T. Pauporté, J. Chivot, D. Lincot, Temperature effects on ZnO electrodeposition, *Electrochimica Acta* 50 (2005) 2239-2248.

## Annex I – Additional information Chapter 3

In this Annex the first procedures are presented to obtain the best conditions to produce dense well-oriented ZnO films (named as “textured” ZnO). Many parameters were modified, among them: the influence of the argon flux, the deposition power and the thickness. All these first steps were necessary for the production of these ZnO films.

### I. Synthesis of the ZnO layers

The first procedure was to obtain the best conditions to produce textured ZnO dense films. To obtain these results, we focused on the intensity of the (002) peak [1-6] to evaluate the different conditions. Figure I show the influence of the argon flux (Figure Ia) and the influence of the deposition power.

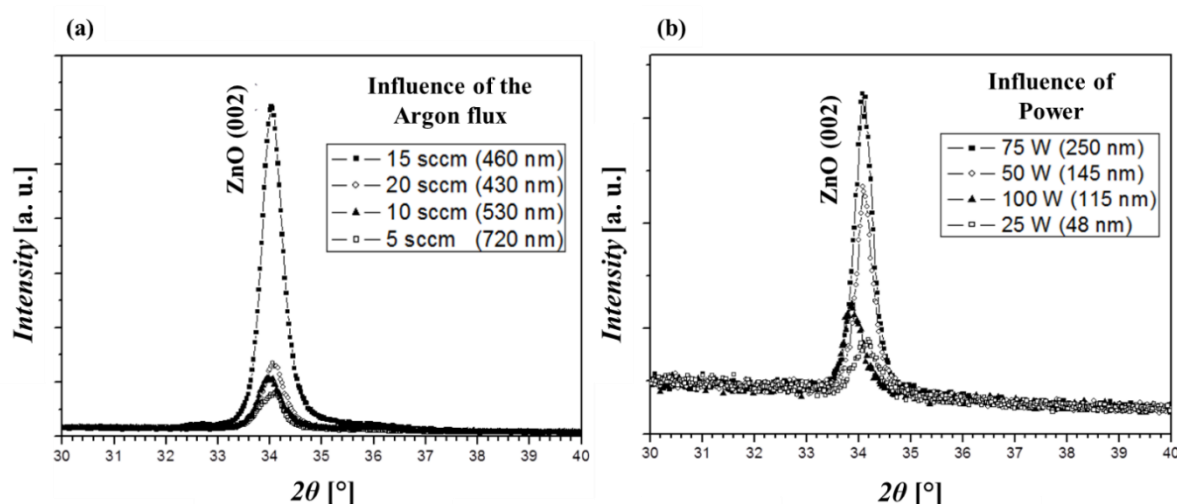


Figure I: XRD spectrums of ZnO thin films deposited on glass substrates showing the influence of the argon flux (a) and power (b). Note the linear-scale of the y-axis.

According to XRD spectrums, the biggest intensity of (002) peak was obtained for 15 sccm argon flux (Figure Ia) resulting in an oriented film with a thickness of 460 nm. The best deposition power observed was 75W, where an oriented film with a thickness of 250 nm was obtained (Figure Ib). With these preliminary studies, the argon flux and the power were defined.

The next step was to obtain different thicknesses (according to the deposition time), for which, in Figure II are shown the results of three different thickness.

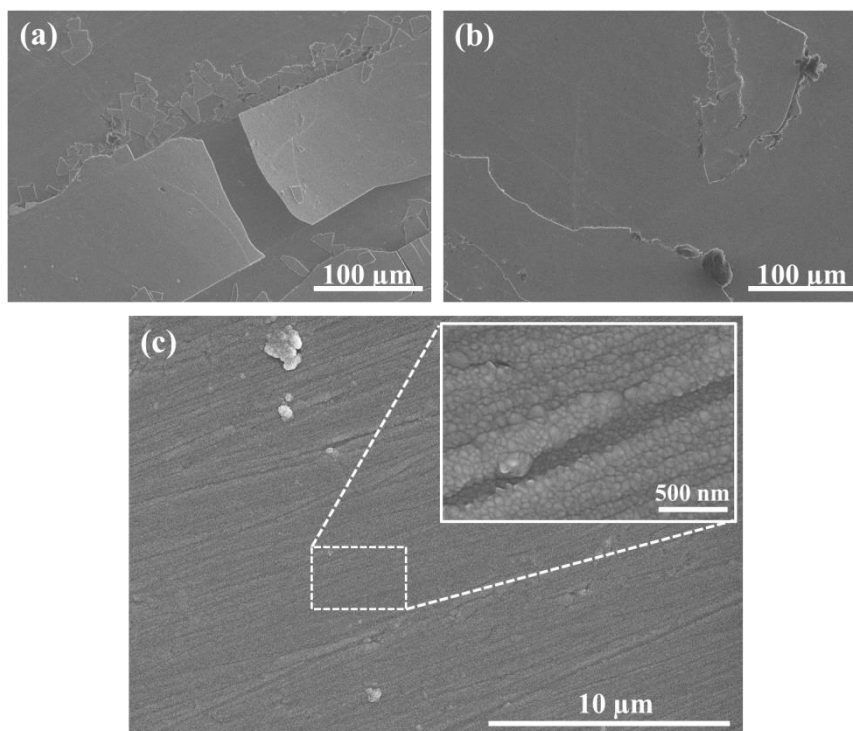


Figure II: SEM images of ZnO thin films deposited on copper substrates with different thickness (a) 1  $\mu\text{m}$ , (b) 700 nm and (c) 300 nm.

With these top-view SEM images, it is possible to note that with larger deposition times, higher thicknesses are obtained. These thicker films (thickness of 1  $\mu\text{m}$  and 700 nm) presented cracks since the beginning, being impossible to use them as a model electrode. The most promising thickness was the 300 nm, which showed no cracks, corresponding to a deposition time of 90 minutes.

All the conditions to produce the textured ZnO films are then: ZnO target; deposition time (90 min); mixture of reactive gas (Argon: O<sub>2</sub>) 2:1 (it means (argon flux (15 sccm) and oxygen flux (10 sccm)), and the input power (at the target) 75W.

## II. Investigation of the dissolution process

Assuming the hypothesis that textured ZnO films undergo chemical dissolution in alkaline media, a study was developed to try to explain this assumption. The dissolution was verified in alkaline electrolyte (same solution used for the electrochemical measurements). The films were exposed for 24 hours and 1 week. The samples were analyzed by SEM and EDX technique, as shown in Figure III.

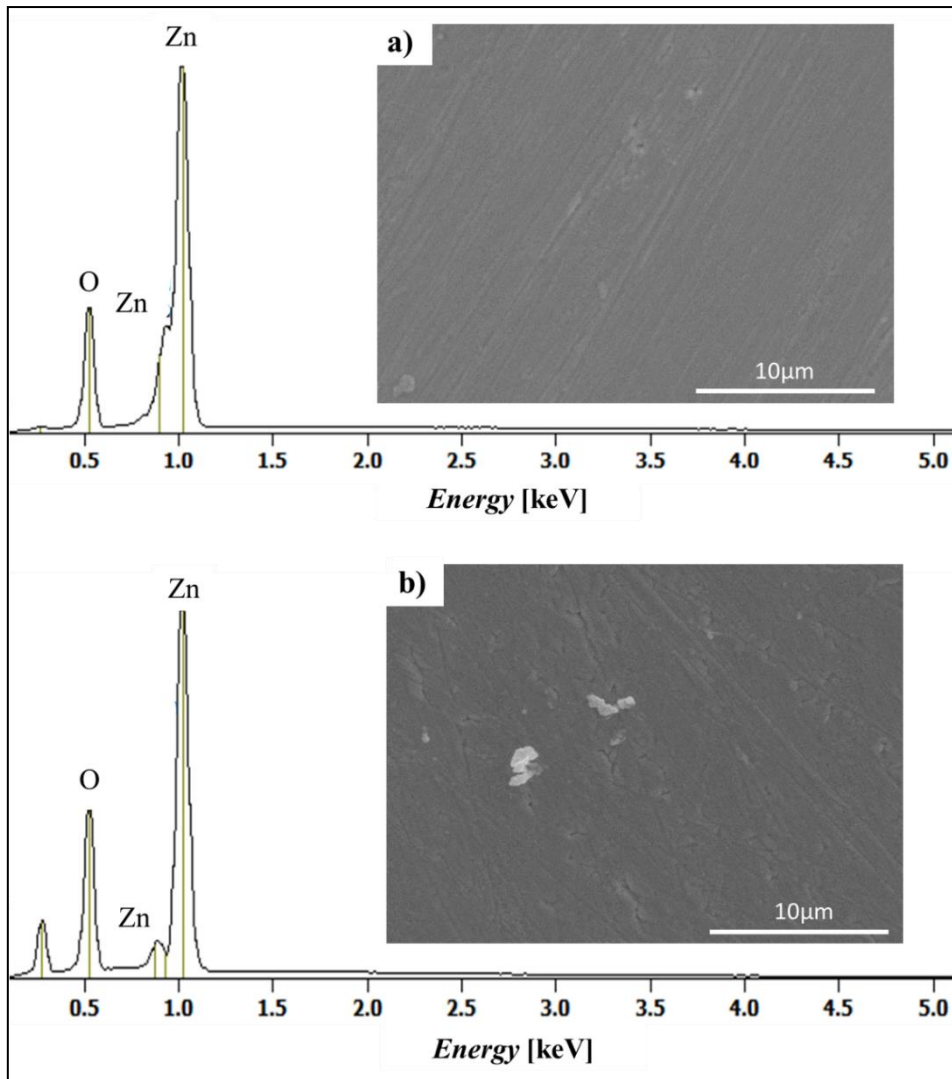


Figure III: SEM images and EDX spectrums of (a) 24h and (b) 1week immersion on the electrolyte.

Practically, was not observed any changes on the ZnO surface after 24 h and 1 week of immersion on the alkaline electrolyte. The qualitative and quantitative results provided by the EDX technique display that only ZnO is present on the surface. The dissolution hypothesis cannot be totally excluded, since some authors observed the dissolution of ZnO thin films in alkaline medium, but the electrolyte concentration should be considered [7].

### III. References:

- [1] H. F. Liu et al. Effects of substrate on the structure and orientation of ZnO thin film grown by rf-magnetron sputtering. *Journal of Applied Physics*, 102 (2007);
- [2] R. Ondor-Ndong et. al. Properties of RF magnetron sputtered zinc oxide thin films. *Journal of Crystal Growth*, 255 (2003) 130-135;



- [3] I.-S. Kim et al. Magnetron sputtering growth and characterization of high-quality single crystal ZnO thin films on sapphire substrates. *Semiconductors Science and Technology*, 19 (2004) 29-31;
- [4] S.-S. Lin, J.-L. Huang. Effect of thickness on the structural and optical properties of ZnO films by rf. magnetron sputtering. *Surface & Coatings Technology* 185 (2004) 222-227;
- [5] Z. Onuk, N. Rujisamphan, R. Murray, M. Bah, M. Tomakin, S. I. Shah, Controllable growth and characterization of highly aligned ZnO nanocolumnar thin films, *Applied Surface Science* 396 (2017) 1458-1465;
- [6] K. B. Sundaram, A. Khan, Characterization and optimization of zinc oxide films by rf. magnetron sputtering, *Thin Solid Films* 295 (1997) 87-91;
- [7] J. P. Becker, S. E. Pust, J. Hupkes, Effects of the electrolyte species on the electrochemical dissolution of polycrystalline ZnO:Al thin films, *Electrochimica Acta* 112 (2013) 976-982;

## Impedance analysis of the degradation of textured ZnO films

---

### Abstract

The degradation of (002)-oriented sputtered ZnO layers under DC polarization was studied by electrochemical impedance spectroscopy and electron microscopy. It was found that the structure of the as-deposited ZnO film was dense at the nanoscale. An equivalent circuit model including the De Levie impedance accounted for the localized propagation of microscaled cracks towards the copper substrates. This generated a capacitance ( $C_{ZnO}$ ) that represents the crack surface area in contact with the electrolyte.  $C_{ZnO}$  was small enough not to be obscured by the double layer capacitance at the top of the layer and increased with increasingly negative potential. The combination of *in situ* EIS analysis with the *ex situ* structural information provided by electron microscopy proved to be an efficient methodology to evidence the first stages of degradation of the textured ZnO films.

*A modified version of this chapter will be submitted to ChemElectroChem or Electrochimica Acta: Impedance spectroscopy analysis of the degradation of textured ZnO films under DC polarization (provisional title). J. Soares Costa, M. Prestat, B. Tribollet, B. Lescop, S. Rioual, L. Holzer, D. Thierry.*

### 4.1. Introduction

In the previous Chapter, the DC behavior of dense (002)-oriented ZnO films has been studied. The films presented a potential-dependent mechanical instability leading to film cracking and delamination which rendered ORR investigations difficult. When using potentiodynamic polarization curves, the critical potential at which the film ruptured was around ca. -0.6V vs. Hg-HgO. The criterions for estimating this rupture potential was the presence of cracks in post-mortem SEM analysis and the increase of ORR activity (when the electrolyte reached the underlying and more electrochemically active copper substrate). Hence conclusions could be drawn only when significant damages on the films had already occurred.

This chapter focuses on the early stage of degradation taking place at potentials less negative than -0.6 V and induced by the crack propagation. The ZnO layer with the propagating cracks

might be considered as “porous” systems to a certain extent. Electrochemical impedance spectroscopy (EIS) has already been used in the literature to investigate such porous layers.

Recently Barrès *et al.* used EIS to investigate the porosity of silicon nitride ( $\text{SiN}_x$ ) thin films (30-60 nm) used in the glass industry as barrier layers [1]. High-resolution electron microscopy analysis revealed the presence of nanoscale pores (0.5 - 2 nm). The study distinguished “through-pores” in which the electrolyte could reach an underlying gold substrate and “non-through-pores” that crossed only a portion of  $\text{SiN}_x$  layer. The impedance of the former was modelled as a pore resistance in series with a CPE while the distribution of resistivity of the latter was accounted for with the Young model [2,3]. Interestingly, the approach followed by Barrès *et al.* based on combination *in situ* impedance spectroscopy with *ex situ* electron microscopy analysis present similarities with the approach used in the present chapter.

De Levie model has been developed for ideal “metallic” electrodes with parallel cylindrical pores with identical geometry to account for frequency dispersion using transmission lines [4]. Several studies showed that De Levie impedance could be used to describe analytically more complex systems with pores of various geometry, length and radius [5-8]. For instance, Barcia *et al.* investigated cast iron corrosion in Evian mineral water using the De Levie impedance [5]. The latter was applied to the cathodic impedance through macroporous red rust. The (averaged) number and length of pores could be estimated after numerical optimization between experimental and simulated impedance data.

The objective of this chapter is to gain more understanding about the degradation of the textured ZnO layers (described previously in Chapter 3) in alkaline electrolyte using EIS. The experimental data are compared with two models, one accounting for a fully dense ZnO layer and the other describing the penetration of the electrolyte in the cracks of the films. The global *in situ* information provided by EIS is completed by the local *ex situ* structural data at the nanoscale and at the microscale obtained by electron microscopy.

## 4.2. Experimental Section

### 4.2.1. Synthesis and characterization of the ZnO layers

This study deals with the same 300 nm thin textured ZnO layers as those produced in Chapter 3. Hence the details of the sample preparation as well as the results of XPS, XRD, EDX, FIB-SEM and AFM characterization are not repeated here. Additional high-angle annular dark-field scanning transmission electron microscopy (HAADF-STEM) imaging and resistivity measurements in air were performed. HAADF-STEM was used to characterize the

level of compacity of the as-deposited layer at the nanoscale. For this purpose, TEM-lamellas representing cross-sections of the ZnO-layers were prepared with the focused ion beam (FIB) technique. The ZnO layers were then investigated with an analytical TEM (FEI Talos F200X) at 200 kV. Top-view imaging was performed by conventional scanning electron microscopy (SEM, SU3500, Hitachi) to evaluate the aspect of surface of the layers at the microscale.

The electrical resistivity of the layers was measured in air (dry conditions) using the two-probe method in transverse mode with a multimeter (ISO-TECH IDM62T) (Figure 4.1). The transverse mode means that the electrical charges circulate along the main axis of the ZnO column perpendicular to the substrate, as they do during the electrochemical experiments (wet conditions). For that purpose, as shown in the sketch of Figure 4.1, a copper contact electrode (surface area 1 mm<sup>2</sup>) was deposited by rf-sputtering technique on the top of ZnO layer. The same ZnO thickness as for the EIS measurements, i.e. 300 nm, was used.

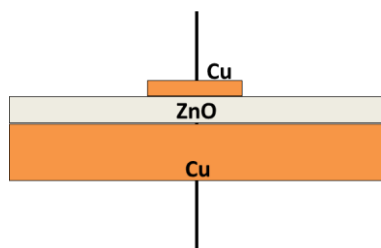


Figure 4.1: Two-probe setup for the electrical resistance measurement of the ZnO layer in the transverse mode in air.

### 4.2.2. Electrochemical measurements

The electrochemical experiments were conducted at room temperature in KOH solutions at pH = 10 +/- 0.1 with KCl 0.2 M as supporting electrolyte. EIS measurements were carried out under controlled hydrodynamic conditions using the RDE technique (Pine Research Instrumentation, Durham, NC, USA) at a rotation rate of 1000 rpm. The counter-electrode was a large titanium-based metallic grid placed below the working electrode. The reference electrode was a mercury/mercury oxide electrode (Hg-HgO, KOH 1M). The three-electrode setup was controlled by a Gamry Reference 600 potentiostat. The applied frequency domain ranged from 10<sup>5</sup> Hz to 1 Hz with 10 points per decade. The sinusoidal perturbation was 10 mV. Data fitting was carried out using non-commercial software developed at the Laboratoire Interfaces et Systèmes Electrochimiques (LISE), Paris, France, based on a simplex strategy [1,9]. The program minimizes the function  $\chi^2$ :

$$\chi^2 = \sum_{i=1}^{nf} \left[ \left( \frac{\text{Re}(Z_{exp,i}) - \text{Re}(Z_{sim,i})}{0.005|Z_{exp}|} \right)^2 + \left( \frac{\text{Im}(Z_{exp,i}) - \text{Im}(Z_{sim,i})}{0.005|Z_{exp}|} \right)^2 \right] \quad (1)$$

with  $nf$  being the number of frequencies in the experimental spectra,  $Z_{exp}$  and  $Z_{sim}$  the experimental and simulated (calculated) impedance, respectively, and 0.005 the coefficient standing for an acceptable error of 0.5% between the experimental and the simulated spectra.

### 4.3. Results and discussion

#### 4.3.1 Physical characterization of the ZnO layers

Preliminary remark about units: please note that, in this study, resistance, impedance and capacitance values are expressed relative to the geometrical surface area of the disk electrode. Hence, unless otherwise stated, resistances (and impedances) are expressed in  $\Omega \text{ cm}^2$  and capacitances in  $\mu\text{F}/\text{cm}^2$ . Only the resistance,  $R$ , of the film measured in air with the set-up of Figure 4.1 is expressed in  $\Omega$  (see below).

Electron microscopy analysis provides relevant *ex situ* microstructural information on the ZnO layers at the microscale and the nanoscale. Analysis of HAADF-STEM images allows determining porosity (that appears in black contrast) [1,10,11]. ZnO is evidenced to have a very compact structure at the nanoscale (Figure 4.2a). Only very thin vertical black lines between the columns were detected. They could be grain boundary or extremely narrow pores that are very unlikely to let the electrolyte go through in view of their aspect ratio. Figure 4.2b shows the surface of the ZnO films using conventional SEM. One can notice the presence of a limited number of micro-scaled defects in the otherwise dense microstructure.

The micro/nano-structural features and their impact on the electrical properties of the layers obtained by EIS are further discussed below along with Figure 4.10.

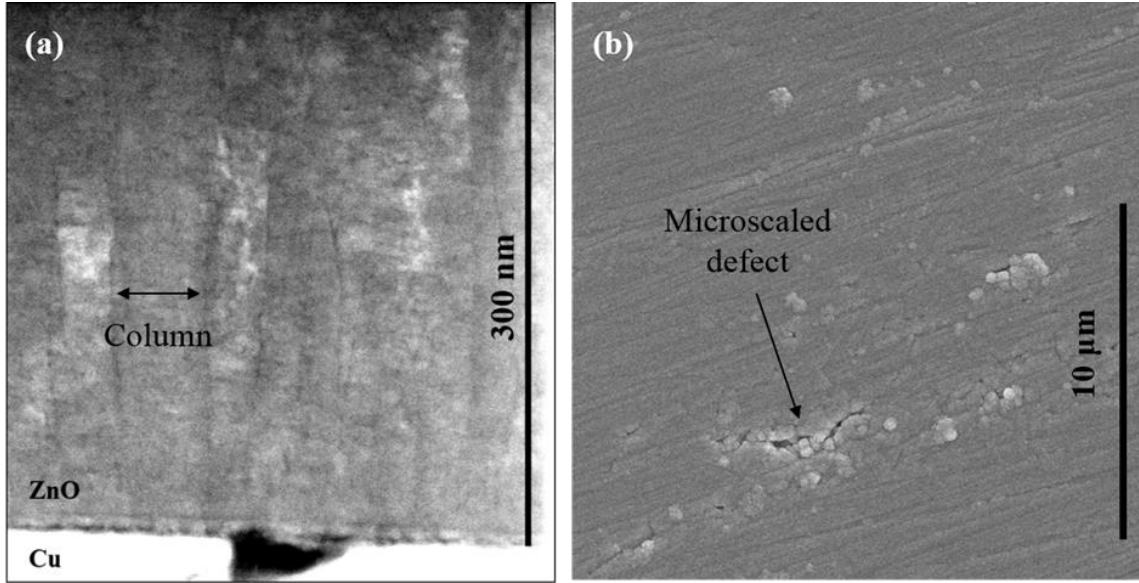


Figure 4.2: Electron microscopy analysis of the as-deposited ZnO layers: (a) cross-sectional HAADF-STEM image (nanoscale information) and (b) top-view SEM micrograph of the surface (microscale information).

The resistance,  $R$ , of the film was measured in transverse mode (cross-plane) in air between two copper stripe electrodes (Figure 4.1).  $R$  was found to be ca 0.3 - 0.4  $\Omega$ . The order of magnitude of the resistivity,  $\rho$ , can be deduced using Eq. (2):

$$\rho = \frac{RS}{L} \quad (2)$$

with  $S$  being the ZnO surface area between the two copper electrodes (1 mm<sup>2</sup>) and  $L$  the thickness of the layer (300 nm, the same as in the electrochemical measurements).  $\rho$  was therefore estimated to be ca. 10<sup>2</sup>  $\Omega$  cm. This low resistivity value suggests that the impedance of the ZnO layers cannot be described by models accounting for distribution of resistivity within the films (such as the power law model [3] or Young model [2]). In the rest of this chapter, the product  $\rho L$  ( $\sim 3 \cdot 10^{-3}$   $\Omega$  cm<sup>2</sup>) is renamed  $R_{film}$  and implemented in the equivalent circuit models depicted in Figure 4.4 and Figure 4.6.

### 4.3.2. Electrochemical results

Figure 4.3 shows the experimental impedance recorded at -0.4 V (the open circuit potential, OCP, was ca. -0.1 V). In this study, electrochemical experiments were carried out at negative overpotentials “far” from OCP so that the faradaic impedance could be simplified to its sole cathodic contribution.

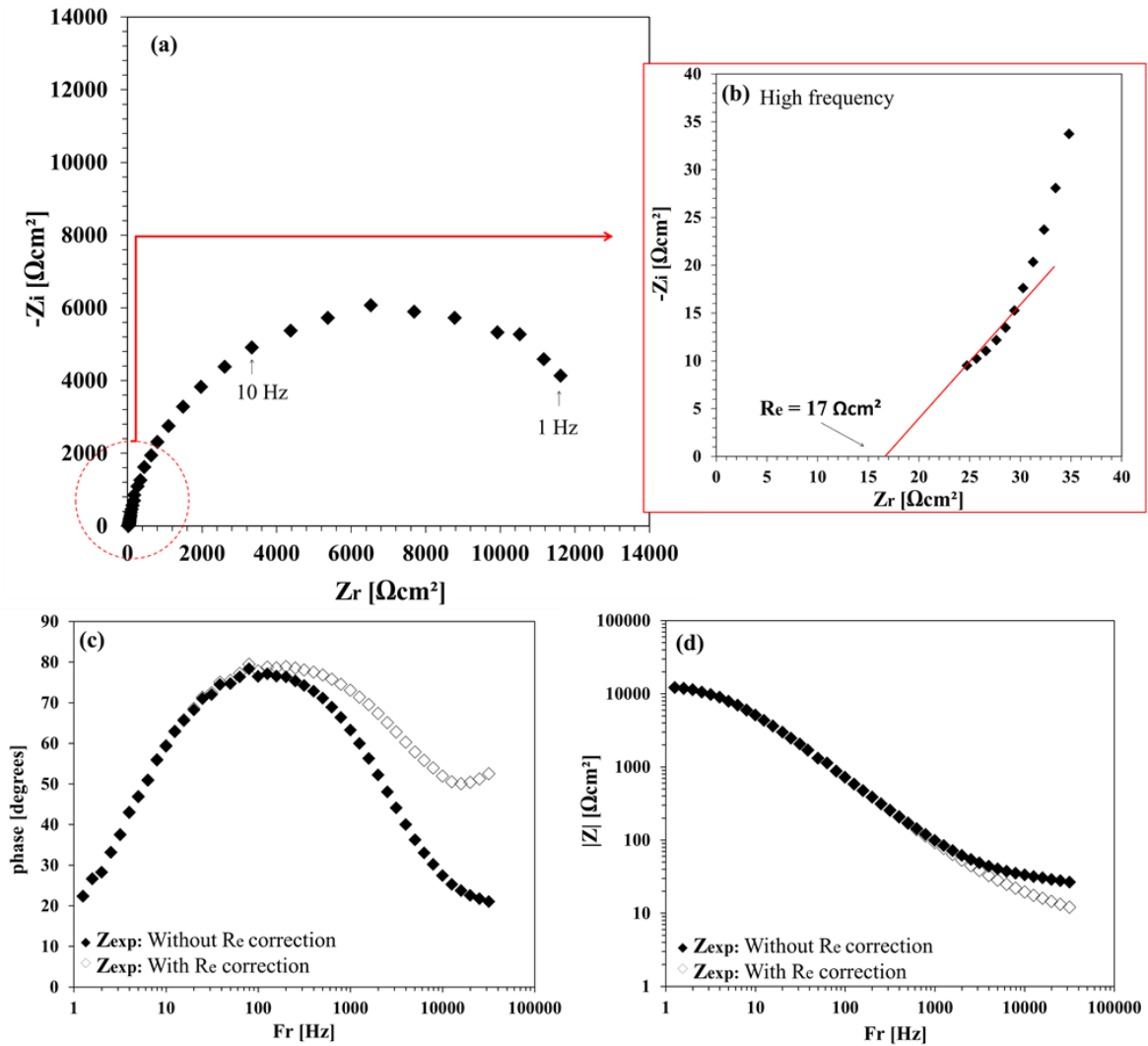


Figure 4.3: EIS diagrams recorded at -0.4V. (a) Nyquist plot with (b) zoom in high frequency to determine the electrolyte resistance ( $R_e$ ). Bode plots (without and with  $R_e$  correction): (c) phase curve and (d) modulus curve.

It has been demonstrated in the literature that, in the “classical” Bode plots (as recorded, without correction), the high frequency data might be obscured by the electrolyte resistance which can be misleading for data interpretation [9,12,13]. In the present study, the  $R_e$  value was obtained by graphical extrapolation of the Nyquist plot onto the real axis at high frequencies (Figure 4.3a and Figure 4.3b). The effect of the  $R_e$  correction on the Bode plots is demonstrated in Figure 4.3c and Figure 4.3d.

As shown in Figure 4.4, a first simple model was tested by assuming that the ZnO layer was compact and that the microscale defects observed on the top-view SEM micrographs (Figure 4.2b) did not impact the impedance behavior. Hence in this model, the contribution of the ZnO film is solely the electronic resistance  $R_{\text{film}}$  whose low value was assessed above.

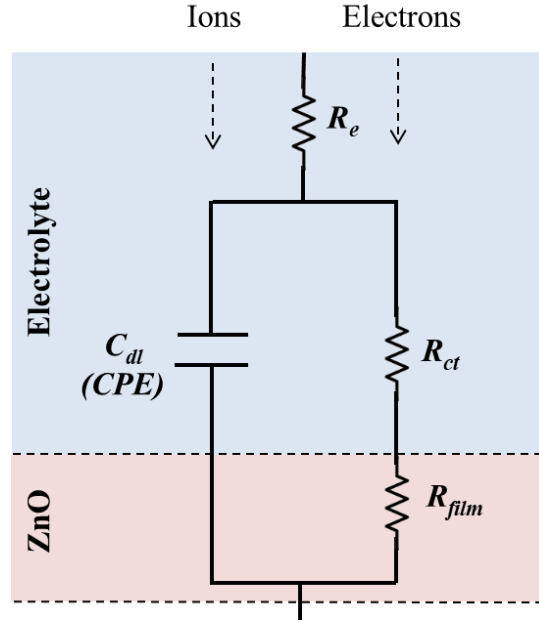


Figure 4.4: First equivalent circuit model accounting for a dense ZnO layer with no penetration of the electrolyte.

The rest of model consists of a faradaic impedance,  $Z_f$ , that is simplified to a charge transfer resistance,  $R_{ct}$ , in parallel with the ZnO/electrolyte double layer capacitance that is represented by a constant phase element,  $Z_{CPE}$  [14,15]. The elements of this model can be written:

$$Z_f = R_{ct} \quad (3)$$

$$Z_{CPE} = \frac{1}{Q(j\omega)^\alpha} \quad (4)$$

with  $\omega$  being the angular frequency, and  $Q$  and  $\alpha$  the frequency-independent CPE parameters. The electrolyte resistance  $R_e$  completes the equivalent circuit model.  $R_{film}$  is assumed to be much smaller than  $R_{ct}$  and is therefore neglected. The total simulated impedance,  $Z_{sim}$ , for this model is:

$$Z_{sim} = \frac{1}{\frac{1}{R_{ct}} + \frac{1}{Z_{CPE}}} + R_e \quad (5)$$

The fitting process enables to get the value of  $Q$ . Then the double layer capacitance is obtained by applying the Brug formula [16]:



$$C_{dl} = Q^{1/\alpha} R_e^{(1-\alpha)/\alpha} \quad (6)$$

A comparison between the experimental data and the simulated impedance obtained from the fitted values corresponding to the 1<sup>st</sup> model (Figure 4.4) is given in Figure 4.5. The results of the fitting process are presented in Table 4.1.

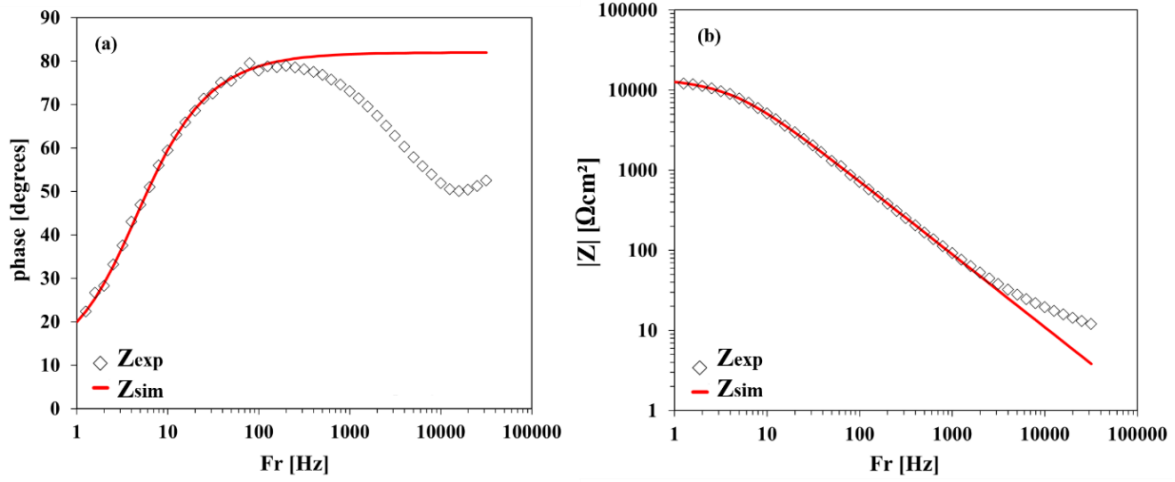


Figure 4.5: Corrected Bode phase (a) and modulus (b) diagrams obtained at -0.4V. The open symbols represent the experimental data ( $Z_{exp}$ ). The line represented the simulated data ( $Z_{sim}$ ) obtained from the fitting process using the first equivalent circuit model (Figure 4.4).

$R_{ct}$ ( $\Omega \text{ cm}^2$ )	$Q$	$\alpha$	$C_{dl}$ ( $\mu\text{F cm}^2$ )
$1.4 \cdot 10^4$	$4.4 \cdot 10^{-6}$	0.89	1.4

Table 4.1: Result of the fitting process using the first equivalent circuit model (Figure 4.4) and the Re-corrected impedance recorded at -0.4 V (Figure 4.5).

The model works well at low frequencies (below 38 Hz) only.  $C_{dl}$  is found to be 1.4  $\mu\text{F cm}^{-2}$ , which is very small compared to the typical double layer capacitance values (around 10-100  $\mu\text{F cm}^{-2}$ ). Similarly, low values were obtained for all applied potentials between -0.3 V and -0.5 V. Furthermore, at high frequencies, the first model does not account for the decrease of the phase (Figure 4.5a) and the change of slope of the modulus curve (Figure 4.5b). Based on those results, a second model was developed by introducing a second capacitive element in series with  $C_{dl}$ . This model accounts for the penetration of the electrolyte into the ZnO during the degradation of the layers under DC polarization. Compared to the first model (Figure 4.4), De Levie impedance was added in the equivalent circuit, as shown in Figure 4.6. As mentioned in the introduction, De Levie model was shown to be able to describe, at a phenomenological level, the impedance of pores with very

different geometries far from the ideal system of identical cylindrical pores. In the present study, the cracks growing and propagating through the layers are considered as “pores” accessible by the electrolyte.

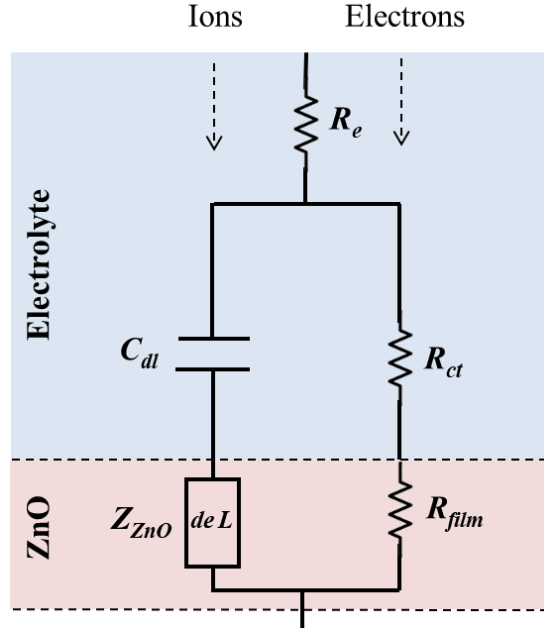


Figure 4.6: Second equivalent circuit model accounting for the penetration of the electrolyte into the ZnO layer using a de Levie impedance. In the fitting process,  $C_{dl}$  is considered as large (compared to the capacitance of the ZnO layer) and its impedance is therefore neglected.

The second model can be analytically described using Eqs. (3), (7), (8), (9) and (10). Where the impedance of the ZnO layer,  $Z_{ZnO}$ , is represented by DeLevie impedance:

$$Z_{ZnO} = \frac{\sqrt{R_0 Z_0}}{n} \coth \sqrt{\frac{R_1}{Z_0}} \quad (7)$$

with  $R_0$  being the electrolyte resistance per unit of pore length with units of  $\Omega \text{ cm}^{-1}$ .  $n$  is the number of pores per  $\text{cm}^2$ .  $R_1$  is the product  $l^2 R_0$ , where  $l$  is the length of the cylindrical pore of the “ideal” electrode of De Levie [4]. In the present model, that does not aim at evaluating precisely the pores (cracks) geometry, only  $R_1$  is used as a fitting parameter.  $Z_0$  is the interfacial impedance per unit length of pore (expressed in  $\Omega \text{ cm}$ ). Here, one assumes no charge transfer reaction in the pores and,  $Z_0$  is simply described by a CPE corresponding to the double layer capacitance along the pore wall whose parameters are  $Q_{pore}$  and  $\beta$ .

$$Z_0 = \frac{1}{Q_{pore}(j\omega)^\beta} \quad (8)$$

When the argument of the *coth* is small, the *coth* is equal to the inverse of the argument (observed in low frequency) and can be represented as:

$$Z_{ZnO} = \sqrt{\frac{R_0}{R_1}} \frac{Z_0}{n} \quad (9)$$

The faradaic impedance,  $Z_f$ , is expressed the same way as in the first model using Eq. (3). The double layer capacitance shown in Figure 4.6 physically exists, but its impedance is small compared to that of  $Z_{ZnO}$ . Hence it is neglected in this mathematical model (and in the corresponding fitting process). The total simulated impedance,  $Z_{sim}$ , for this model is thus:

$$Z_{sim} = \frac{1}{\frac{1}{R_{ct}} + \frac{1}{Z_{ZnO}}} + R_e \quad (10)$$

From the fitting process, the parameter  $Q_{ZnO}$  is calculated using the values of  $Q_{pore}$ ,  $R_1$  and  $R_0$ :

$$Q_{ZnO} = Q_{pore} \sqrt{\frac{R_1}{R_0}} n \quad (11)$$

Finally, the capacitance,  $C_{ZnO}$ , of the ZnO film is derived from the Brug formula:

$$C_{ZnO} = Q_{ZnO}^{1/\beta} R_e^{(1-\beta)/\beta} \quad (12)$$

Figure 4.7a shows the results of the fitting of the experimental data with the second equivalent circuit model. The resulting fitting parameters are listed in Table 4.2.

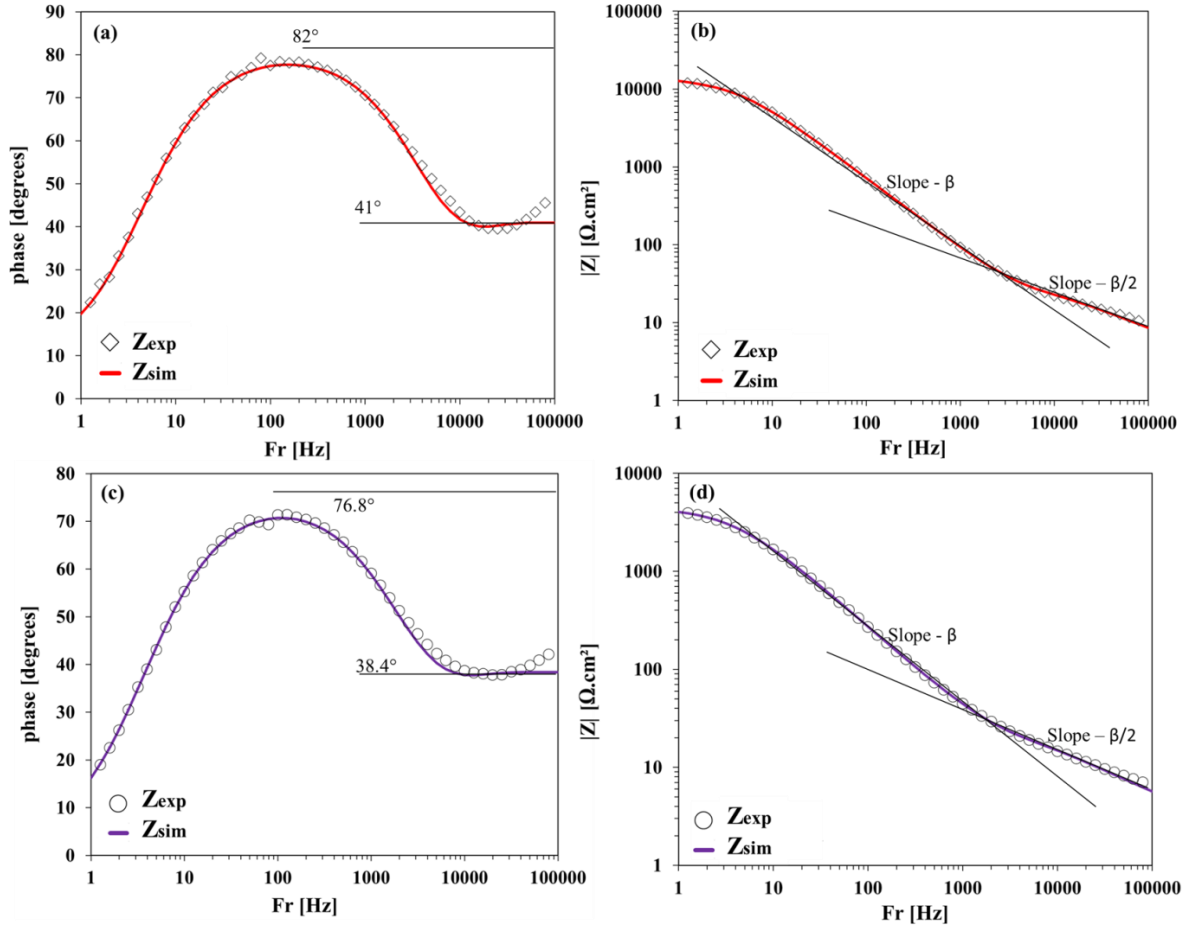


Figure 4.7: Corrected Bode phase (a) and modulus (b) diagrams obtained at -0.4 V and corrected Bode phase (c) and modulus (d) diagrams obtained at -0.5 V. The open symbols represent the experimental data ( $Z_{exp}$ ). The line represented the simulated data ( $Z_{sim}$ ) obtained from the fitting process using the second equivalent circuit model (Figure 4.6).

The phase  $82^\circ$  (at -0.4V) and  $76.8^\circ$  (at -0.5V) is corresponding to the limiting phase of the CPE and is equal to  $\beta \times 90^\circ$ .  $41^\circ$  (at -0.4V) and  $38.4^\circ$  (at -0.5V) corresponds to the limiting phase in the high frequency range and are equal to the half value of the limiting phase of CPE in agreement with the square root in the De Levie model.

$E$ (V)	$R_e$ ( $\Omega \text{ cm}^2$ )	$R_{ct}$ ( $\Omega \text{ cm}^2$ )	$R_0/n^2$ ( $\Omega \text{ cm}^3$ )	$R_l$ ( $\Omega \text{ cm}$ )	$Q_{pore}$ $\Omega^{-1} \text{ cm}^{-1} \text{ s}^\beta$	$\beta$	$Q_{ZnO}$ $\Omega^{-1} \text{ cm}^{-2} \text{ s}^\beta$	$C_{ZnO}$ ( $\mu\text{F cm}^{-2}$ )
-0.4	13.2	$1.4 \cdot 10^4$	0.21	$1.3 \cdot 10^4$	$1.7 \cdot 10^{-8}$	0.90	$3.9 \cdot 10^{-6}$	1.46
-0.5	13.8	$4.5 \cdot 10^3$	0.23	$8.3 \cdot 10^3$	$7.7 \cdot 10^{-8}$	0.85	$1.46 \cdot 10^{-5}$	3.3

Table 4.2: Results of the fitting process using the second model (Figure 4.6 and Figure 4.7).

In high frequency the argument of coth is large and the coth is equal to one. Then,

$$Z_{ZnO} = \frac{\sqrt{R_0 Z_0}}{n} \quad (13)$$

and the phase is the half of the  $Z_0$  phase and the slope of modulus of  $Z$  is the half of the slope of the modulus of  $Z$  in the low frequency ( $-\beta/2$ ) (Figure 4.7).

An excellent agreement was found between experimental and simulated data in the whole frequency range. This finding shows that the De Levie impedance can describe in a satisfactory way the capacitive behavior of the growing cracks even though they are not of cylindrical shape. The second model was also successfully applied at different potentials in the cathodic direction from -0.3 V till -0.5 V. The resulting  $C_{ZnO}$  and  $R_{ct}$  values are reported in Figure 4.8. Post-mortem SEM analysis of the surface of the layers polarized at -0.4 V and -0.5 V is shown in Figure 4.9.  $C_{ZnO}$  increases with increasingly negative potential. This is consistent with crack propagation since, in first approximation,  $C_{ZnO}$  is proportional to the “pore” surface in contact with the electrolyte. In Figure 4.9a, there is no obvious degradation on the ZnO surface after the polarization at -0.4V (compare Figure 4.9a with the as-deposited state in Figure 4.2b). In contrast, Figure 4.9b reveals significant damages after the polarization at -0.5 V. These findings confirm that the propagation of the cracks goes from the surface towards the substrate (probably along some of the column boundaries) till causing local delamination of the films. This also shows that the first stages of crack propagation can go unnoticed using only ex situ SEM top-view analysis (Figure 4.9a), highlighting the beneficial complementarity of the in situ EIS technique.

Crack propagation is already initiated between -0.3 V and -0.4 V which is much lower than the film rupture potential estimated at ca. -0.6 V in Chapter 3. This is explained by the fact that, in the second model,  $C_{ZnO}$  is “visible” (i.e. not masked by the double layer capacitance  $C_{dl}$ ) only at low values that correspond to the first stage of the layer degradation. For this matter, EIS proves to be a much more sensitive technique than DC polarization curves.

Low values of  $C_{ZnO}$  also suggest that the formation of cracks is localized. The DeLevie model provides only global “averaged” information over the whole surface of the ZnO in contact with the electrolyte. The depth, the width and the spatial distribution of the cracks cannot be assessed. A zoom-out on the micrograph of the sample polarized at -0.5 V (Figure 4.9c) evidences that delamination is localized in some areas (where the copper substrate is clearly exposed) while other areas look damage-free (Figure 4.9c). When this delamination state is reached, most of the stress in the layer is probably released. Then the model developed in this study, that links the impedance of the ZnO layer to its mechanical instability, probably fails to apply.

Finally, the smooth dependence of  $C_{ZnO}$  on the applied potential (Figure 4.8b) is another clue indicating that the degradation could be related to the nature properties of the (002)-textured ZnO (as already described in Chapter 3).

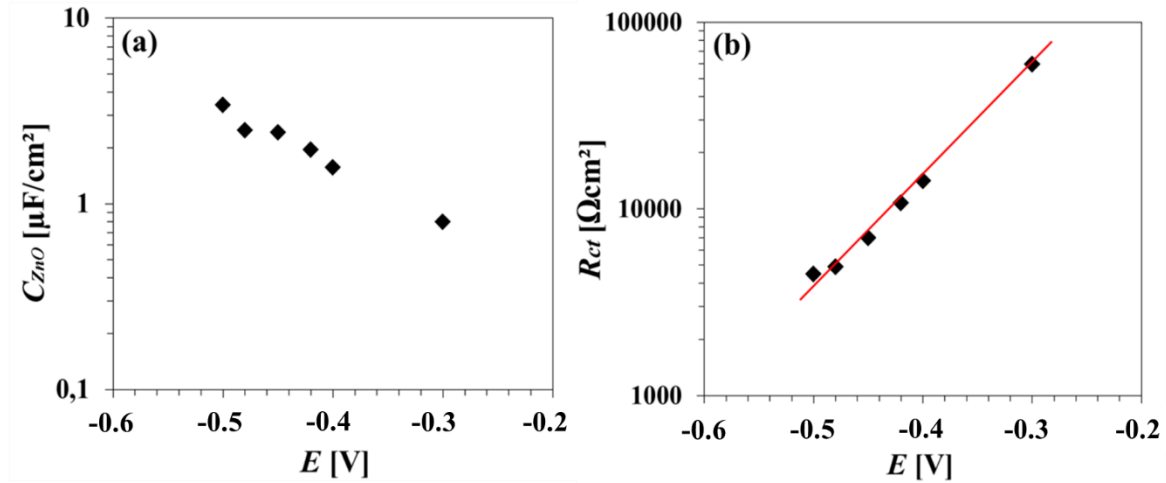


Figure 4.8: Dependence of the ZnO capacitance (a) and the charge transfer resistance  $R_{ct}$  (b) on the applied potential using the second equivalent circuit model.

In Figure 4.8b,  $R_{ct}$  exhibits an exponential dependence on the applied potential which is consistent with the oxygen reduction reaction whose kinetics would be essentially limited by charge transfer. Though it is not the main focus of the study, this result consolidates the reliability of the physical model and the efficiency of the fitting process.

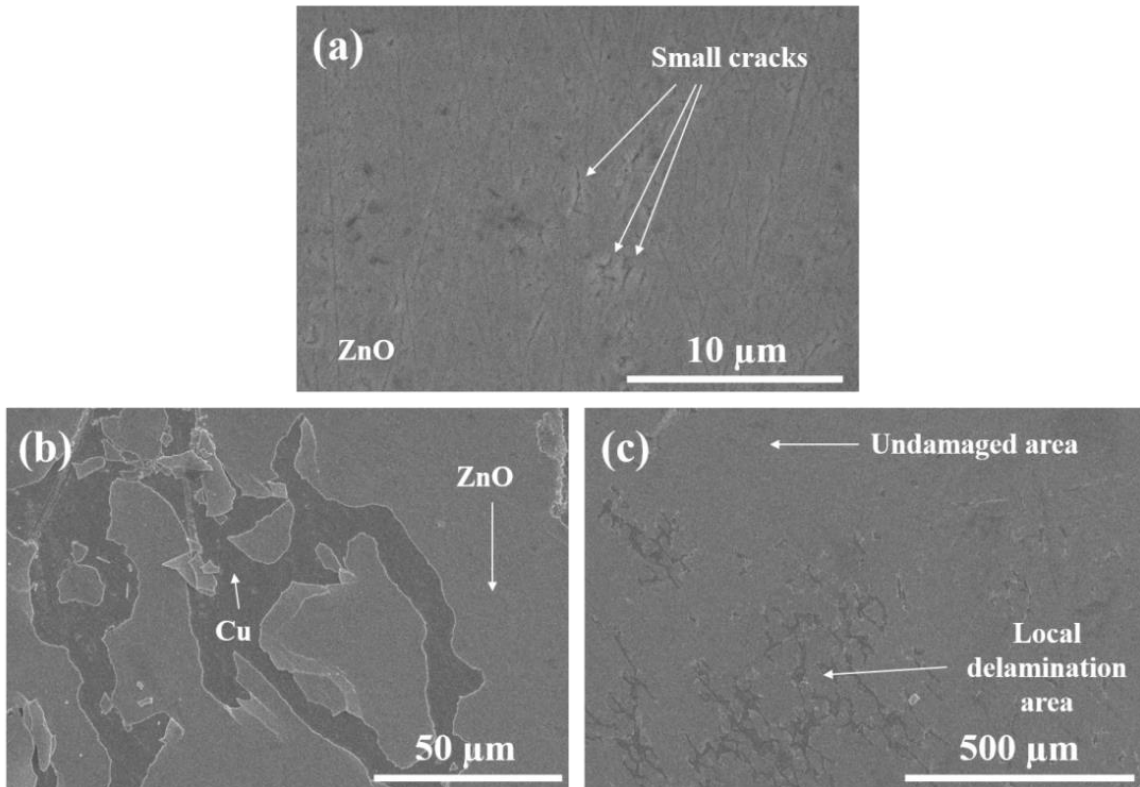


Figure 4.9: Post-mortem analysis of the ZnO layers at different potentials. Top-view SEM micrographs of the ZnO layers polarized at -0.4 V (a) and at -0.5 V (b,c). The Cu substrate appears in darker contrast as the ZnO layer.

Figure 4.10 schematically presents the main electrochemical and microstructural results so as to summarize the main findings of this study. Three scenarios are considered based on different micro/nanostructures and their expected capacitance  $C$ . Figure 4.10a shows a fully dense structure. This structure is in accordance with the STEM analysis (Figure 4.2a). For such structure, the first model (Figure 4.4) is suitable and  $C$  should be in the range of usual double layer capacitance values, i.e. 10-100  $\mu\text{F}/\text{cm}^2$ . Yet the capacitance measured during the impedance experiments is much lower. Hence this scenario is rejected. Figure 4.10b shows the same textured layer as in Figure 4.10a but with numerous gaps between the columns. This nanostructured is not in agreement with the STEM image of the as-deposited ZnO layers (Figure 4.2a). Virtually this open nanostructure could have been generated by a homogenous (i.e. non-localized) crack propagation along most of the column boundaries. This assumption is not supported by Figure 4.9c. Moreover, such nanostructure would have yielded large values of  $C_{\text{ZnO}}$  that would have been masked by  $C_{dl}$ . This second scenario is therefore also invalid. Thus, the only way to explain the low capacitance value is the localized crack propagation (leading to microscale damages and delamination) in an originally dense structure (at the nanoscale), as shown in Figure 4.10c.

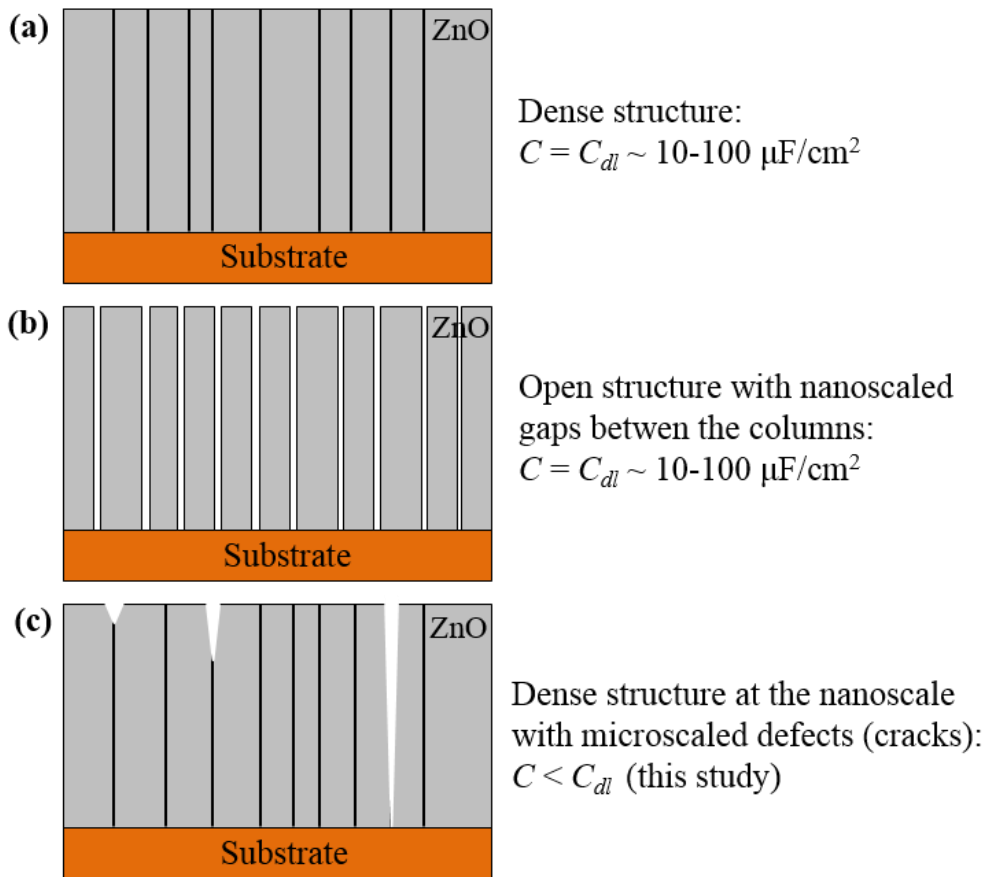


Figure 4.10: Schematic interpretation of the impedance results in relationship with the ZnO microstructure: (a) fully dense layer, (b) layer with nanoscaled gaps between the columns and (c) dense with microscaled cracks.

#### 4.4. Conclusions

The degradation of the (002)-oriented ZnO layers presented in Chapter 3 was investigated by EIS and electron microscopy. It was found that the structure of the as-deposited ZnO film was dense at the nanoscale with no gaps between the columns. An equivalent circuit model including the De Levie impedance was developed to account for the localized crack propagation under DC polarization. The growth of cracks generates a capacitance ( $C_{ZnO}$ ) that is approximated to be proportional to the crack inner surface in contact with the electrolyte. Due to its localized nature,  $C_{ZnO}$  is sufficiently small so that its impedance is not masked by that of the double layer capacitance existing at the top of the ZnO surface. The good fitting of the experimental impedance data was obtained by taking advantage of the flexibility of the De Levie model that can describe “real” electrodes whose microstructures are far from an ideal array of identical cylindrical pores. EIS appears to be a more accurate method than DC voltammetry (as used in Chapter 3) to evidence the early stages of the ZnO layer degradation. The methodology used in this study combining global *in*



*situ* impedance data with local *ex situ* nano/macro-structural data proved to be efficient to investigate porous electrochemical systems regardless of the model used to describe the electrode (DeLevie, Young, power law...). This statement is also illustrated by the interesting study of Barrès *et al.* (presented in the introduction) using a similar combination of techniques to analyze the nanoporosity of silicon nitride thin films [1]. The gradual increase of  $C_{ZnO}$  with the applied potential suggests that the crack development is related to the nature of the (002)-oriented ZnO (potential-dependent, observed in Chapter 3). This finding is also supported by the results of Chapter 5 in which such degradation is not observed. In this next chapter, ZnO layers with no preferred orientation are produced with magnetron sputtering using a zinc target. The microstructure, the capacitance and the mechanical stability of the films as well as their electrochemical behavior towards ORR are investigated and compared with the data obtained in Chapter 3 and 4 with textured ZnO.

### 4.5. References

- [1] T. Barres, B. Tribollet, O. Stephan, H. Montigaud, M. Boinet, Y. Cohin, Characterization of the porosity of silicon nitride thin layers by Electrochemical Impedance Spectroscopy, *Electrochimica Acta*, 2017, 227, 1-6;
- [2] L. Young, Anodic oxide films. Part 4.-The interpretation of impedance measurements on oxide coated electrodes on niobium, *Trans. Faraday Soc.* 51 (1955) 1250;
- [3] B. Hirschorn, M. Orazem, B. Tribollet, V. Vivier, I. Frateur, M. Musiani, Constant-phase-element behavior caused by resistivity distributions in films I. Theory, *J. of Electrochem. Soc.*, 2010, 157, C452-457;
- [4] R. de Levie, Electrochemical response of porous and rough electrodes, *Adv. Electrochem. Electrochem. Eng.* 6 (1967) 329;
- [5] O. E. Barcia, E. D. Elia, I. Frateur, O. R. Mattos, N. Pébère, B. Tribollet, Application of the impedance model of de Levie for the characterization of porous electrodes, *Electrochimica Acta* 47 (2002) 2109-2116;
- [6] Lasia, J. Impedance of porous electrodes, *Journal of Electroanalytical Chemistry*, 397 (1995) 27-33;
- [7] C. Hitz, A. Lasia, Experimental study and modeling of impedance of the her on porous Ni electrodes, *Journal of Electroanalytical Chemistry*, 500 (2001) 213-222;
- [8] J.-P. Candy, P. Fouilloux, M. Keddou, H. Takenouti, The pore texture of raney-nickel determined by impedance measurements, *Electrochimica Acta*, 27 (1982) 1585-1593;

- [9] T. T. M Tran, B. Tribollet, E. M. M Sutter, New insights into the cathodic dissolution of aluminium using electrochemical methods, *Electrochimica Acta*, 2016, 216, 58-67;
- [10] J. Sakabe, N. Ohta, T. Ohnishi, K. Mitsuishi, K. Takada, Porous amorphous silicon film anodes for high-capacity and stable all-solid-state lithium batteries, *Communications chemistry*, 2018, 1-24;
- [11] V. Godinho, P. Moskovkin, R. Álvarez, J. Caballero-Hernández, R. Schierholz, B. Bera, J. Demarche, A. Palmero, A. Fernández, S. Lucas, On the formation of the porous structure in nanostructured a-Si coatings deposited by dc magnetron sputtering at oblique angles, *Nanotechnology*. 2014; 25, 355705;
- [12] B. Hirschorn, M.E. Orazem, B. Tribollet, V. Vivier, I. Frateur, M. Musiani, Constant-Phase-Element Behavior Caused by Resistivity Distributions in Films. II. Applications, *J. Electrochem. Soc.*, 2010, 157, C458-463;
- [13] M. E. Orazem, N. Pébère, B. Tribollet, Enhanced Graphical Representation of Electrochemical Impedance Data, *J. Electrochem. Soc.*, 2006, 153, B129;
- [14] M. E. Orazem, B. Tribollet, *Electrochemical Impedance Spectroscopy*, John Wiley & Sons, 2<sup>nd</sup> ed., 2017;
- [15] J. R. Macdonald, *Impedance Spectroscopy Emphasizing Solid Materials and Systems*, John Wiley & Sons, New York, 1987;
- [16] G. J. Brug, A. L. G. Van Den Eeden, M. Sluyters-Rehbach, The analysis of electrode impedances complicated by the presence of a constant phase element, *J. H. Sluyters, J. Electroanal. Chem.*, 1984, 176, 275;

## Microstructural and electrochemical investigations on non-textured ZnO layers

---

### Abstract

In this chapter, non-textured ZnO films were synthesized by rf-magnetron sputtering using a zinc target. The absence of preferred orientation was verified by XRD. AFM and SEM top-view images evidenced the nano-granular structure. HAADF-STEM micrographs reveal a porous structure with pore size and grain size around 10 nm. This was consistent with EIS analysis that suggested a large zinc oxide capacitance. The narrowness of the pores enabled to approximate that oxygen reduction took place at the surface of the layers. Under DC polarization, the non-textured ZnO films proved to be mechanically stable. Yet they became rougher due to the presence of numerous oxygen-rich nodules on the surface. The non-textured ZnO electrodes exhibit a high activity towards ORR. RRDE measurements coupled with ORR modelling allowed to quantitatively demonstrate that the direct reduction prevailed with the indirect pathway being active as well. The latter was shown not to stop at the production of hydrogen peroxide. However, the uncertainty on the rough electrode surface area did not allow to determine which reaction hydrogen peroxide underwent (reduction to OH<sup>-</sup> anions and/or chemical decomposition into oxygen molecules).

*A modified version of this chapter will be submitted to ChemElectroChem: Microstructural and electrochemical investigations on nano-granular ZnO layers. J. Soares Costa, M. Prestat, B. Lescop, S. Rioual, B. Tribollet, L. Holzer, D. Thierry.*

### 5.1. Introduction

In this Ph.D. thesis, we aim at producing ZnO layers that are suitable for the investigation of oxygen reaction with the rotating ring disk electrode technique. Ideally these films are dense, smooth and mechanically stable. In the previous chapters, compact columnar layers with an homogeneous thickness were successfully deposited by sputtering using a ZnO target. Unfortunately, those films suffered from mechanical instability which was dependent on the applied potential. It is believed that this issue is related to the nature properties of the (002)-oriented ZnO. The lack of mechanical reliability led to film delamination and limited ORR investigations. Hence the motivation for the present chapter was to circumvent this

issue by synthesizing non-textured ZnO layers that exhibited improved mechanical stability. Note that this type of films may also be called “nano-granular” or “with no preferred orientation”.

Figure 5.1 shows a schematic of the different ZnO microstructures that can be obtained with the sputtering technique and that are suitable for RRDE investigations. Figure 5.1a presents a dense and compact layer for which ORR occurs on the film surface. This structure was obtained in Chapters 3 and 4 along with the stability issues mentioned above. Figure 5.1b depicts a non-textured structure with micro-scaled grains and pores. The latter are sufficient large to enable the electrolyte to penetrate easily in the ZnO. In that case, the ORR active sites can also be found on the walls of the pore network below the surface. This makes the investigation of the ORR mechanism much more complex than that occurring at the surface of a dense electrode. The structure of Figure 5.1c also has no preferred orientation, but grains and pores are nano-scaled. The narrowness of the pores ( $< 10\text{-}15\text{ nm}$ ) generates a strong resistance to the transport of electroactive species within the ZnO layer. Thus, ORR can be approximated to take place on the surface of the film. Though not completely dense, this kind of film is acceptable for the RRDE investigations intended in the present chapter.

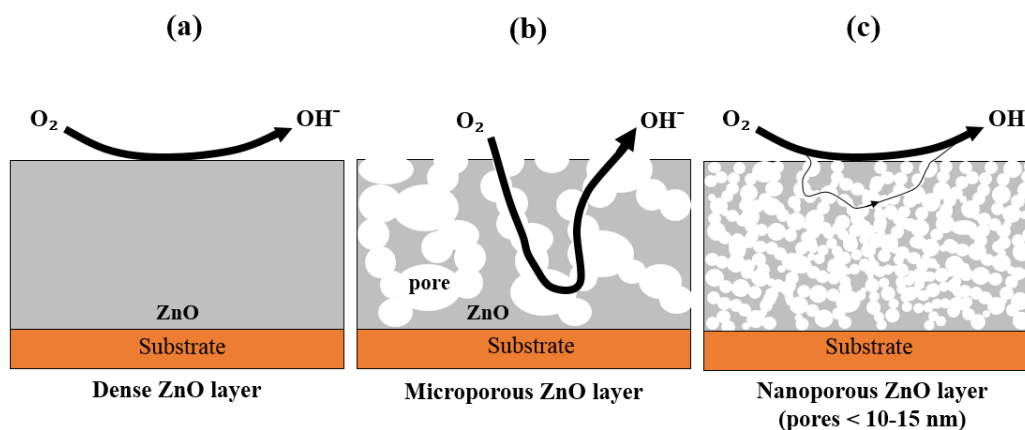


Figure 5.1: Schematic of the impact of microstructure on the oxygen fluxes during ORR: (a) dense layer, (b) layer with micro-scaled pores and (c) layer with nano-scaled pores. Thick arrows represent large fluxes whereas thin arrows depict minor fluxes.

To the best of our knowledge, no synthesis of dense nano-granular ZnO layers using “one-step” sputtering (with no annealing post-treatment) has been reported before. The data available in the literature involving sputtering technique is related to the production of films with preferred (002) orientation [1-6] or to nanoporous ZnO films using thermally oxidized substrates [7,8], etching process [9,10] or heat-treatment after deposition [11-15]. To obtain

sputtered ZnO films with no preferred orientation, some authors modified the pressure of oxygen on the deposition procedure [16-18]. It seems to be a trend indicating that, when the O<sub>2</sub> partial pressure is increased, more randomly-oriented grains are observed during XRD experiments. Sasi *et al.* deposited ZnO films on 3C-SiC-on-Si substrates by using rf-sputtering technique with zinc target, changing the O<sub>2</sub>/Ar gas ratio and annealing the layers at different temperatures [16]. The authors observed that a mixture containing 50% O<sub>2</sub> and 50% Ar showed three peaks (100, 002, 101) on the XRD diffractogram with practically the same intensity after annealing at 600°C. No data on the crystalline structure without annealing was supplied, suggesting that the as-deposited films were probably (002)-oriented. No microstructural data on the porosity was reported.

Abdallah *et al.* prepared ZnO thin films with rf-magnetron sputtering (with zinc oxide target) using glass as substrate and varying the oxygen flow rate [17]. No post-deposition heat-treatment was done. They observed that increasing the flux of O<sub>2</sub> resulted in the decrease of the (002) orientation and in the appearing of the (100) reflection. No reliable microstructural information was reported. Maslyk *et al.* synthesized Zn/ZnO films with DC magnetron sputtering (zinc target) by increasing the gas flow rates while keeping the same 10:1 Ar:O<sub>2</sub> ratio [18]. Due to the limited amount of oxygen, the produced films were essentially made of zinc. Yet it is interesting to observe from cross-sectional SEM micrographs that the porosity of the layers decreases with increasing oxygen flow rate.

The aim of this chapter was to synthesize non-textured layers with no pore or pores in the nanometer range (<10-15 nm) with rf-magnetron sputtering and to investigate the ORR mechanism and kinetics with RRDE. The layers were produced using a zinc target and different fluxes of oxygen during sputtering. They were characterized by XRD, conventional SEM, EDX, XPS, FIB-SEM, HAADF-STEM and impedance spectroscopy. The DC behavior of the ZnO layers towards oxygen reduction was investigated using chronoamperometry, potentiodynamic voltammetry and RRDE. A reaction mechanism was proposed and used to quantitatively evaluate the ratio between direct and indirect oxygen reduction. The results of this chapter were compared with those obtained with textured films.

## 5.2. Experimental Section

### 5.2.1. Synthesis of the ZnO layers

The non-textured ZnO films were deposited on copper substrates (diameter 5 mm) by radio-frequency magnetron sputtering deposition method (Univex 350, Oerlikon) using a Zn target. The details of the preparation of the cylindrical copper substrates have been described

in Chapter 3. For some depositions, glass substrates were used. For sputtering deposition, the working chamber was vacuumed to reach a base pressure of  $4.8 \times 10^{-7}$  mbar. The substrates were fixed at a distance of ca. 10 cm parallel to the Zn target surface. Film deposition was tested with various mixtures of reactive gas (Ar:O<sub>2</sub> from 20:0 to 20:3) inside the chamber. The gas purities were 99.9996% for Argon and 99.9995% for O<sub>2</sub>. Pre-sputtering was carried out for 30 min to clean and equilibrate the target surface prior to deposition. The same conditions were used for pre-sputtering and sputtering, except deposition time. During deposition, the total pressure was kept at  $1.7 \times 10^{-2}$  mbar. The input power at the target was fixed at 250 W.

### 5.2.2. Characterization of the ZnO layers

A Profilometer (Tencor P-10) was used to estimate the layer thickness.

X-ray diffraction (XRD) was used to analyze the crystalline structure of non-textured ZnO layers using PANalytical Empyrean apparatus with CuK radiation ( $1.5408 \text{ \AA}$ ). The chemical composition of the surface was assessed by X-ray photoelectron spectroscopy (XPS) using an Al-K $\alpha$  X-ray source (Thermo VG) and a cylindrical mirror analyzer (RIBER). The surface topography of the films was studied with an atomic force microscope (Multimode 8 FM from Bruker) in tapping mode.

Top-view secondary electron imaging was performed with a field emission SEM (FEI Quanta 200F) at 20 kV to characterize the surface microstructure of the ZnO layers. The machine was equipped with an energy dispersive X-ray spectroscopy (EDX) system from EDAX (Octane Super, with TEAM software) that enabled to determine the composition of the layers. EDX spot analyses were acquired at 20 kV and results are given in atom%.

Cross-sectional analysis of the internal microstructure of the ZnO layers was performed by FIB-SEM (FEI Helios NanoLab 600i) to provide a first hint of the compactness of the layers and to assess their thickness. First, a 1  $\mu\text{m}$  thick protective layer (Pt or C) was applied on top of the ZnO surface at the location of interest with ion beam induced deposition. Cross-sections of 20-30  $\mu\text{m}$  width and 5-10  $\mu\text{m}$  depth are then milled and polished with FIB. The prepared cross-sections were finally investigated with low acceleration voltage SEM (2kV).

The nanostructure of the ZnO layers was further investigated with high resolution scanning transmission electron microscopy (STEM, FEI Talos F200X) at 200 kV. For this purpose, electron transparent TEM lamellas (thickness ca. 50 nm) were fabricated with FIB.

The High-Angle Annular Dark Field (HAADF) detector provided the best contrast settings for capturing the internal pore structure of the ZnO layers.

### 5.2.3. Electrochemical measurements

The electrochemical analyses were conducted at room temperature with the same electrolyte as in the previous chapters (KOH solutions, pH 10 +/- 0.1, with KCl 0.2 M as supporting electrolyte). EIS was used to evaluate *in situ* the degree of porosity of the layers. The spectra were recorded between  $10^5$  Hz to 1 Hz with 10 points per decade using 10 mV of sinusoidal perturbation. Lower frequencies (less than 1 Hz) were not used because the most relevant porosity information is found at high frequencies (see Chapter 4). As in Chapter 4, fitting of the experimental impedance data with the proposed equivalent circuit model was carried out using non-commercial software developed at the Laboratoire Interfaces et Systèmes Electrochimiques (LISE), Paris, France [19,20].

Oxygen reduction (ORR) was investigated using chronoamperometry and the rotating ring disk electrode (RRDE, same setup as in Chapter 3). The disk and the ring currents were collected simultaneously at fixed potentials while varying the rotation rate. The counter-electrode was a large titanium-based metallic grid placed below the working electrode. The reference electrode was a mercury/mercury oxide electrode (Hg-HgO, KOH 1M). The potential of the ring electrode was set at + 0.850 V (vs. Hg-HgO). Disk polarization curves were recorded with scan rates of 0.5 to 1 mV/s. The electrochemical measurements were repeated at least three times for each experiment.

### 5.3. Results and discussion

The first step of this study was to determine the sputtering parameters for ZnO deposition (on copper) using a Zn target. The main experimental parameter was the oxygen flow (in sccm, that is a flow measurement term indicating  $\text{cm}^3/\text{min}$  in standard conditions of the fluid). Was reported to have a significant influence of the microstructure changing this parameter [18]. All the other deposition parameters were kept constant. The produced samples are listed in Table 5.1.

Sample name	Mixture of reactive gas Argon: O <sub>2</sub> (sccm)	ZnO film thickness	Deposition time (min)
A	20:3	~ 600 – 800 nm	5
B	20:2	~ 700 nm	7
C	20:0	~ 1 $\mu$ m	15

Table 5.1: Initial parameters to produce non-textured ZnO films using Zn target.

After deposition, was used a profilometer to estimate the film thickness. Also, the films were analyzed by XRD and SEM (Figure 5.2). There is an obvious dependence of the microstructure and the crystalline structure on the oxygen flow. Denser structures were obtained high oxygen flow (sample A, 3 sccm) while highly porous films were produced with low oxygen flow (sample C, 0 sccm). Sample C is thus clearly not suitable for the present study. Furthermore, their XRD analysis reveals that the presence of crystalline zinc which is in agreement with the findings of Maslyk *et al.* [18] mentioned in the introduction.

For the rest of this study, sample A was selected since its surface looks dense using top-view SEM images. Furthermore, its crystalline structure revealed no preferred orientation. The deposition time was fixed at 5 min, yielding thicknesses between 600 and 800 nm (depending on the sample). In comparison, sample B had a slightly more open microstructure and a more relevant zinc contribution in the zinc diffractogram.



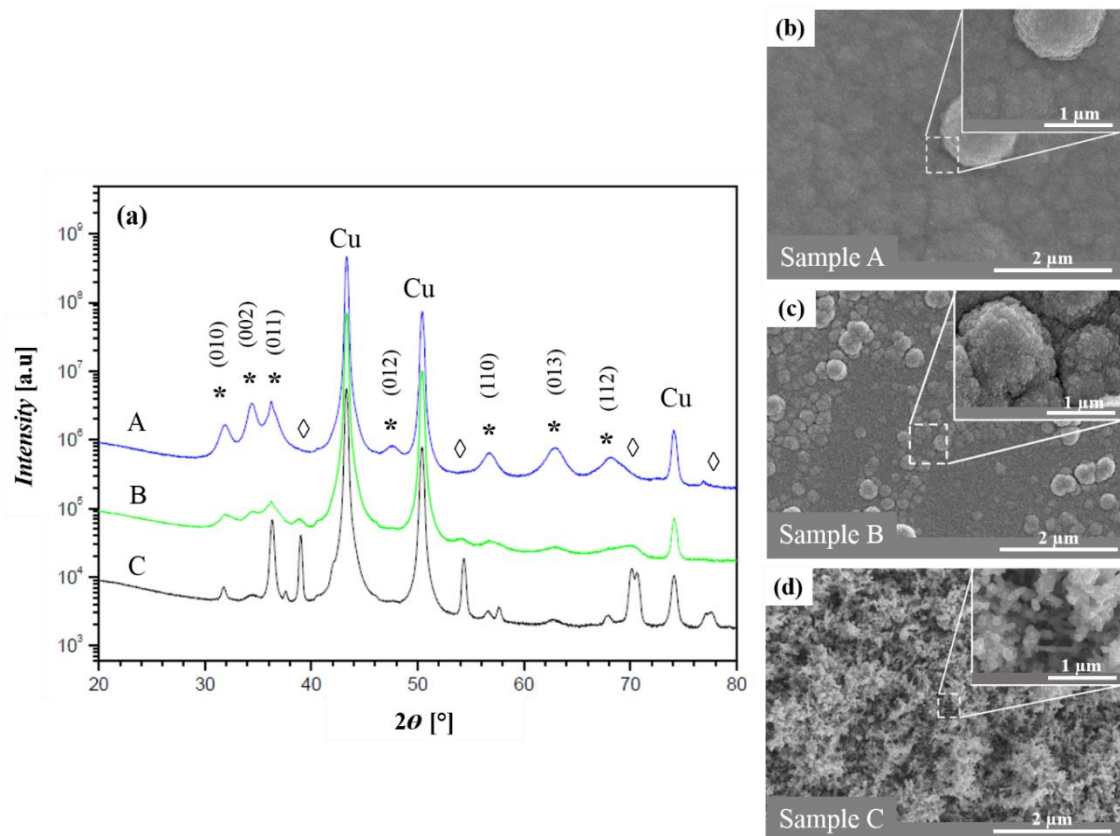


Figure 5.2: Influence of oxygen flux on the crystalline structure and the microstructure of the layers during sputtering deposition with zinc target. The experimental parameters corresponding to the samples A, B and C are found in Table 5.1. (a) XRD diffractograms with \* denoting the ZnO peaks and  $\diamond$  the Zn reflections; (b-d) SEM top-view micrographs.

A comparison of XRD pattern between non-textured (this chapter) and textured ZnO films (Chapters 4 and 5) is presented in Figure 5.3. There is a marked difference between the two samples. While the textured samples exhibit essentially a well-defined (002) peak (c-axis orientation perpendicular to the substrate) at ca.  $34^\circ$ , the diffractogram of the samples prepared in this chapter displays multiple crystalline orientations, the most important being the (002), (010) and (011). This demonstrates that the layers produced with the zinc target with the 20:3 sccm Ar:O<sub>2</sub> gas mixture has no preferred orientation (*i.e.* they are “non-textured”), which was one of the goals of this study. Debye-Scherrer analysis yielded an averaged grain size of 9 nm, confirming the nano-granular nature of the structure. The inset in Figure 5.3 shows the different colors obtained for each type of film.

According to the literature, ZnO films with preferred (002) orientation tends to be transparent [21], as observed here. ZnO films may have different colors that are associated with an increase in oxygen vacancies inside the layer [22]. This assumption can be made for

explaining the black color of the non-textured films Further work is needed to confirm this hypothesis (beyond the scope of this Ph.D. thesis).

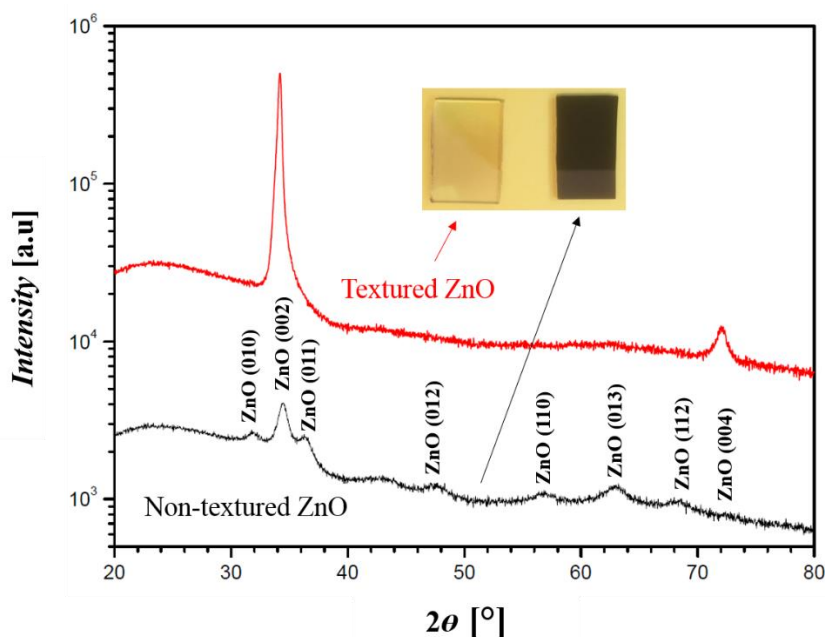


Figure 5.3: XRD spectra of textured (red curve) and non-textured (black curve) ZnO films deposited on glass. Note the log-scale of the y-axis. Inset: photographs of the two types of films.

The XPS analysis of the non-textured films is shown in Figure 5.4. The films exhibited only the Zn and O peaks. No other impurities were observed on the surface of the samples. The O (1s) peak was centered at 531 eV that is related to the  $O_2^-$  in the ZnO structure. The Zn (2p) and Auger Zn (LMM) spectra were centered at 1022 and 989 eV, respectively, exhibit only one peak, revealing the presence of ZnO on the surface. No metallic zinc was found. The derived  $\alpha$  Auger parameter is 2011 eV, close to the value expected for ZnO (2010.4 eV) [23].

The morphology of the surface of the layers is presented in Figure 5.5. Top-view SEM micrographs show that the ZnO films consists of a base layer on top of which one can see “nodules” of *ca.* 0.5  $\mu\text{m}$  to 1  $\mu\text{m}$ . The base layer looks rather compact. It consists of very small grains hinting at the desired nano-granular structure. The latter can also be seen in the AFM image (Figure 5.5b). Figure 5.5c is a cross-sectional FIB-SEM image of a nodule “inserted” in the base layer with a gap fitting the shape of the nodule. To the best of our knowledge, similar peculiar structure has not been reported in the literature yet. The estimated thickness of non-textured ZnO films was approximately 700 nm for 5 minutes of deposition (growth rate: 140 nm/min).

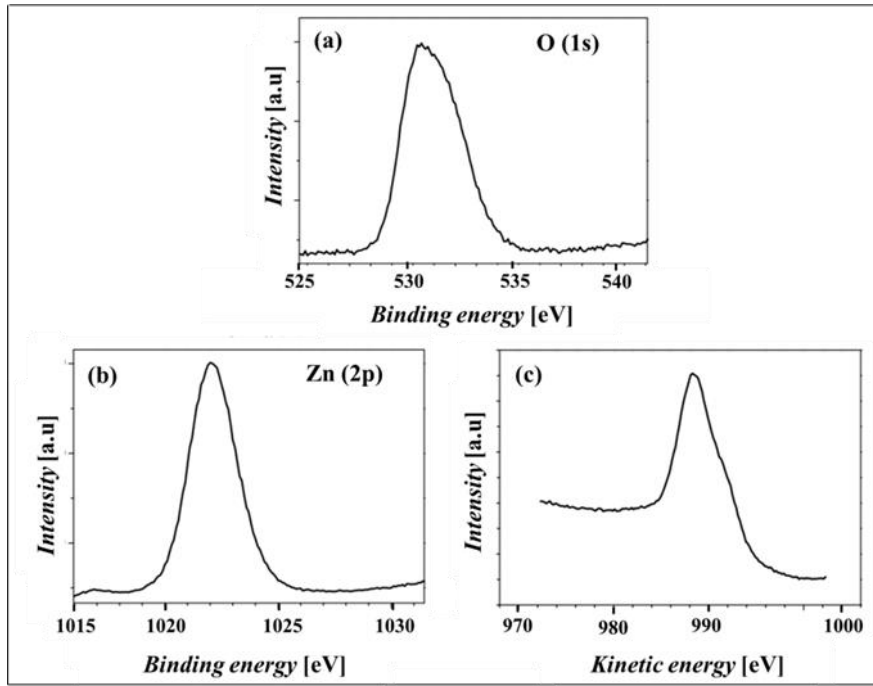


Figure 5.4: Surface analysis of the ZnO films: a) XPS spectrum of O (1s); b) XPS spectrum of Zn (2p<sub>3/2</sub>); c) Auger spectrum of Zn (LMM).

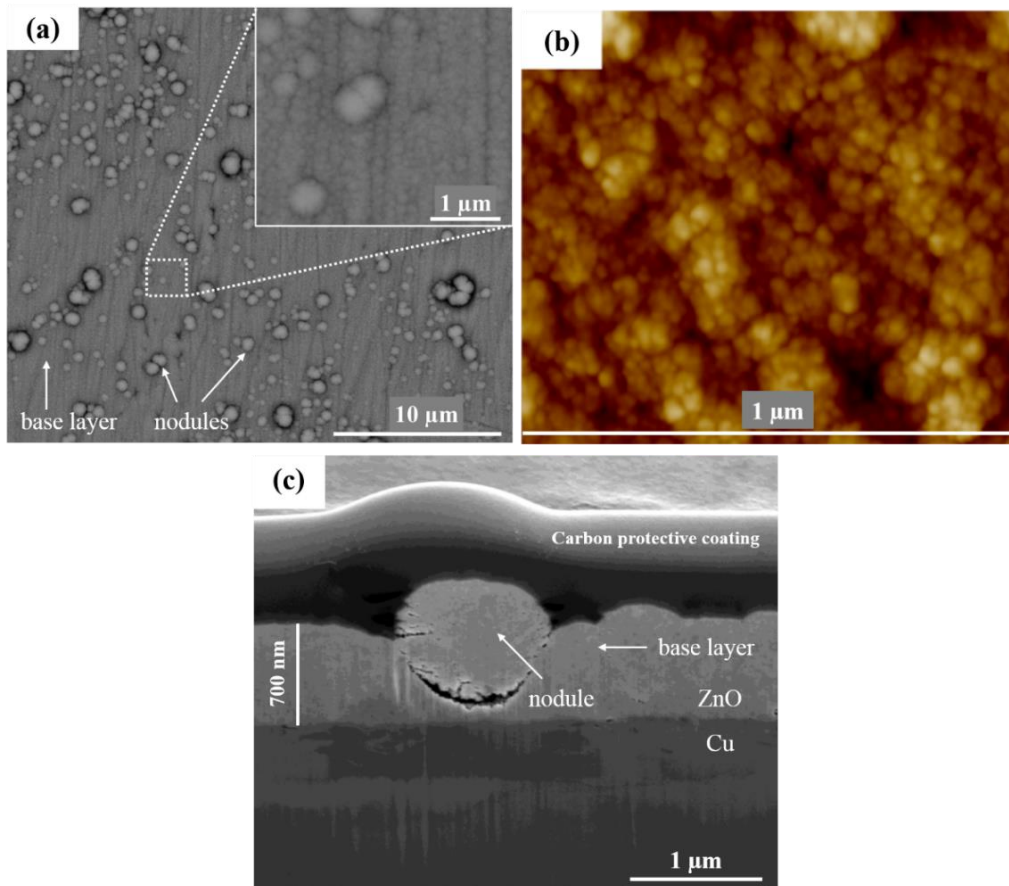


Figure 5.5: Microstructure analysis of the as-deposited non-textured ZnO films: (a) top-view SEM micrograph, (b) AFM surface image and (c) FIB-SEM micrograph of the layer cross-section.

EDX spot analyses were carried out for both the base layer and the nodules (ten measurements for each). The composition of the as-deposited ZnO films is close to the nominal 50:50 Zn:O atomic ratio (52:48 for the base layer, 45:55 for the nodules) within the accuracy limits of this technique.

Figure 5.6 displays the HAADF-STEM cross-sectional images of the as-deposited non-textured ZnO layers. Although hints exist about some vertical organization of the ZnO and pores (which is consistent with the presence of the (002) peak on the XRD diffractogram) in Figure 5.6a, this nanostructure is clearly different from that of the well-oriented columnar ZnO presented in the Figure 4.2b of Chapter 4. The images reveal that the layers are nanoporous with pores mostly narrower than 10 nm (with a couple of large pores around 15-20 nm). Grain size is in the range of 10 nm which is consistent with the Debye-Scherrer analysis mentioned above. Hence the nanostructure of the non-textured ZnO corresponds well to that schematically depicted in Figure 5.1c. It is believed that the electrolyte might penetrate the pore network (see EIS analysis below) but, from a kinetic point of view, ORR takes place essentially at the surface of the layer.

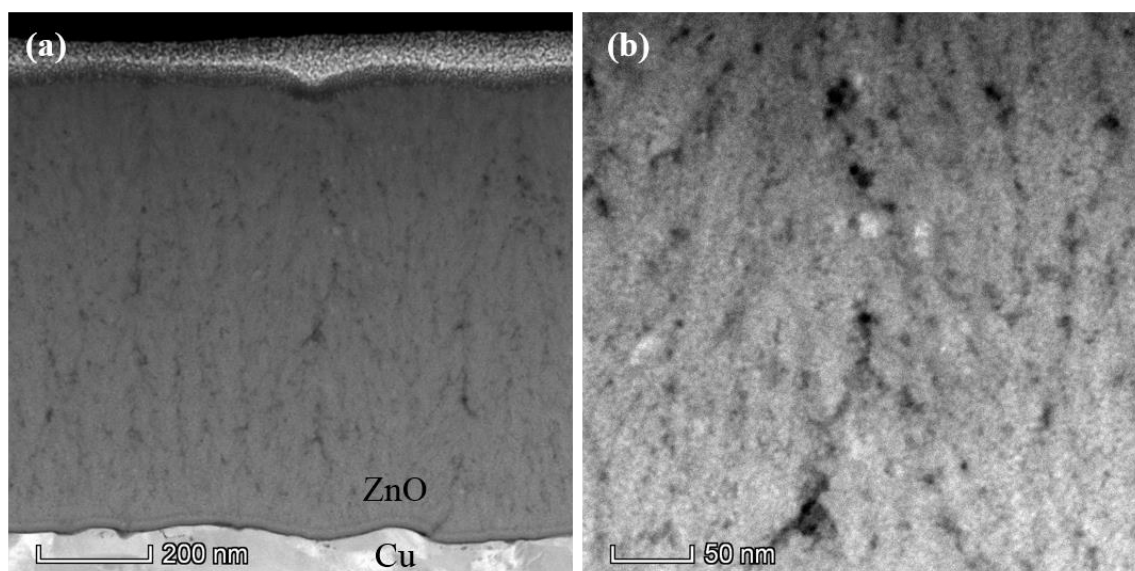


Figure 5.6: Microstructure analysis of the as-deposited non-textured ZnO films by HAADF-STEM: (a) micrograph showing the whole thickness of the layer at moderate magnification; (b) zoom-in allowing for the estimation of the size of the pores (that appear in black contrast).

Following a similar approach as in Chapter 4, EIS was used in this chapter to characterize *in situ* the porosity of the ZnO layers. Figure 5.7 shows the impedance data for ZnO films at -0.7 V (OCP was ca. -0.1 V). This potential was chosen because it is far from OCP which allows to simplify the faradaic impedance to its sole cathodic branch. The Bode

plots (Figures 5.7b and 5.7c) were first corrected from the electrolyte resistance that was obtained by extrapolation of the high frequency impedance to the real axis in the Nyquist plot (Figure 5.7a and 5.7b).

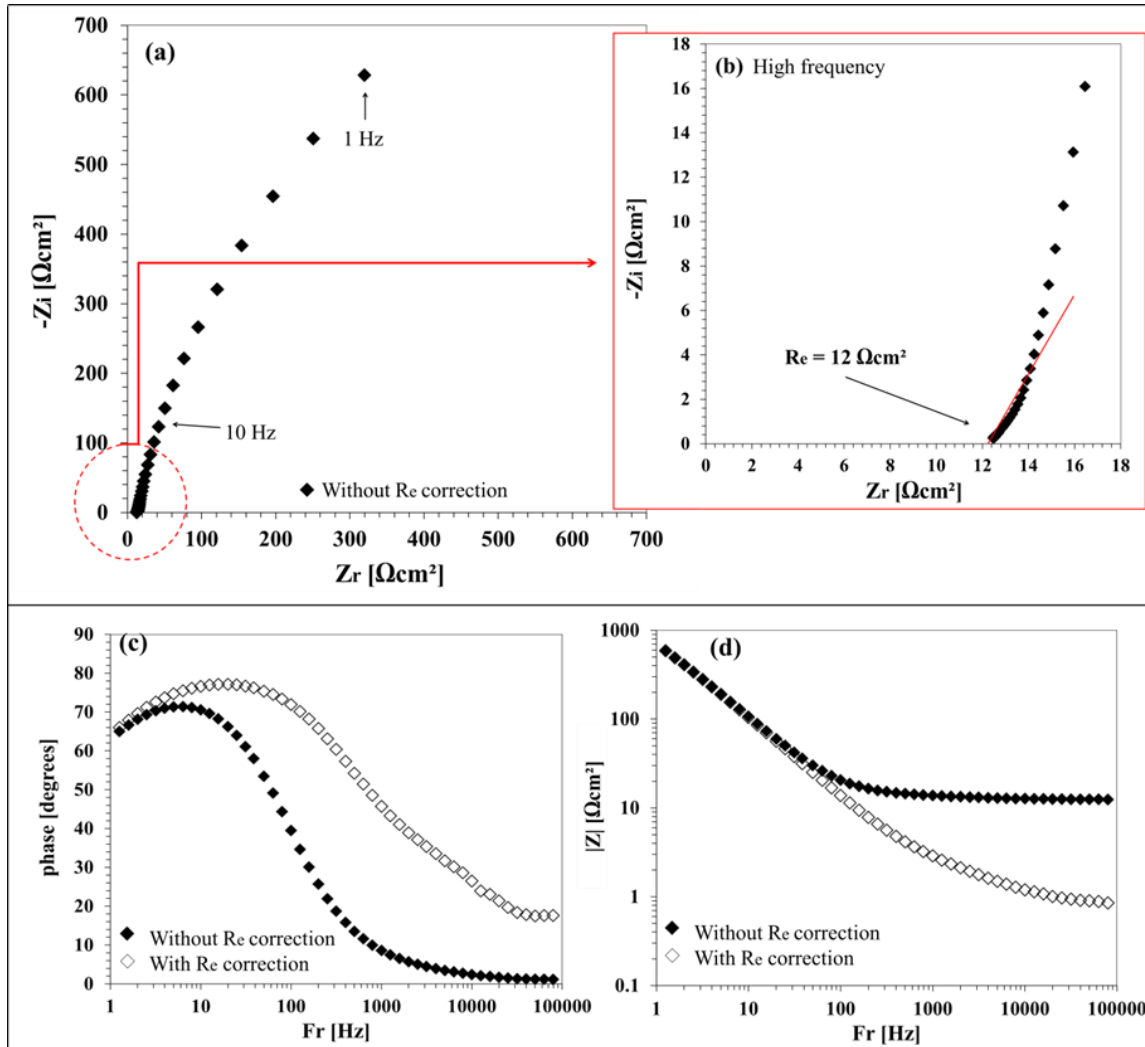


Figure 5.7: EIS diagrams recorded at  $-0.7$  V and at a rotation rate of 200 rpm. (a) Nyquist plot with (b) zoom in high frequency to determine the electrolyte resistance ( $R_e$ ). Bode plots (without and with  $R_e$  correction): (c) phase curve and (d) modulus curve.

In view of the change of slope in Figure 5.7d, the equivalent circuit used for describing the experimental impedance,  $Z_{exp}$ , is almost the same as the second model of Chapter 4. The ZnO impedance,  $Z_{ZnO}$ , is represented by a De Levie impedance:

$$Z_{ZnO} = \sqrt{\frac{R_0 Z_0}{m^2}} \coth \sqrt{\frac{R_l}{Z_0}} \quad (1)$$

with  $R_0$  being the electrolyte resistance per unit of pore length with units of  $\Omega \cdot \text{cm}^{-1}$  and  $m$  is the number of pore per  $\text{cm}^2$ .  $R_1$  is product  $l^2 R_0$ , where  $l$  is the length of the cylindrical pore of the “ideal” electrode of DeLevie [24].  $Z_0$  is the interfacial impedance per unit length of pore (expressed in  $\Omega \cdot \text{cm}$ ). One assumes no charge transfer reaction in the pores.

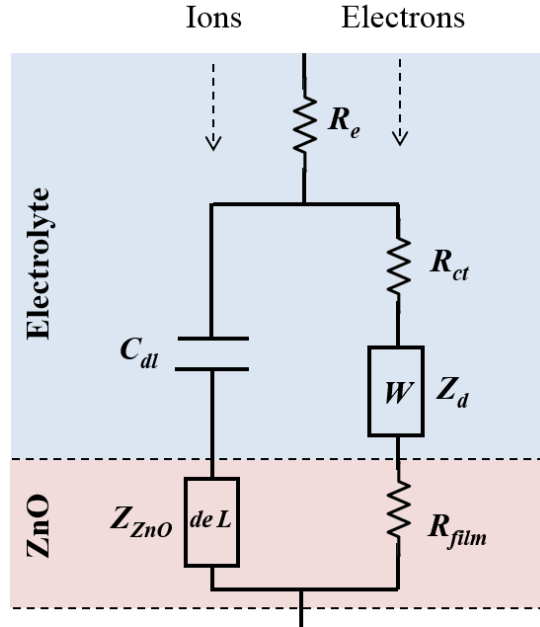


Figure 5.8: Equivalent circuit model accounting for the penetration of the electrolyte into the ZnO layer using a DeLevie impedance.

$Z_0$  is described by a CPE whose frequency-independent parameters are  $Q_{pore}$  and  $\beta$ :

$$Z_0 = \frac{1}{Q_{pore}(j\omega)^\beta} \quad (2)$$

with  $\omega$  being the angular frequency.

At high frequencies, the impedance of ZnO is “visible”, as suggested by the decrease of slope in the Bode plot of the modulus (Figure 5.7d).  $\coth \sqrt{\frac{R_l}{Z_0}}$  is equal to 1. Then  $Z_{ZnO}$  can be expressed as:

$$Z_{ZnO} = \sqrt{\frac{1}{Q_1(j\omega)^\beta}} \quad (3)$$

with

$$Q_1 = \frac{Q_{pore} m^2}{R_0} \quad (4)$$

The faradaic impedance,  $Z_f$ , consists of a charge transfer resistance,  $R_{ct}$ , in series with a diffusion (Warburg) impedance,  $Z_d$  :

$$Z_f = R_{ct} + Z_d \quad (5)$$

$$Z_d = \frac{R_d}{\sqrt{j\omega}} \quad (6)$$

with  $R_d$  being the diffusion resistance and  $\omega$  the angular frequency.

$R_e$  is electrolyte resistance. The double layer capacitance at the top of ZnO layer is represented by a constant phase element

$$Z_{CPE} = \frac{1}{Q(j\omega)^\alpha} \quad (7)$$

with  $Q$  and  $\alpha$  being the frequency-independent CPE parameters.

The resistivity,  $\rho$ , of the non-textured ZnO was measured cross-plane (transverse mode) using the same setup as in Chapter 4.  $\rho$  was found to be ca.  $10^2 \Omega \text{ cm}$ , the same order of magnitude as for the textured films. Hence there is no significant influence of the texture (nanostructure) on the resistivity for the films synthesized by rf-magnetron sputtering in this Ph.D. thesis.  $R_{film}$  is estimated to be ca.  $6 \cdot 10^{-3} \Omega \text{ cm}^2$ , which is negligible compared to the values of  $R_{ct}$  and  $R_d$ .

The total simulated impedance,  $Z_{sim}$ , for this model is:

$$Z_{sim} = \frac{1}{\frac{1}{Z_f} + \frac{1}{Z_{ZnO} + Z_{CPE}}} + R_e \quad (8)$$

The fitting process enables to get the values of  $R_d$ ,  $R_{ct}$ ,  $Q_1$ ,  $\beta$ ,  $Q$  and  $\alpha$ . The double layer capacitance,  $C_{dl}$ , is calculated using the Brug formula:

$$C_{dl} = Q^{1/\alpha} R_e^{(1-\alpha)/\alpha} \quad (9)$$



The results of the fitting of the experimental data with the equivalent circuit model is shown in Figure 5.9. After numerical optimization,  $Z_{sim}$  was shown to describe  $Z_{exp}$  very well in the whole frequency range. The obtained fitting parameters are listed in Table 5.2. The value of  $C_{dl}$  that are in the usual range of ca. 10-100  $\mu\text{F}/\text{cm}^2$  for double layer capacitances confirms that the impedance of ZnO is small due to a large capacitance (e.g. a large pore surface). This is consistent with a nanoporous layer with many small pores as observed in the *ex situ* HAADF-STEM analysis (Figure 5.6).

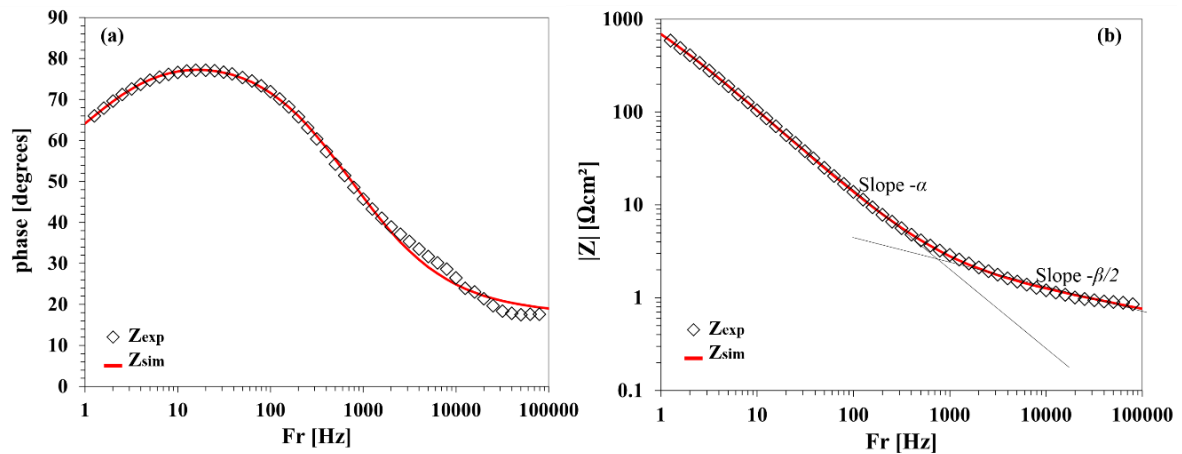


Figure 5.9:  $R_e$ -corrected Bode phase (a) and modulus (b) diagrams obtained at -0.7 V and 200 rpm corrected. The open symbols represent the experimental data ( $Z_{exp}$ ). The line represented the simulated data ( $Z_{sim}$ ) obtained from the fitting process using the equivalent circuit model of Figure 5.8.

$R_e$ ( $\Omega \text{ cm}^2$ )	$R_d$ ( $\Omega \text{ cm}^2$ )	$R_{ct}$ ( $\Omega \text{ cm}^2$ )	$Q_l$	$\beta$	$Q$ ( $\mu\text{F s}^{\alpha-1} \text{ cm}^2$ )	$\alpha$	$C_{dl}$ ( $\mu\text{F cm}^2$ )
11.9	$2 \cdot 10^{+3}$	$1.6 \cdot 10^{+3}$	0.0128	0.44	149	0.89	68

Table 5.2: Results of the fitting process using the model of Figure 5.8.

Figure 5.10 schematically compares textured and non-textured layers in terms of Bode plots of the modulus. The comparison is based on the capacitance values of the ZnO and the double layer. In a first approximation, the capacitance accounts for the surface of the pores in contact with the electrolyte. In the ionic branch of the equivalent circuit,  $Z_{\text{ZnO}}$  and  $Z_{\text{CPE}}$  are in series.



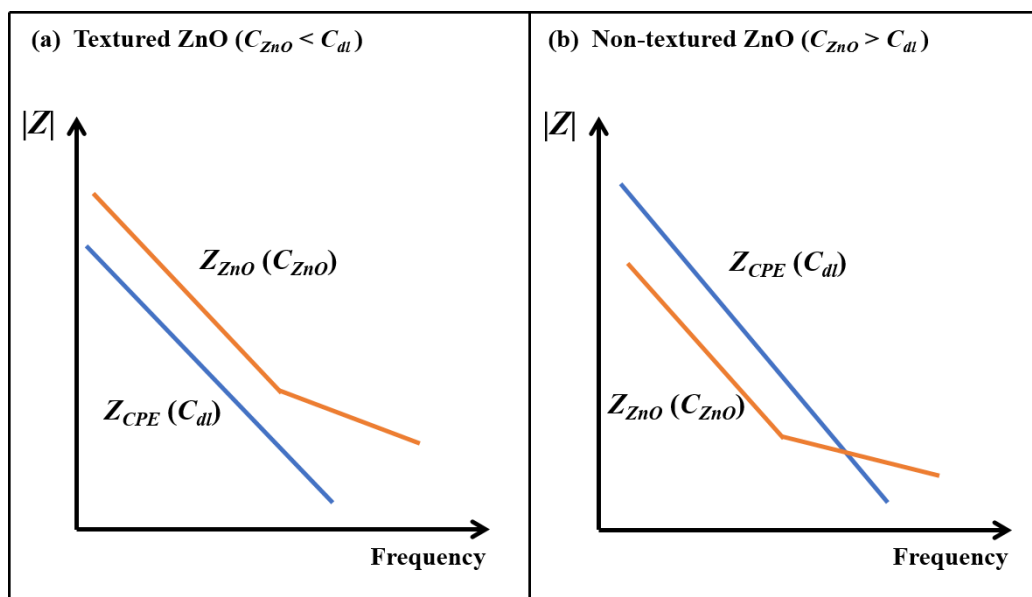


Figure 5.10: Effect of the capacitances of the ZnO and the double layer on the Bode plot of the impedance modulus for (a) textured films (Chapter 4) and (b) non-textured films (this chapter).

As the impedance of such capacitive element is inversely proportional to its capacitance, the impedance of the greater capacitance is masked by the impedance of the smaller capacitance. In the case of textured films (Chapter 4), the small capacitance is generated by localized micro-scaled cracks and the double layer capacitance is not visible. An (almost) identical equivalent circuit is able to describe the opposite situation in the case of non-textured films. The nano-granular structure with numerous nanopores develops a large internal surface area. Hence  $Z_{ZnO}$  is negligible and only the double layer capacitance is measurable.

Please note that the EIS measurements presented above (Figures 5.7-5.9) were carried out right after immersion and during DC polarization. The EIS results ( $C_{ZnO} > C_{dl}$ ) were not affected by the change of surface morphology during DC polarization that is described below. DC investigations under cathodic polarization were performed to gain understanding on the ORR activity and reaction mechanism on the non-textured ZnO layers. Based on the resistivity measurements mentioned above, it is considered that the non-textured ZnO is a good electrical conductor and that the ohmic drop within the layer during DC polarization is negligible.

Systematically, chronoamperometry at  $-0.7$  V with a rotation rate of 200 rpm was carried out as first experiment right after electrode immersion in order to evaluate the electrochemical stability of the films. A typical chronoamperometric curve is shown in Figure 5.11.

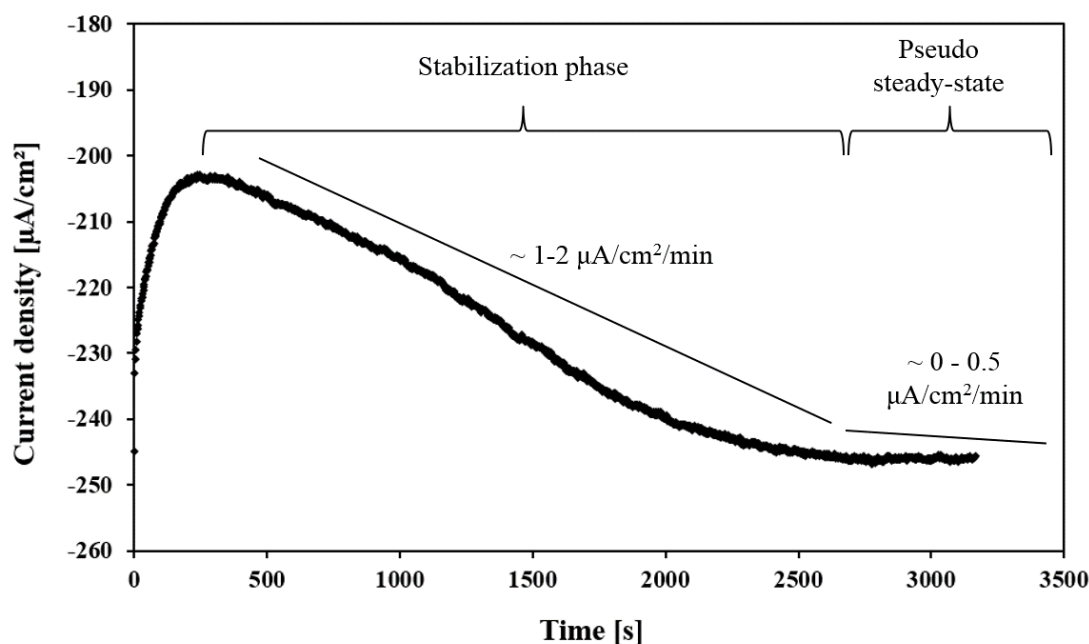


Figure 5.11: Typical chronoamperometry curve of the disk recorded at  $-0.7\text{V}$  and at a rotation rate of 200 rpm.

The potential of  $-0.7\text{ V}$  was chosen because it corresponds to an ORR kinetics controlled by both charge transfer and mass transport. Hence this is one of the potentials at which RRDE measurements could be made (see Figures 5.16 and 5.17 below). At the beginning of the measurement, the current density decreases sharply, which corresponds to the capacitive discharge resulting from applying of the potential step from OCP to  $-0.7\text{ V}$ . Thereafter, the current density increases steadily at a rate of ca.  $1\text{-}2\ \mu\text{A}/\text{cm}^2/\text{min}$  during ca. 40-60 min (depending on the sample). During this period, no reliable analysis of the ORR mechanism can be done since no steady-state conditions are reached. This period is denoted “stabilization phase” in Figure 5.11. Eventually a more stable regime in which the current density is stable or continues to increase very slowly ( $0\text{ - }0.5\ \mu\text{A}/\text{cm}^2/\text{min}$ ). This is described as the “pseudo-steady-state”. Under those conditions, the rapid measurements of disk and ring currents (as described below in Figure 5.16) are considered as reliable. From the beginning to the end of the DC polarization (chronoamperometry + RRDE experiments), the current density increases by 20-50 %, depending on the sample and the duration of polarization

In order to gain more insight on the evolution of the current shown in Figure 5.11, SEM and AFM imaging of the ZnO surface were performed before and after polarization (Figure 5.12). The very positive result was that no rupture of the layers was observed after polarization, (Figure 5.12b). This validated the strategy of synthesizing non-textured layers to

obtain better mechanical stability than in Chapter 3. Thus, the increase of current density observed during the stabilization phase cannot be ascribed to a layer delamination that would expose the electrochemically active copper substrates.

Rather it is associated with the roughening of the surface that is clearly visible on the SEM micrographs as well as on the AFM images (insets). This roughening is due to the development of a large number of nodules.

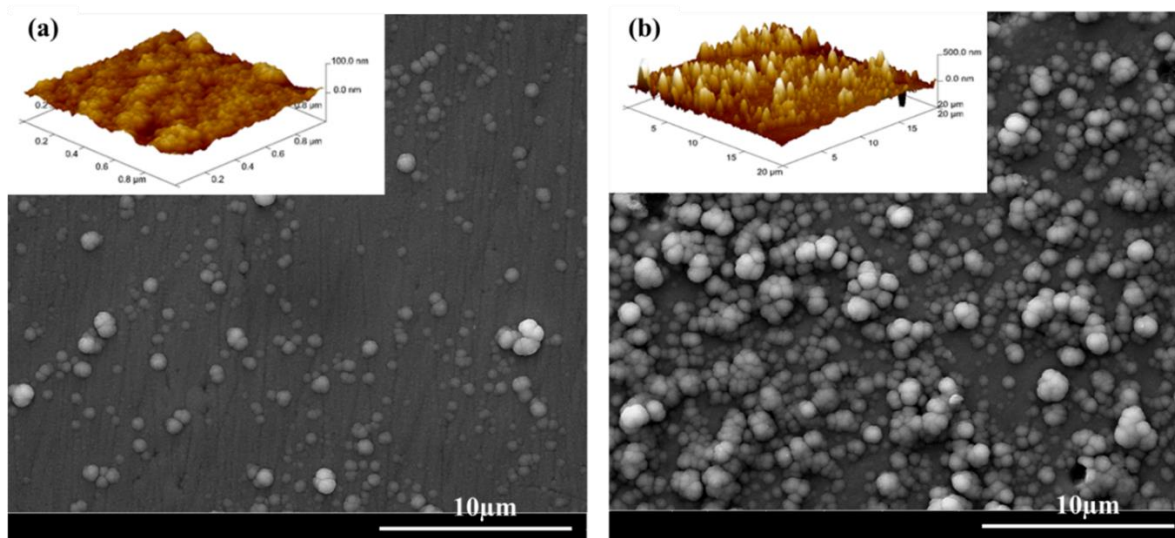


Figure 5.12: SEM top-view micrographs of the non-textured ZnO surface: (a) as-deposited; (b) after electrochemical analysis. Insets: AFM images.

Additional post-mortem analyses were performed to better understand the nodule-rich surface. XRD diffractograms demonstrate that, within the detection limits of the technique, the rough electrodes (after polarization) did not contain any additional crystalline compound (Figure 5.13). EDX spot measurements evidenced that the composition of the base layer remained almost unchanged (50:50 Zn:O). In contrast, the nodules were significantly richer in oxygen (from 44:56 till 36:64 Zn:O) than in the as-deposited state. It might be that amorphous  $\text{Zn}(\text{OH})_2$  developed during cathodic polarization (for instance, during a dissolution-redeposition process).

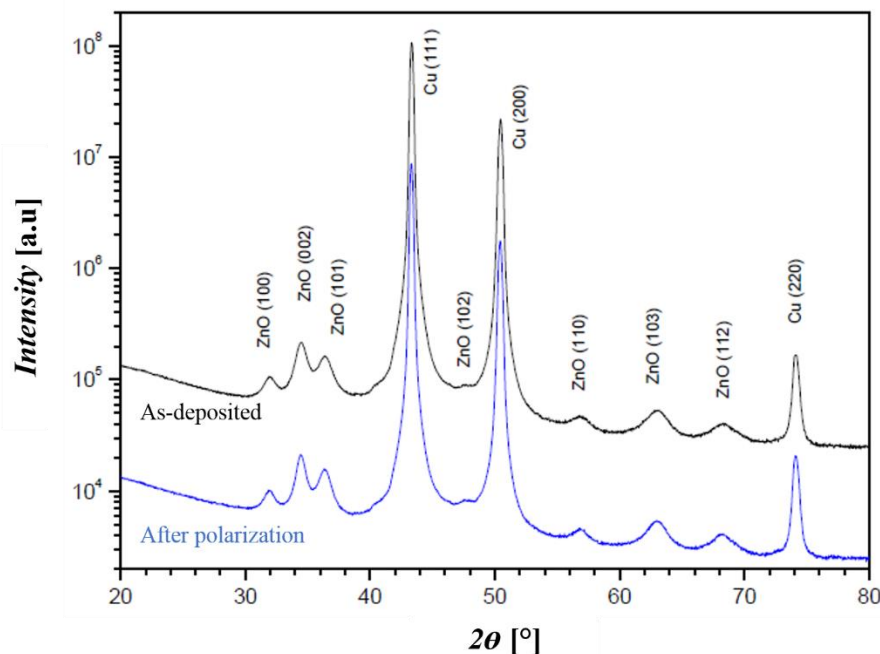


Figure 5.13: XRD diffractograms of non-textured ZnO layer: as-deposited (black curve) and after electrochemical polarization (blue curve).

XPS analysis could not be done to analyze the nodule-rich surface as the sample holder was not compatible with the copper substrate of the layers. More research work is still needed to elucidate the growth mechanism and the chemical nature of the nodules.

The ORR findings presented below are those of rough non-textured ZnO (after the stabilization phase). As the electrochemical techniques used in this thesis provide only “global” information, the results have to be seen as “averaged” properties of the ZnO base layer and the nodules. The cathodic activity of the non-textured ZnO electrodes was evaluated with potentiodynamic voltammetry at low scan rate from the open-circuit to the oxygen reduction plateau at pH = 10 (Figure 5.14). The polarization curves are compared with those of textured ZnO (Chapter 3) and electrodeposited ZnO (from a previous study carried out at the French Corrosion Institute [23]). For the electrodeposited ZnO, the pH was 11 and the supporting electrolyte was more concentrated (KCl 2 M) which explains the low current density of the oxygen diffusion plateau (due to lower oxygen diffusion coefficient). Its microstructure was randomly-oriented. All curves were recorded with the same RDE setup.

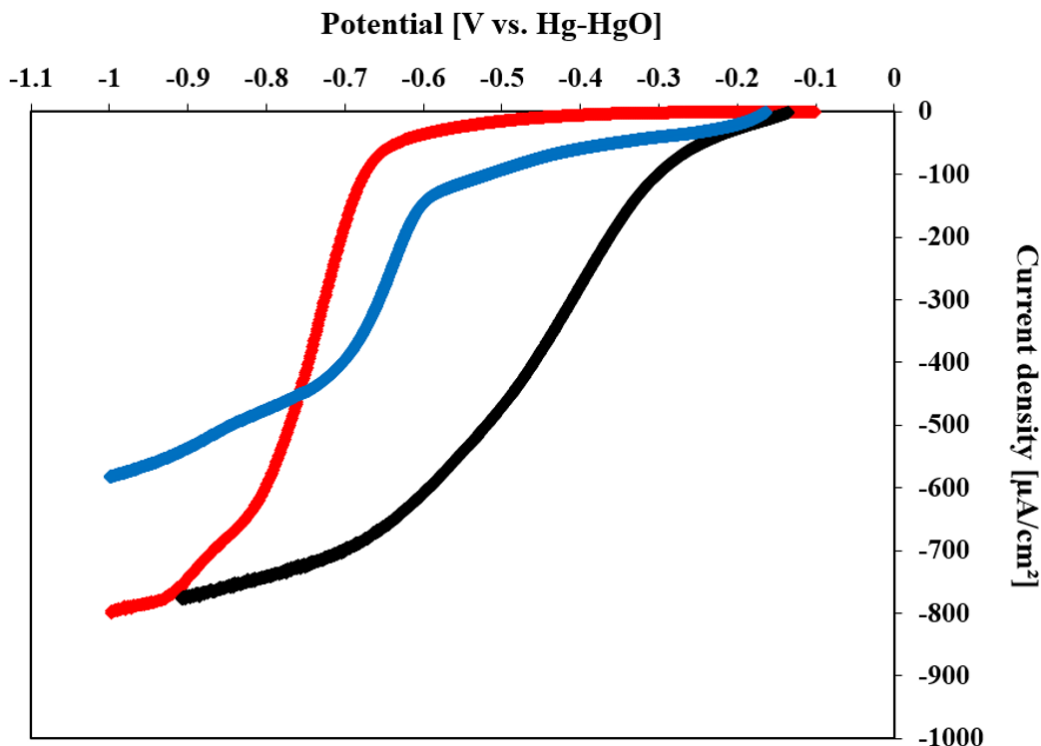


Figure 5.14: Cathodic polarization curves of the non-textured ZnO (black curve) and textured (red curve) ZnO films. The potential scan rates were between 0.5 and 1 mV/s at a rotation rate 1000 rpm. For comparison purposes, the polarization curve of electrodeposited ZnO (blue curve) is also supplied. It was recorded at pH 11 with KCl 2M as supporting electrolyte.

The non-textured ZnO is far more active towards ORR than the textured ZnO and, to a smaller extent, than the electrodeposited ZnO. At -0.5 V, the (modulus of the) current density is 14  $\mu\text{A}/\text{cm}^2$  for the textured ZnO, 93  $\mu\text{A}/\text{cm}^2$  for the electrodeposited ZnO and 470  $\mu\text{A}/\text{cm}^2$  for the non-textured ZnO. Certainly, part of high current density of the non-textured ZnO is due to its rough surface developing more electrode/electrolyte interfacial area. Yet, even by taking this point in to account and by making a correction of 50% (i.e. 235  $\mu\text{A}/\text{cm}^2$ ), the activity of the non-textured ZnO remains significantly higher than that of textured ZnO. The superior activity of non-textured ZnO can also be seen in the smaller overpotentials to reach the onset of the oxygen reduction “wave” occur: ca. 100 mV for the non-textured ZnO compared 450-550 mV for the other films.

The comparison of the three curves shows that ZnO can have very different cathodic behaviors. The ORR activity is likely to depend on the nanostructure which, in turn, is strongly related to the synthesis conditions. Yet no clear and straightforward trend can be established on the sole basis of the three curves of Figure 5.14 along with the very limited data of the literature. For instance, nanogranular ZnO electrodes, like the non-textured layers of this Chapter, the electrodeposited films of Figure 5.14 (blue curve) [23] and the

electrodeposited ZnO from Goux *et al.* (exhibiting sluggish activity and large overpotentials) [24] behave quite differently towards ORR. This opens interesting research topics focusing notably on the complex relationships between electrochemical activity and the numerous parameters that define a ZnO electrode (synthesis method, synthesis parameters, nanostructure, grain size, pore size, influence of grain boundary, surface composition, presence of a second phase...)

In order to quantify the prevalence of the direct or indirect reduction, an ORR mechanism has been proposed (Figure 5.15) and solved analytically. It was adapted from the work of Heller-Ling *et al.* on alkaline ORR at  $\text{Ni}_x\text{Co}_{3-x}\text{O}_4$  spinel films using a double-electrode channel flow cell [25].

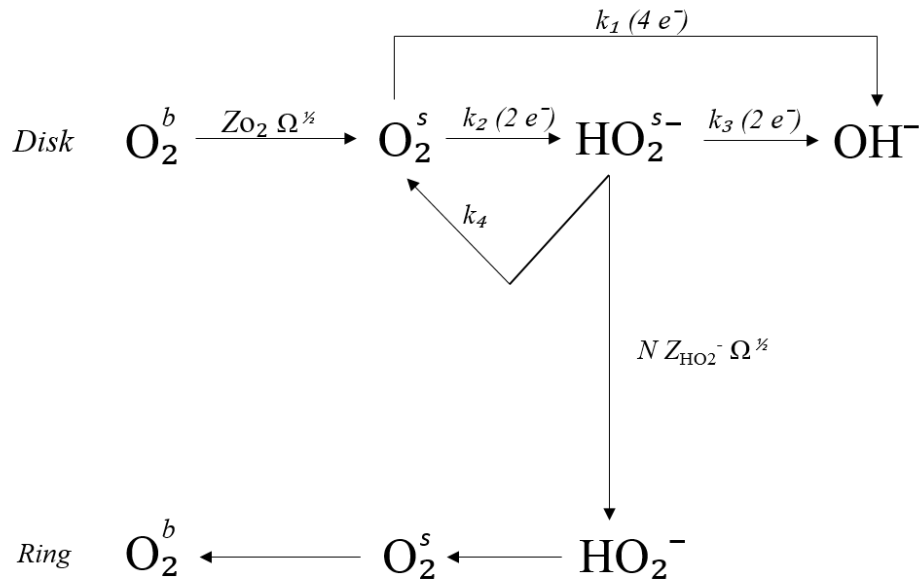
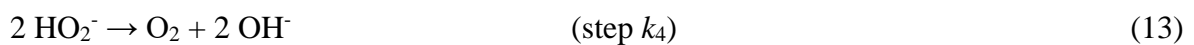
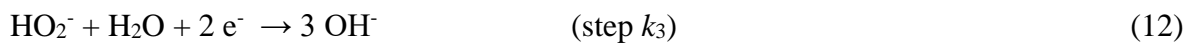
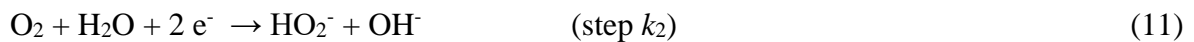


Figure 5.15: Alkaline oxygen reduction reaction model. The superscripts <sup>b</sup> and <sup>s</sup> mean “species in the bulk of the electrolyte” and “species near the disk surface, respectively”.

The detailed (electro)chemical reactions of the model are:



with  $k_1$ ,  $k_2$ ,  $k_3$  and  $k_4$  being the rate constants associated to each reaction steps.

The model is based on the magnitude of the disk current,  $I_d$ , and ring current,  $I_r$ . For sake of simplification, all currents are considered in terms of modulus. Hence the negative sign of oxygen reduction current (disk current) is ignored.

The assumptions and approximations were made:

- The oxygen reduction takes place at the surface of the electrode and not in the pores of the layers (as schematically depicted in Figure 5.1c). In view of the HAADF-STEM results, this approximation is realistic.
- The measurements of the disk and ring current are carried out under steady-state conditions. In practice, they were performed under “pseudo-steady-state” conditions after the stabilization phase (see Figure 5.11). The swiftness of the measurement (typically one minute, see Figure 5.16) make possible reliable measurements of the disk and ring current by considering they are stable during this short period of time. Note that this was not the case during the stabilization phase.
- The RRDE theory have been developed for smooth disk electrodes. In this study, it is approximated that it also applies to “moderately rough” electrodes like those described in Figure 6.12b. The reasonable nature of this approximation is also supported by the fact the determination of the  $\frac{N_d}{I_r}$  ratio is not affected by disk surface area (see Eq. (24) below).

According to the reaction model of Figure 5.15, the disk current,  $I_d$ , can be written as follows:

$$I_d = 4FSk_1C_{O_2}^s + 2FSk_2C_{O_2}^s + 2FSk_3C_{HO_2^-}^s \quad (14)$$

with  $F$  being the Faraday,  $S$  the active surface area of the electrode,  $C_{O_2}^s$  the oxygen concentration near the electrode surface and  $C_{HO_2^-}^s$  the hydrogen peroxide concentration near the electrode surface.

Under steady-state conditions, the reaction and transport fluxes generating and consuming  $O_2$  and  $HO_2^-$  near the surface of the disk are equal, hence:

$$(k_1 + k_2)C_{O_2}^s = k_4C_{HO_2^-}^s + Z_{O_2}\Omega^{1/2}C_{O_2}^b \quad (15)$$

$$k_2C_{O_2}^s = (k_3 + k_4 + Z_{HO_2^-}\Omega^{1/2})C_{HO_2^-}^s \quad (16)$$

with:

$$Z_{O_2} = 0.201 \nu^{-1/6} D_{O_2}^{2/3} \quad (17)$$

$$Z_{HO_2^-} = 0.201 \nu^{-1/6} D_{HO_2^-}^{2/3} \quad (18)$$

with  $\Omega$  being the electrode rotation rate,  $\nu$  the kinematic viscosity of the electrolyte,  $Z_{O_2}$  and  $Z_{HO_2^-}$  the diffusion-convection rate constant of oxygen and hydrogen peroxide (respectively), and  $D_{O_2}$  and  $D_{HO_2^-}$  the diffusion coefficient constant of oxygen and hydrogen peroxide (respectively).

By combining Eq. (15) and Eq. (16), the concentration of the species at the disk surface,  $C_{O_2}^s$  and  $C_{HO_2^-}^s$ , can be calculated as a function of all the kinetic and transport parameters of the reaction model:

$$C_{O_2}^s = \frac{A Z_{O_2} \Omega^{1/2} C_{O_2}^b}{A(k_1 + k_2) - k_4} \quad (19)$$

$$C_{HO_2^-}^s = \frac{Z_{HO_2^-} \Omega^{1/2} C_{O_2}^b}{A(k_1 + k_2) - k_4} \quad (20)$$

with,

$$A = \frac{k_3 + k_4 + Z_{HO_2^-} \Omega^{1/2}}{k_2} \quad (21)$$

By implementing Eq. (19) and Eq. (20) in Eq. (14), one obtains the dependence of the disk current,  $I_d$ , on the reaction model rate constants and the rotation rate  $\Omega$ :

$$I_d = \frac{2FSZ_{O_2} \Omega^{1/2} C_{O_2}^b}{A(k_1 + k_2) - k_4} \{A(2k_1 + k_2) + k_3\} \quad (22)$$

The ring current,  $I_r$ , can be expressed as:

$$I_r = 2NFSZ_{HO_2^-} \Omega^{1/2} C_{HO_2^-}^s \quad (23)$$



with  $N$  being the collection coefficient of the RRDE ( $N = 23\%$ ). By combining Eqs. (20), (21), (22) and (23), one gets the following equation:

$$\frac{NI_d}{I_r} = \left( \frac{2k_1}{k_2} + 1 \right) + \frac{1}{Z_{\text{HO}_2} \cdot \Omega^{1/2}} \left\{ \frac{2k_1}{k_2} (k_3 + k_4) + 2k_3 + k_4 \right\} \quad (24)$$

If the model applies, plotting  $\frac{NI_d}{I_r}$  as a function of  $\Omega^{-1/2}$  leads to a straight line whose intercept on the vertical axis (*i.e.* at infinite rotation rate) yields  $\frac{2k_1}{k_2} + 1$  from which the ratio  $\frac{k_1}{k_2}$  can be derived. From a kinetic point of view, the extrapolation to infinite rotation rate allows to simplify the reaction kinetics by “ignoring” the steps  $k_3$  and  $k_4$ . It is important to note that the determination of  $\frac{k_1}{k_2}$  is independent of the surface area of the electrode. Hence, in first approximation, it can be applied to the rough electrodes observed in Figure 5.12b.

Typical experimental RRDE data is presented in Figure 5.16. The disk and ring current are recorded under pseudo-steady-state conditions at fixed potential while varying the rotation rates. Proceeding this way (rather than recording several polarization curves at various rotation rates as commonly done) allows for fast acquisition of the currents which is particularly useful when the electrode is not fully stable. The fixed potential also enables to avoid any capacitive (non-faradaic) effects that may originate from potentiodynamic measurements. The selected rotation rates varied from one sample to another but remain in the range of 40 - 600 rpm. In Figure 5.16,  $I_r$  is divided by the collection efficiency  $N$  (23%). It represents the ring current that would be generated if this efficiency was 100%.

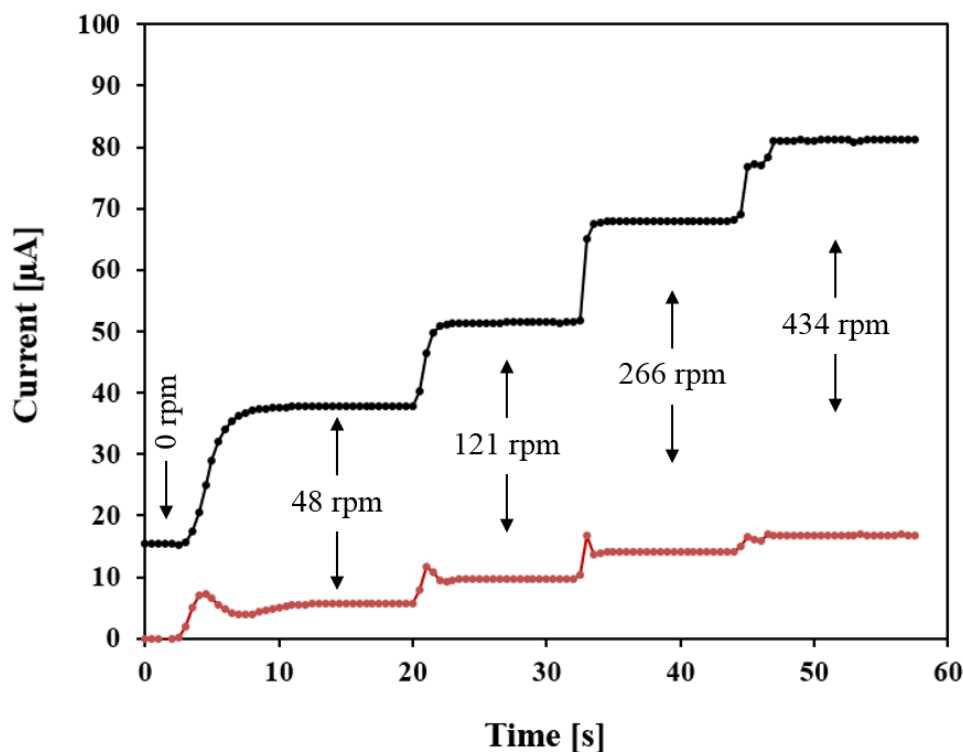


Figure 5.16: Typical experimental RRDE currents obtained at fixed potential (here at -0.9 V) while varying the rotation rate. The currents were recorded at the end of each plateau. The black curve corresponds to the disk current,  $I_d$ , and the red curve shows the ring current divided by the collection efficiency,  $I_r/N$ .

The  $\frac{N I_d}{I_r}$  vs.  $\Omega^{1/2}$  plots for several non-textured ZnO films at -0.7 V and -0.9 V are shown in Figure 5.17. The good linear regressions validated the proposed model and its assumptions and approximations. Although there is some scattering in the results, the intercepts on the y-axis led to rather reproducible values. The ratio  $\frac{k_1}{k_2}$  was 1.1 to 1.6 at -0.7 V and 1.3 to 2.2 at -0.9 V. Thus, there is a slight prevalence of the direct oxygen reduction (pathway  $k_1$ ). The results indicate that both the direct and indirect pathways contribute to the reduction of oxygen and none of them can be neglected. A similar conclusion was reached for the textured ZnO (yet for a lower ORR activity) in Chapter 3 but with no possibility of quantitatively establishing the prevalence of one or the other pathway.

In the reports of the literature about ORR investigated on zinc with the RRDE technique, a clear trend is that the reaction mechanism was potential-dependent (in alkaline and near-neutral electrolytes) [26,27]. On passive zinc (*i.e.* covered by a few nanometers of ZnO) and low cathodic overpotentials, a two-electron reaction was found, producing only hydrogen peroxide (no direct reduction). This corresponds to the step  $k_2$  of our reaction mechanism. With increasing negative potentials, the contribution of the direct reduction (step

$k_1$ ) increases until it becomes the unique reaction (with no hydrogen peroxide produced). This “switch” of reaction mechanism is associated with the passive-active transition of the zinc surface when the potential goes more negative, as described by Flitt *et al.* [28]. Thus it appears that the “thick” ZnO films of this Ph.D. thesis behave quite differently with both the production of OH<sup>-</sup> (step  $k_1$ ) and hydrogen peroxide (step  $k_2$ ) even far from the equilibrium potentials.

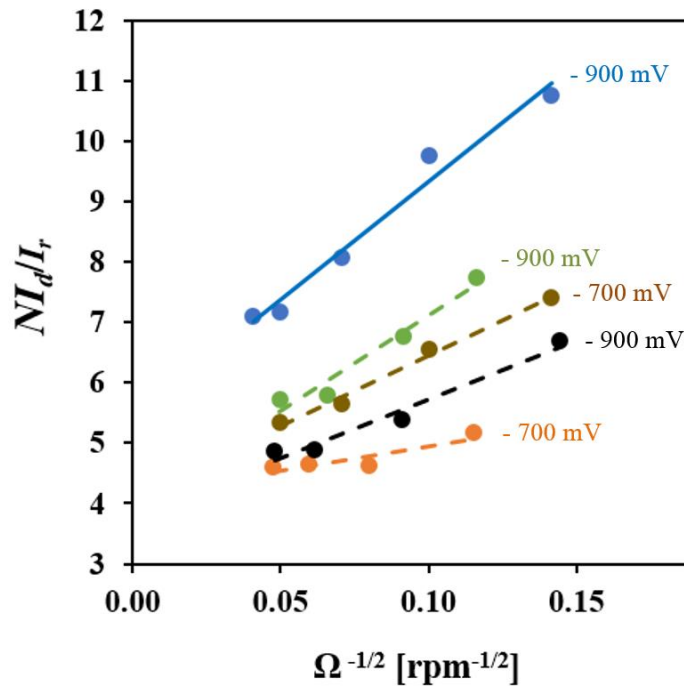


Figure 5.17:  $\frac{NI_d}{I_r}$  vs.  $\Omega^{-1/2}$  plots obtained for several non-textured ZnO layers at -700 mV and -900 mV.

Once the ratio  $\frac{k_1}{k_2}$  is established, the next question to answer is: what happens to the hydrogen peroxide ions? According to the reaction model (Figure 5.15), the following scenarios are possible:

- (1) The indirect reduction reaction proceeds no further. This means  $k_3 = k_4 = 0$ .
- (2) HO<sub>2</sub><sup>-</sup> is reduced to OH<sup>-</sup> (step  $k_3$ ).
- (3) HO<sub>2</sub><sup>-</sup> is chemically decomposed into O<sub>2</sub> (step  $k_4$ , this reaction is also named disproportionation).
- (4) HO<sub>2</sub><sup>-</sup> is partially reduced (step  $k_3$ ) and partially decomposed (step  $k_4$ ) simultaneously.

These four scenarios are, in principle, distinguishable based on the values of  $I_r/N$  and  $n$ , the mean number of exchanged electrons per reduced oxygen molecule ( $2 \leq n \leq 4$ ). In theory, it is possible to evaluate  $n$  using the Koutecky-Levich equation [29]:

$$\frac{1}{I_d} = \frac{1}{I_k} + \frac{1}{0.201 n S F C_{O_2}^b D_{O_2}^{2/3} \nu^{-1/6} \Omega^{1/2}} \quad (25)$$

with  $I_k$  being the kinetic current (in absence of mass transport limitations) and  $S$  the active electrolyte/electrolyte interface area.

Plotting  $\frac{1}{I_d}$  vs.  $\Omega^{-1/2}$  yields a straight line whose slope enables to calculate  $n$  provided that  $S$  is known:

$$n = \frac{1}{0.201 S F C_{O_2}^b D_{O_2}^{2/3} \nu^{-1/6} \text{slope}} \quad (26)$$

For a plane electrode,  $S$  is taken as the geometrical area of the disk (in our case, 0.196 cm<sup>2</sup> for a disk with a diameter of 5 mm). Yet using the geometrical surface area for a rough electrode in Eq. (25) leads to an underestimation of  $S$  and an overestimation of  $n$ . Since accurate values of  $S$  was not known while doing the RRDE measurements of the non-textured ZnO layers, the Koutecky-Levich equation could not be applied in a reliable way.

Exploiting the values of  $I_r/N$  provides some interesting insight regarding the occurrence of scenario (1). From Eq. (24), it can be stated that, if  $k_3$  and  $k_4$  are much smaller than  $Z_{HO_2} \cdot \Omega^{1/2}$ , then:

$$\frac{NI_d}{I_r} = \frac{2k_1}{k_2} + 1 \quad (27)$$

Expressed differently, if scenario (1) is valid, then:

$$\frac{I_r}{N} = \frac{I_d}{\frac{2k_1}{k_2} + 1} \quad (28)$$

Figure 5.18 compares  $I_r/N$  with  $\frac{I_d}{\frac{2k_1}{k_2} + 1}$  derived from the data of Figure 5.16 that is well representative of the samples investigated with RRDE.  $\frac{2k_1}{k_2} + 1$  was equal to 3.8.  $I_r/N$  is smaller than  $\frac{I_d}{\frac{2k_1}{k_2} + 1}$  at all rotation rates.

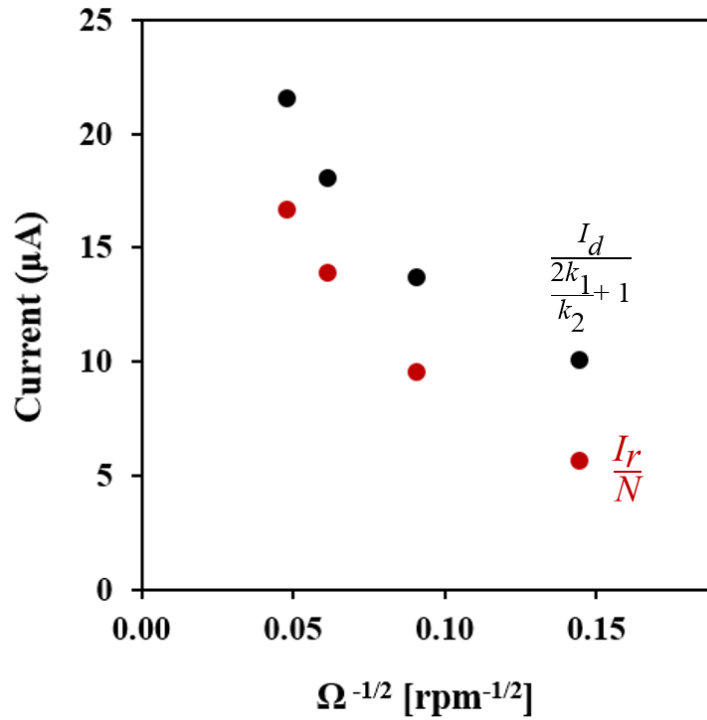


Figure 5.18: Comparison of  $I_r/N$  with  $\frac{I_d}{\frac{2k_1}{k_2} + 1}$  at different rotation rates.

There is thus a deficit of current collected at the ring. This means that part of the hydrogen peroxide produced by the step  $k_2$  is consumed by the step(s)  $k_3$  and/or  $k_4$  and does not reach the ring. Scenario (1) is therefore not valid. Yet without the value of  $n$ , it is not possible to identify which reaction steps are active ( $k_3$ ,  $k_4$  and or the combination of both). From the values of  $\frac{k_1}{k_2}$ , one can only state that  $n$  is greater than 3 (for equal contributions of direct and indirect reduction ( $k_1 = k_2$ ),  $n$  would have been equal to 3).

#### 5.4. Conclusions

In this chapter, 600-800 nm thin non-textured ZnO films were successfully produced by rf-magnetron sputtering. The nano-granular structure was verified by XRD, AFM and SEM. EIS analysis using a model based on the DeLevie impedance supplied *in situ* evidence

of the porosity of the layers. HAADF-STEM imaging demonstrated that pore size and grain size was *ca.* 10 nm. The narrowness of the pores enabled to consider that oxygen reduction took place at the surface of the layers. Under DC polarization, the non-textured ZnO films proved to be mechanically stable and did not suffer from the rupturing problems of the textured layers. Yet they developed a certain roughness due to the presence of numerous nodules that were more zinc-depleted and richer in oxygen than the nominal ZnO composition. Compared to the columnar films of Chapter 3, the non-textured ZnO electrodes exhibit a significantly higher cathodic activity. This proves that there is not a single type of ZnO behavior towards ORR. Electrochemical activity probably depends on many parameters such synthesis method and conditions, nanostructure, pore and grain size, among others.

A reaction mechanism was proposed for oxygen reduction. Using experimental data collected with the RRDE technique, it made possible the assessment of the ratio  $\frac{k_1}{k_2}$  (direct over indirect reduction). The direct reduction was shown to be dominant, but the indirect reduction could not be neglected. The roughness of the electrode impeded the determination of the mean number of exchanged electrons using the Koutecky-Levich equation. Yet it was possible to evaluate that indirect reduction pathway did not stop at the production of hydrogen peroxide. The latter is further reduced to OH<sup>-</sup> anions and/or decomposed into oxygen molecules.

### 5.5. References

- [1] W. Gao, Z. Li, ZnO thin films produced by magnetron sputtering, *Ceramics International* 30 (2004) 1155–1159;
- [2] H.-Y. Tsai, Characteristics of ZnO thin film deposited by ion beam sputter, *Journal of Materials Processing Technology* 192–193 (2007) 55–59;
- [3] S.-Y. Chu, W. Water, J.-T. Liaw, Influence of postdeposition annealing on the properties of ZnO films prepared by RF magnetron sputtering, *Journal of the European Ceramic Society* 23 (2003) 1593–1598;
- [4] R. E. I. Schropp, A. Madan, Properties of conductive zinc oxide films for transparent electrode applications prepared by rf magnetron sputtering, *Journal of Applied Physics* 66, 2027 (1989);
- [5] Z. Onuk, N. Rujisamphan, R. Murray, M. Bah, M. Tomakin, S. I. Shah, Controllable growth and characterization of highly aligned ZnO nanocolumnar thin films, *Applied Surface Science* 396 (2017) 1458–1465;

- [6] I. Sayago, M. Aleixandre, L. Arés, M. J. Fernández, J. P. Santos, J. Gutiérrez, M. C. Horrillo, The effect of the oxygen concentration and the rf power on the zinc oxide films properties deposited by magnetron sputtering, *Applied Surface Science* 245 (2005) 273–280;
- [7] K. Srinivasarao, Ch. Prameela, P. Venkata Kala, P. K. Mukhopadhyay, Preparation and Characterization of rf. magnetron sputtered porous ZnO thin films, *Materials Today: Proceedings* 2 (2015) 4503 – 4508;
- [8] H. S. Al-Salman, M. J. Abdullah, Preparation of ZnO nanostructures by RF-magnetron sputtering on thermally oxidized porous silicon substrate for VOC sensing application, *Measurement* 59 (2015) 248–257;
- [9] C. Shang, Y. Thimont, A. Barnabé, L. Presmanes, I. Pasquet, P. Tailhades, Detailed microstructure analysis of as-deposited and etched porous ZnO films, *Applied Surface Science* 344 (2015) 242–248;
- [10] M. A. Mahdi, A. Ramizy, H. F. Al-Taay, Preparation and characterization of porous ZnO nanostructures grown onto silicon substrate, *Journal of Ovonic Research* 13 (2017) 135 – 141;
- [11] Z. W. Li, W. Gao, R. J. Reeves, Zinc oxide films by thermal oxidation of zinc thin films, *Surface & Coatings Technology* 198 (2005) 319– 323;
- [12] M. A. Borysiewicz, E. Dynowska, V. Kolkovsky, J. Dyczewski, M. Wielgus, E. Kaminska, A. Piotrowska, From porous to dense thin ZnO films through reactive DC sputter deposition onto Si (100) substrates, *Phys. Status Solidi A*, (2012) 1–7;
- [13] A. Sacco, A. Lamberti, R. Gazia, S. Bianco, D. Manfredi, N. Shahzad, F. Cappelluti, S. Ma, E. Tresso, High efficiency Dye-sensitized Solar Cell exploiting sponge-like ZnO Nanostructures, *Physical Chemistry Chemical Physics* (2012);
- [14] R. Gazia, A. Chiodoni, S. Bianco, A. Lamberti, M. Quaglio, A. Sacco, E. Tresso, P. Mandracci, C. F. Pirri, An easy method for the room-temperature growth of spongelike nanostructured Zn films as initial step for the fabrication of nanostructured ZnO, *Thin Solid Films* 524 (2012) 107–112;
- [15] M. A. Borysiewicz, E. Dynowska, V. Kolkovsky, M. Wielgus, K. Golaszewska, E. Kaminska, M. Ekielski, P. Struk, T. Pustelny, A. Piotrowska, Sputter deposited ZnO porous films for sensing applications, *Mater. Res. Soc. Symp. Proc.* 1494 (2013);
- [16] V. V. Sasi, A. Iqbal, K. Chaik, A. Iacopi, F. Mohd-Yasin, RF Sputtering, Post-Annealing Treatment and Characterizations of ZnO (002) Thin Films on 3C-SiC (111)/Si (111) Substrates, *Micromachines* 8 (2017) 148;

- [17] B. Abdallah, A. K. Jazmati, R. Refaai, Oxygen Effect on Structural and Optical Properties of ZnO Thin Films Deposited by RF Magnetron Sputtering, *Materials Research*. 20 (2017) 607-612;
- [18] M. Maslyk, M. A. Borysiewicz, M. Wzorek, T. Wojciechowski, M. Kwoka, E. Kaminska, Influence of absolute argon and oxygen flow values at a constant ratio on the growth of Zn/ZnO nanostructures obtained by DC reactive magnetron sputtering, *Applied Surface Science* 389 (2016) 287–293;
- [19] T. Barres, B. Tribollet, O. Stephan, H. Montigaud, M. Boinet, Y. Cohin, Characterization of the porosity of silicon nitride thin layers by Electrochemical Impedance Spectroscopy, *Electrochimica Acta*, 227 (2017) 1-6;
- [20] T. T. M Tran, B. Tribollet, E. M. M Sutter, New insights into the cathodic dissolution of aluminium using electrochemical methods, *Electrochimica Acta*, 216 (2016) 58-67;
- [21] F. Huang, Z. Lin, W. Lin, J. Zhang, K. Ding, Y. Wang, Q. Zheng, Z. Zhan, F. Yan, D. Chen, P. Lv, X. Wang, Research progress in ZnO single-crystal: growth, scientific understanding, and device applications, *Chin. Sci. Bull.* 59 (2014) 1235–1250;
- [22] J. Wang, Z. Wang, B. Huang, Y. Ma, Y. Liu, X. Qin, X. Zhang, Y. Dai, Oxygen Vacancy Induced Band-Gap Narrowing and Enhanced Visible Light Photocatalytic Activity of ZnO, *ACS Applied Materials & Interfaces* 2012;
- [23] M. Prestat, F. Vucko, B. Lescop, S. Rioual, F. Peltier, D. Thierry, Oxygen reduction at electrodeposited ZnO layers in alkaline solution, *Electrochimica Acta* 218 (2016) 228-236;
- [24] A. Goux, T. Pauporte, D. Lincot, Oxygen reduction reaction on electrodeposited zinc oxide electrodes in KCl solution at 70°C, *Electrochimica Acta*, 51 (2006) 3168–3172;
- [25] N. Heller-Ling, M. Prestat, J. L. Gautier, J. F. Koenig, G. Poillerat, P. Chartier, Oxygen electroreduction mechanism at thin  $\text{Ni}_x\text{Co}_{3-x}\text{O}_4$  spinel films in a double channel electrode flow cell (DCEFC), *Electrochimica Acta* 42 (1997) 197-202;
- [26] H. S. Wroblowa, S. B. Qaderi, The mechanism of oxygen reduction on zinc, *Journal of Electroanalytical Chemistry and Interfacial Electrochemistry*, 295 (1990) 153-161;
- [27] A. P. Yadav, A. Nishikata, T. Tsuru, Oxygen reduction mechanism on corroded zinc, *Journal of Electroanalytical Chemistry* 585 (2005) 142–149;
- [28] H. J. Flitt, D. P. Schweinsberg, Synthesis, matching and deconstruction of polarization curves for the active corrosion of zinc in aerated near-neutral NaCl solutions, *Corrosion Science* 52 (2010) 1905–1914;
- [29] Available in: <https://www.pineresearch.com/shop/knowledgebase/rotating-electrode-theory/>.



The main goal of this Ph.D. thesis was to investigate the oxygen reduction reaction (ORR) on ZnO electrodes at pH = 10 under controlled hydrodynamic conditions using the rotating ring disk electrode and to gain understanding on the electrochemical activity and the reaction mechanisms. For that purpose, ideally, dense and smooth ZnO layers had to be prepared. Radio-frequency magnetron sputtering was used to synthesize such ZnO layers since this technique allows to produce a large variety of coatings by changing experimental parameters such as target composition, reactive gas composition, gas fluxes and power. Two types of layers were produced: columnar ZnO with (002) orientation (referred to as “textured”) and nano-granular ZnO with no preferred orientation (referred to as “non-textured”). The two types of films were thoroughly characterized. A particular focus was laid on the ex situ and in situ characterization of the structure of those layers at the micro-scale and the nano-scale.

In Chapter 3, 300 nm thin textured ZnO films were deposited using a zinc oxide target. XRD and FIB-SEM measurements clearly that the films grew columnarly perpendicular to the surface. The width of the columns ranged from 40 to 150 nm and no gaps between them could be observed. The (cross-sectional) FIB-SEM and (surface) AFM images, revealed uniform deposition, smooth and dense layers. In the as-deposited state, the textured ZnO layers fulfilled all the requirements for being a model ZnO electrode suitable for RRDE measurements. However, during DC polarization the films tended to rupture rapidly. Furthermore, this degradation occurred in the potential range where RRDE provides its most useful information, i.e. when ORR is controlled, partially or totally, by mass transport. This impeded the in-depth investigation of ORR on the textured layers. The degradation was characterized by large cracks and local delamination (observed in top-view SEM images after DC polarization). This led to an increase of the cathodic current density since the more electrochemically active copper was in contact with the electrolyte. Despite the fast degradation of the layers, two important characteristics of the ORR were identified:

- Textured ZnO was found to have poor ORR activity with large overpotential.
- During RRDE measurements, a non-negligible flux of hydrogen peroxide was detected on the ring, indicating that both direct and indirect reaction pathways are followed.
- With potentiodynamic polarization curves, the rupture potential was estimated to be ca. -600 mV (vs. Hg-HgO, KOH 1M). This rough estimate was refined in the next thesis chapter with AC analysis.

In Chapter 4, the textured layers were investigated using in situ electrochemical impedance spectroscopy (EIS) and ex situ electron microscopy to document the degradation of the layers. This study took advantage of the fact that EIS could be applied at low overpotentials before large damages appeared on the layers. At the nanoscale, the as-deposited ZnO layers were shown to be compact based on cross-sectional HAADF-STEM imaging. The electrical resistivity of the layers measured in transverse mode was found to be low. The electrolyte resistance corrected Bode plots exhibited a decrease of phase and modulus at high frequencies. Based on those observations, an equivalent circuit model was developed including a De Levie impedance to account for the propagation of the cracks under DC polarization. The penetration of electrolyte in the expanding cracks generated a capacitance,  $C_{\text{ZnO}}$ , that was considered as proportional to the crack inner surface. The main findings of this chapter were:

- $C_{\text{ZnO}}$  is sufficiently small (around  $1 \mu\text{F}/\text{cm}^2$ ) so that its impedance is not masked by that of the double layer capacitance connected in series. This small value of  $C_{\text{ZnO}}$  is consistent with a localized crack propagation observed at the microscale with SEM.
- The gradual increase of  $C_{\text{ZnO}}$  with the applied potential suggests that the development of the cracks is related to the piezoelectric nature of the (002)-oriented ZnO. It also evidenced that crack propagation occurred already at potential as low as -0.3 V (vs. Hg-HgO, KOH 1M).
- The De Levie impedance can be successfully applied to "real" electrodes whose microstructures are far from an ideal arrangement of parallel cylindrical pores. This flexibility of the De Levie impedance was also utilized in Chapter 5 for nanoporous layers.

Based on the results of Chapters 3 and 4 suggesting the mechanical instability of the textured layers was related to their columnar structure, the investigations of Chapter 5 were done on non-textured films. The rationale for this study was twofold:

- Avoiding the rupturing of the layers observed in the previous chapters so that an in-depth RRDE analysis could be performed.
- Producing another type of sputtered ZnO with a different texture/nanostructure so that comparisons could be made with the textured layers, notably in terms of electrochemical properties.

The 600-800 nm thin non-textured films were produced using a zinc target. The flux oxygen in the deposition chamber was increased (while keeping the flux of argon constant) until a nano-granular structure with narrow pores was obtained. The layers were checked to have no rupturing problems by applying a fixed polarization at -0.7 V (vs. Hg-HgO, KOH 1M) for at least 45 min. The main findings of this chapter were:

- $C_{\text{ZnO}}$  is larger than the double layer capacitance so that only the latter could be measured. This large value of  $C_{\text{ZnO}}$  provided an in situ hint of the nanoporosity of the non-textured films that was confirmed by HAADF-STEM imaging. The pores (< 10-15 nm) were considered to be small enough so that ORR takes place at the surface of the layer.
- During DC polarization, the surface of the layers became rougher with the development of oxygen-rich nodules.
- Non-textured ZnO exhibited ORR activity with low overpotential.
- The prevalence of the direct oxygen reduction was quantitatively established ( $k_1/k_2 \sim 1.1 - 2.2$ ) by using a reaction model whose equations could be treated analytically. Yet due to the uncontrolled development of the surface roughness, the mean number of exchanged electron per reduced oxygen molecule could not be established.

When comparing the textured and non-textured layers of this thesis, the following conclusions can be drawn:

- The mechanical instability of the textured layers is postulated to relate to the piezoelectric properties of the (002)-oriented structure. Three findings support this hypothesis. The rupture of films is clearly potential-dependent (Chapter 3). The gradual increase of  $C_{\text{ZnO}}$  with the applied potential (Chapter 4) is also consistent with a piezo-electric behavior. Finally, there is no rupturing when the ZnO layers have a nano-granular structure (Chapter 5).
- In terms of ORR mechanism, both textured and non-textured layer produced hydrogen peroxide (Chapters 3 and 5). For the non-textured samples, the duality of reaction pathways is even quantified since it was possible to evaluate the ratio  $k_1/k_2$  (Chapter 5). It was demonstrated that direct reduction prevails but the indirect pathway with hydrogen peroxide production is not negligible. As mentioned in the state-of-the-art, some first results on that prevalence of direct reduction had been reported on “thick” electrodeposited ZnO layers [1,2]. It differs from the behavior of ultrathin native ZnO layers on zinc for which a two-electron indirect reduction was reported [3-4].
- While the two types of layers have some common points in terms of reaction pathways, their electrochemical activity differ significantly. Non-textured ZnO exhibit a much higher activity than columnar ZnO. When combined with the findings on electrodeposited ZnO [1,2], those results illustrate the fact that the ORR activity depends on the nanostructure, the synthesis methods and probably other experimental factors in a complex way that still has to be elucidated.

Regarding the methodologies utilized in this Ph.D. thesis, critical assessments can be made:

- The choice of rf-magnetron sputtering for synthesizing model layers suitable for RRDE measurements was validated. Though the sputtering setup is a shared facility in the Lab-STICC, Brest, which limited the number of produced samples, different textures and nanostructures could be obtained by varying the deposition parameters. It was the lack of stability of the layers under polarization that constituted the main issue of this Ph.D. thesis. Cracked appeared in the textured layers under DC polarization (Chapters 3 and 4) while the development of nodules brought about the surface roughening of the non-textured layers (Chapter 5). Whether those problems were specific to rf-magnetron sputtering is difficult to evaluate. To answer this question,

other thin film deposition methods should be used, such as electrodeposition, sol-gel, pulsed laser deposition and spray pyrolysis.

- EIS proved to be a powerful tool to evidence in situ the porosity of the layers. As the two type of ZnO had a good electrical conductivity, the DeLevie impedance could be used to account for the penetration of the electrolyte in the pores. The relatively simple equivalent circuit model could describe two very different kinds of porosity: localized microscaled cracks (textured ZnO, Chapter 4) and homogenously distributed nanoscaled pores (non-textured ZnO, Chapter 5). In the case of the textured layers, EIS made possible the detection of the early stages of the crack propagation occurring at low overpotentials at which post-mortem SEM top-view micrographs were useless (no apparent delamination or large cracks). EIS provided thus a cost-effective and relatively quick way to gain in situ information about layer porosity. The EIS data were complementary to the valuable ex situ information obtained by high-resolution electron microscopy techniques, like HAADF-STEM, that are more difficult to set up, more expensive and applicable to a limited number of samples. In the field of corrosion, the methodology combining EIS and advanced electron microscopy methods could also be applied to investigate the barrier properties of other conductive coatings that may develop porosity during operation, such as Zn-Fe or Zn-Ni alloys [5].
- Once mechanically stable layers were produced, RRDE experiments combined with reaction modelling provided useful insight on the reaction mechanism, namely the ratio  $k_1/k_2$  (Chapter 5). In DC measurement, only collection-based electrochemical techniques, such as RRDE and double electrode channel flow cell [6-7], can offer such direct way to evaluate the competition between the direct and indirect pathways of oxygen reduction. In the present study,  $k_1/k_2$  was conveniently obtained by extrapolation at infinite rotation rate, which is like virtually switching off all the other reactions steps of the model ( $k_3$  and  $k_4$ ). Other details of the reaction mechanism, like the relevance of the chemical decomposition of hydrogen peroxide and/or its reduction to  $\text{OH}^-$  anions could have been evaluated if the textured ZnO layers would not have become rough during polarization.

While this thesis has supplied insights on the ORR reaction mechanism and kinetics on ZnO in alkaline conditions, it has also raised new questions that can be the basis for additional research activities.

The chemical nature and the electrochemical activity of the oxygen-rich nodules visible on the surface of the non-textured ZnO films could not be clarified (Chapter 5). As the RRDE method provides only a “global” information, the electrochemical properties of the layers are an average of the base layer (~ ZnO) and the oxygen-rich nodules. Hence local probe techniques, like the scanning electrochemical microscope, could help evidence a potential difference of activity between base layer and nodules and also gain information on the growth mechanism of the nodules. Complementary analyses using selective area electron diffraction (SAED), Raman spectroscopy, XPS, STEM-EDX would be needed to assess the degree of crystallinity of the nodules and their chemical composition (ZnO? Zn(OH)<sub>2</sub>? other phases?).

In Chapter 5, it was also clearly shown that the electrochemical activity towards ORR of three types of ZnO films (sputtered textured, sputtered non-textured and electrodeposited non-textured) exhibited significantly different cathodic polarization curves (see Figure 5.14). This suggests that there is no such thing as a single ZnO behavior as far as oxygen reduction is concerned. Outside the framework of this Ph.D. thesis that focuses on sputtered electrodes, it is most likely that ORR activity varies from one type of ZnO to another. As shown in the analysis of the state-of-the-art (Chapter 1), there is limited data on ORR at ZnO films reported in the literature. To the best of our knowledge, no study on the relationships between synthesis, nanostructure and ORR activity on ZnO electrodes has been published before. Thus there is wide open field of investigation for academic research involving numerous parameters, such as synthesis conditions, nanostructure (pore size, grain size, influence of grain boundary) and chemical composition (presence of secondary phases, level of impurities), among others.

Finally, it has to be reminded that the concerns about a potentially high oxygen reduction activity of ZnO that could degrade zinc-based protective coatings were raised in the context of atmospheric corrosion [8-10]. The latter is one of the most important research topic in the field of corrosion. At the lab scale, atmospheric conditions are mimicked by using so-called “thin electrolyte layer (TEL) cells” [11-12]. In these setups, the thickness of the electrolyte above the surface of the working electrode is typically below 100 μm. Evaluating

the electrochemical activity of ZnO towards of ORR with TEL cells while taking the electrolyte thickness as one of the main experimental parameters (along with the potential and the pH, for instance) is a topic of great interest. This could be done by potentiodynamic voltammetry, chronoamperometry or impedance spectroscopy. TEL research could be coupled to the investigation on the synthesis-nanostructure-activity relationships mentioned above by testing ZnO coatings deposited under various conditions. This would provide a valuable basis of fundamental knowledge on oxygen reduction at ZnO electrodes under atmospheric conditions that could be compared to the findings obtained in immersion conditions.

### References

- [1] A. Goux, T. Pauporte, D. Lincot, Oxygen reduction reaction on electrodeposited zinc oxide electrodes in KCl solution at 70°C, *Electrochimica Acta*, 51 (2006) 3168–3172;
- [2] M. Prestat, F. Vucko, B. Lescop, S. Rioual, F. Peltier, D. Thierry, Oxygen reduction at electrodeposited ZnO layers in alkaline solution, *Electrochimica Acta* 218 (2016) 228-236;
- [3] H. S. Wroblowa, S. B. Qaderi, The mechanism of oxygen reduction on zinc, *Journal of Electroanalytical Chemistry and Interfacial Electrochemistry*, 295 (1990) 153-161;
- [4] H. J. Flitt, D. P. Schweinsberg, Synthesis, matching and deconstruction of polarization curves for the active corrosion of zinc in aerated near-neutral NaCl solutions, *Corrosion Science* 52 (2010) 1905–1914;
- [5] S. Rashmi, L. Elias, A.C. Hedge, Multilayered Zn-Ni alloy coatings for better corrosion protection of mild steel, *Engineering Science and Technology, an International Journal* 20 (2017) 1227-1232;
- [6] N. Heller-Ling, M. Prestat, J. L. Gautier, J. F. Koenig, G. Poillerat, P. Chartier, Oxygen electroreduction mechanism at thin  $\text{Ni}_x\text{Co}_{3-x}\text{O}_4$  spinel films in a double channel electrode flow cell (DCEFC), *Electrochimica Acta* 42 (1997) 197-202;
- [7] N. Heller-Ling, G. Poillerat, J. F. Koenig, J. L. Gautier, P. Chartier, Double channel electrode flow cell (DCEFC): application to the electrocatalysis of the oxygen reduction on oxide films, *Electrochimica Acta* 39 (1994) 1669;
- [8] J. Stoullil, T. Prosek, A. Nazarov, J. Oswald, P. Kriz, D. Thierry, Electrochemical properties of corrosion products formed on Zn-Mg, Zn-Al and Zn-Al-Mg coatings in model atmospheric conditions, *Materials and Corrosion* 66 (2015) 777-782;

- [9] T. Prosek, D. Persson, J. Stouilil, D. Thierry, Composition of corrosion products formed on Zn–Mg, Zn–Al and Zn–Al–Mg coatings in model atmospheric conditions, *Corrosion Science* 86 (2014) 231-238;
- [10] T. Prosek, A. Nazarov, U. Bexell, D. Thierry, J. Serak, Corrosion mechanism of model zinc–magnesium alloys in atmospheric conditions, *Corrosion Science*, 50 (2008) 2216–2231;
- [11] M. Stratman, H. Streckel, K.T. Kim, S. Crockett, On the atmospheric corrosion of metals which are covered with thin electrolyte layers – III. The measurement of polarization curves on metal surfaces which are covered by thin electrolyte layers, *Corrosion Science* 30 (1990) 715-734;
- [12] Y.L. Cheng, Z. Zhang, F.H. Cao, J.F. Li, J.Q. Zhang, J.M. Wang, C.N. Cao, A study of the corrosion of aluminum alloy 2024-T3 under thin electrolyte layers, *Corrosion Science* 46 (2004) 1649-1667.



## Annex II

---

*This article has been published in ChemElectroChem: M. Prestat, J. Soares Costa, B. Lescop, S. Rioual, L. Holzer, D. Thierry, ChemElectroChem 5 (2018) 1203, <https://doi.org/10.1002/celec.201701325>*

### **Cathodic corrosion of zinc under potentiostatic conditions in NaCl solutions**

Dr. Michel Prestat, Josiane Soares Costa, Dr. Benoit Lescop, Dr. Stéphane Rioual, Dr. Lorenz Holzer, Prof. Dominique Thierry

#### **Abstract**

Zinc electrodes were polarized cathodically at moderate overpotentials in NaCl 0.6 M solutions under potentiostatic conditions for 7 to 17 hours at room temperature. Corrosion products were characterized by optical microscopy, XRD, Raman microscopy, XPS and FIB-SEM. Close to the open circuit potential, the corrosion products were formed by simonkolleite and the electrochemical response exhibits anodic features. At more negative potentials, the current density remains cathodic throughout the polarization and the deposits on the electrode surface consist almost solely of ZnO. The soluble zinc species necessary for ZnO deposition originate from localized dissolution of the substrate in the form of pits. This effect is assigned to the strong alkalisation of the surface due to oxygen reduction. Despite developing greater surface area than bare zinc substrates, the nanostructured ZnO deposits reduced the cathodic activity.

#### **1. Introduction**

Zinc is a metal of considerable industrial importance since it is extensively employed in pure or alloyed form to protect steel by offering both a physical (barrier) and a galvanic protection [1]. Figuring out its mechanisms of corrosion and the factors that accelerate or hinder its degradation is therefore of prime interest. The progresses on understanding corrosion of zinc and galvanized steel in the last decade have been very recently reviewed by Cole [2].

While a significant body of literature is dedicated to zinc under anodic polarization and/or in alkaline electrolytes [3-12], fewer reports have described the cathodic behaviour of zinc in near-neutral solutions [13-17]. In direct current experiments the latter has been studied potentiodynamically using linear sweep voltammetry at low scan rates (typically around 0.5 to 1 mV/s) that are usually considered to provide “quasi-steady-state conditions”. A potentiodynamic scan in the cathodic domain between the open circuit potential (OCP) of zinc and water reduction onset lasts between 10 and 30 minutes. The resulting polarization curves yield only a short-term picture of the electrochemistry of zinc. The latter is characterized by the following features in most studies (though some small discrepancies might exist from one work to another):

- A current density “plateau” between OCP (around -1.04 V vs. saturated calomel electrode, here after abbreviated SCE) and ca. -1.3 V. The “plateau” is assigned to oxygen reduction to hydrogen peroxide on passive zinc. Rigorously speaking, in all reports, the “plateau” (around  $-10 \mu\text{A}/\text{cm}^2$  in unstirred electrolyte) is not perfectly flat, exhibiting slightly increasing cathodic current with increasingly negative potential. This might originate from small contributions of more cathodic processes (reduction of native ZnO, water reduction, see below) and/or capacitive effects due to potential scan.
- A peak accounting for the reduction of the native ZnO surface layer between ca. -1.3 V and -1.4 V (vs. SCE).
- At more negative potentials, the onset of water reduction (with appearance of small hydrogen bubbles on the electrode surface) that often masks the direct 4-electron oxygen reduction on active zinc.

Cathodic polarization curves including such features have been “synthesized” by Flitt *et al.* [17].

In contrast, the cathodic behaviour of zinc in longer time domains in near-neutral solutions has not been reported yet. Corrosion processes of industrial interest occurs in days, months and years. Thus it is interesting, at the laboratory scale, to bridge the already available short-term data and the long-term behaviour of zinc. In other words, it is relevant to investigate the electrochemical polarization of zinc in the time range of several hours in order to identify processes that cannot be uncovered in rapid potentiodynamic measurements.

In this work, zinc substrates were polarized cathodically under potentiostatic conditions for 7 to 17 hours in NaCl solutions (0.6 M) at pH ~ 6.1. It was shown that, under those conditions, zinc corrodes with deposition of nanostructured ZnO as main corrosion product, as evidenced by Raman microscopy, X-ray diffraction (XRD), X-ray photoelectron spectroscopy (XPS),

optical microscopy and scanning electron microscopy (SEM) for various applied potentials. The presence of  $\text{Zn}^{2+}$  cations in the electrolyte resulting from the dissolution of the substrates was assessed by polarography. The formation of corrosion products under cathodic conditions as well as the electrocatalytic activity of ZnO towards the oxygen reduction reaction (ORR) are discussed.

### Experimental section

The working electrodes were zinc plate from Rheinzink (> 99,7%). The raw zinc plates were grinded down to P4000 grade SiC paper and then with water-based alumina suspension (particle diameter 0.1  $\mu\text{m}$ ) on a polishing cloth. The zinc substrates were then cleaned with ultrasound in absolute ethanol and in distilled water. The electrochemical experiments were performed at room temperature using a cell with a three-electrode configuration and a Gamry Reference 600 potentiostat. The working electrode with a circular area of 1.77  $\text{cm}^2$  exposed to the unstirred electrolyte was placed at the bottom of the cell. A zinc plate below the substrate acted as current collector. The reference electrode was a saturated calomel electrode (SCE). All the potentials values reported in this work are expressed relative to this SCE electrode. The counter-electrode was a titanium-based metallic grid placed ca. 2 cm above the working electrode.

The electrolyte was made of 60 mL of NaCl 0.6 M. The OCP of zinc right after immersion was  $-1.038 \pm 0.006$  V. Deaerated electrolyte was obtained by a constant flow of nitrogen that removed more than 99% of the oxygen initially present in the solution after ca. 30-60 minutes. Oxygen content was continuously measured with an oxygen sensor (Oxy-Mini, World Precision Instrument).

The cathodic behaviour of zinc was studied potentiostatically between -1.05 V and -1.3 V. The potential was first driven from OCP to the targeted potential at a sweep rate of 0.5 mV/s. The current density was then monitored by chronoamperometry for the duration of polarization.

The assessment of the concentration of  $\text{Zn}^{2+}$  in the solutions before and after potentiostatic polarization was carried out externally (Laboceca, Plouzané, France) by polarography.

The identification of the CP was made by Raman spectroscopy (Xplora Plus, Horiba) using a 532 nm laser source and a 1200 diffraction grating in static mode as well as in mapping mode (20 x 20  $\mu\text{m}^2$  maps with 1  $\mu\text{m}$  step). The CP crystalline structure was assessed by XRD with an Empyrean PANalytical device using the  $\text{CuK}\alpha$  radiation (1.5408 Å). The analysed surface area was ca. 4  $\text{mm}^2$ .

Characterization of the outermost nanometers of the surface was carried out by XPS using an apparatus consisting of an Al-Ka X-ray source (Thermo VG) and a cylindrical mirror analyzer (RIBER). The adventitious C(1s) peak was used for the binding energy calibration at 284.8 eV. The analysed surface area was ca. 1 cm<sup>2</sup>.

The microstructure of the zinc samples after polarization was investigated by focused ion beam scanning electron microscopy (FIB-SEM), using a FEI Helios NanoLab 600i. The surfaces of the specimens were first characterized with conventional top-view SEM analysis. Secondary electron imaging was then used to investigate the cross-sections prepared beforehand with FIB-milling and -ion polishing.

Before imaging, these samples were mounted on an aluminium stub and then coated with a platinum layer (ca. 15 nm) to avoid charging and to protect the surface from ion beam damage. Before FIB-milling, beam induced deposition was applied to create an additional carbon layer (ca. 1 x 1 x 20 μm) at the location of each cross-section. This layer is necessary to avoid ion beam damage, to reduce the so-called curtaining effect and to obtain smooth cross-sections. The latter were produced with FIB-milling at 30 kV and with ion-beam currents of 0.79 nA and smaller. Field emission gun imaging was performed using a through the lens detector (TLD) in mode 2 (beam acceleration 2-3 kV, beam current 21-43 pA). In cross-section images, the platinum film (ca. 15 nm) represents a bright reference line that marks the surface of the CP underneath the carbon layer.

Additional top-view micrographs of microscaled pits were obtained with a conventional SEM (SU3500, Hitachi).

## **2. Results and discussion**

### **2.1 Experimental results**

Chronoamperometry analysis allows for distinguishing two kinds of electrochemical behaviour (Figure 1). At -1.05V, the samples behaves cathodically for one to two hours (depending on the sample) before undergoing a sharp increase of the current density that switches to positive values (anodic behaviour) with a peak at ca. 350 μA/cm<sup>2</sup> followed by a smooth decrease (see Figure 1 insert) after the corrosion products have covered a significant fraction of the substrate surface (visible by naked-eye inspection). The current density remains positive till the end of the polarization (stopped after 7 hours). At a slightly more negative potential (-1.075 V), the zinc remains cathodic. This is also the case for the other samples of this study (-1.15 V, -1.2 V, -1.25 V and -1.3 V) as shown on Figure 2 displaying examples of chronoamperometry curves for various potentials.

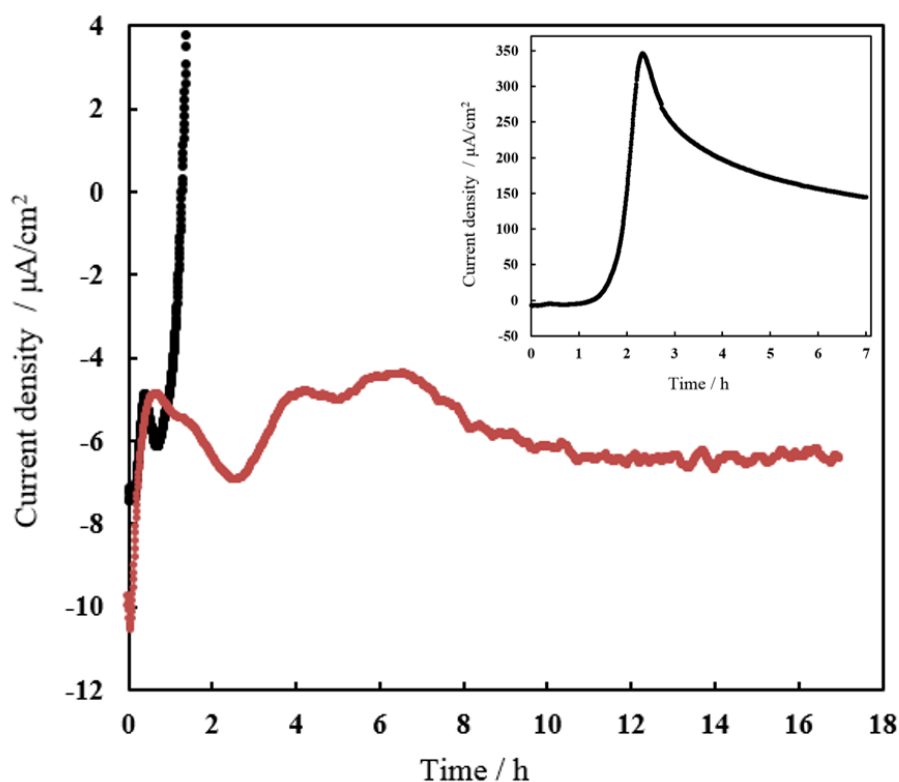


Figure 1: Chronoamperometry curves of zinc electrodes exhibiting anodic behaviour (-1.05 V, black curve + insert) and cathodic behaviour (-1.075 V, red curve).

The plots of Figure 2 are not “typical” in the sense that, for a given potential, the shape of the curves can change significantly from one experiment to another. Yet some well-established trends appear:

- At the beginning of the potentiostatic polarization, the starting current density is, in most cases, between -10 to -15  $\mu\text{A}/\text{cm}^2$  for all samples, except for -1.3 V. This corresponds well to the data of literature obtained by potentiodynamic polarization for the oxygen plateau on zinc covered by its native ZnO layer (as mentioned in the introduction). At -1.3 V, the current density is significantly higher, indicating that the reduction of the native ZnO is ongoing in parallel to oxygen reduction.

- After 17 hours of polarization, the final current density corresponding to the degraded zinc is slightly smaller than the initial value, around -3 to -8  $\mu\text{A}/\text{cm}^2$ .

- No correlation was found between the applied potential and final (or averaged) current densities.

- The pH of the solutions after polarization did not change significantly (increase of 0 to 1, depending on the experiment) and remained in the neutral range regardless of the applied potential.

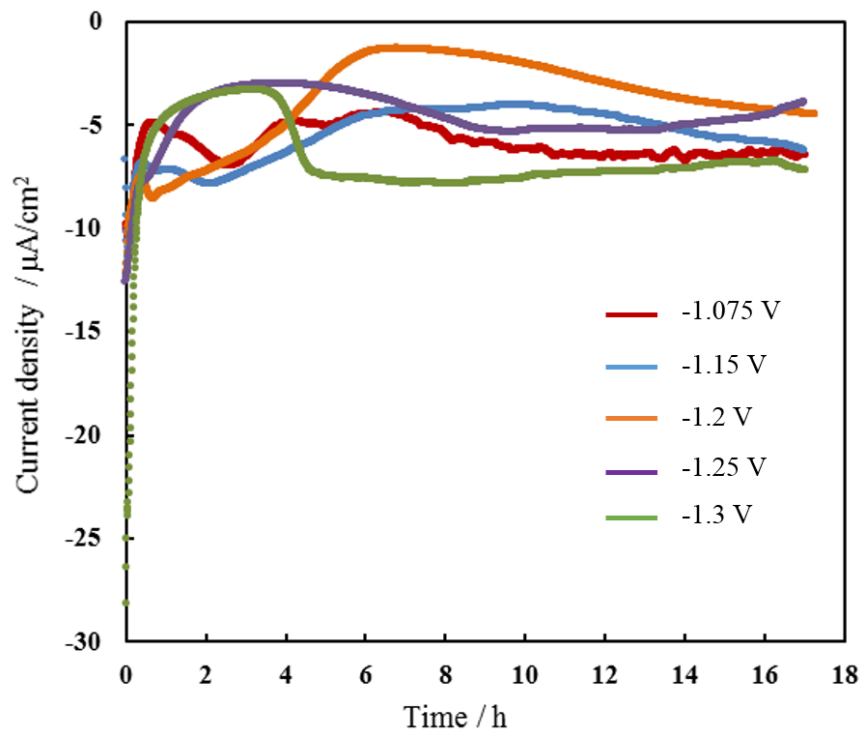


Figure 2: Examples of chronoamperometry curves at various potentials. All samples exhibit a cathodic behaviour throughout the polarization (for 17 hours).

Figure 3 shows optical microscope pictures of zinc substrates before and after cathodic polarization. The pristine zinc appears in dark contrast (Fig. 3a). The latter is replaced by the greyish colour of the corrosion products (CP), evidencing unambiguously a degradation of the material. Fig. 3b shows the images of a specimen polarized at -1.05 V till the switch from negative to positive current density occurs, i.e. the experiment was stopped when the current density was  $0 \mu\text{A}/\text{cm}^2$  (after 1 to 2 hours). A large pit surrounded by corrosion products characterizes the sample at this point of the polarization. After the 7 hours at -1.075 V (5 to 6 hours in the anodic regime), the CP covers fully the substrate.

The corrosion degradation of the samples with cathodic behaviour (Fig. 3d-h), which constitutes the main focus of this paper, reaches a maximum around -1.2 V. It clearly appears that the aspect of the greyish layer depends on the applied potential and the growth process is spatially heterogeneous. Multiple small pits surrounded by “halos” of corrosion products can be observed. This is particularly noticeable for -1.075 V when the CP cover only a small

fraction the zinc substrate (see also Fig. 9b below). Noteworthy is the fact that zinc degradation occurs at potentials as negative as  $-1.3\text{V}$  (to a limited extent though).

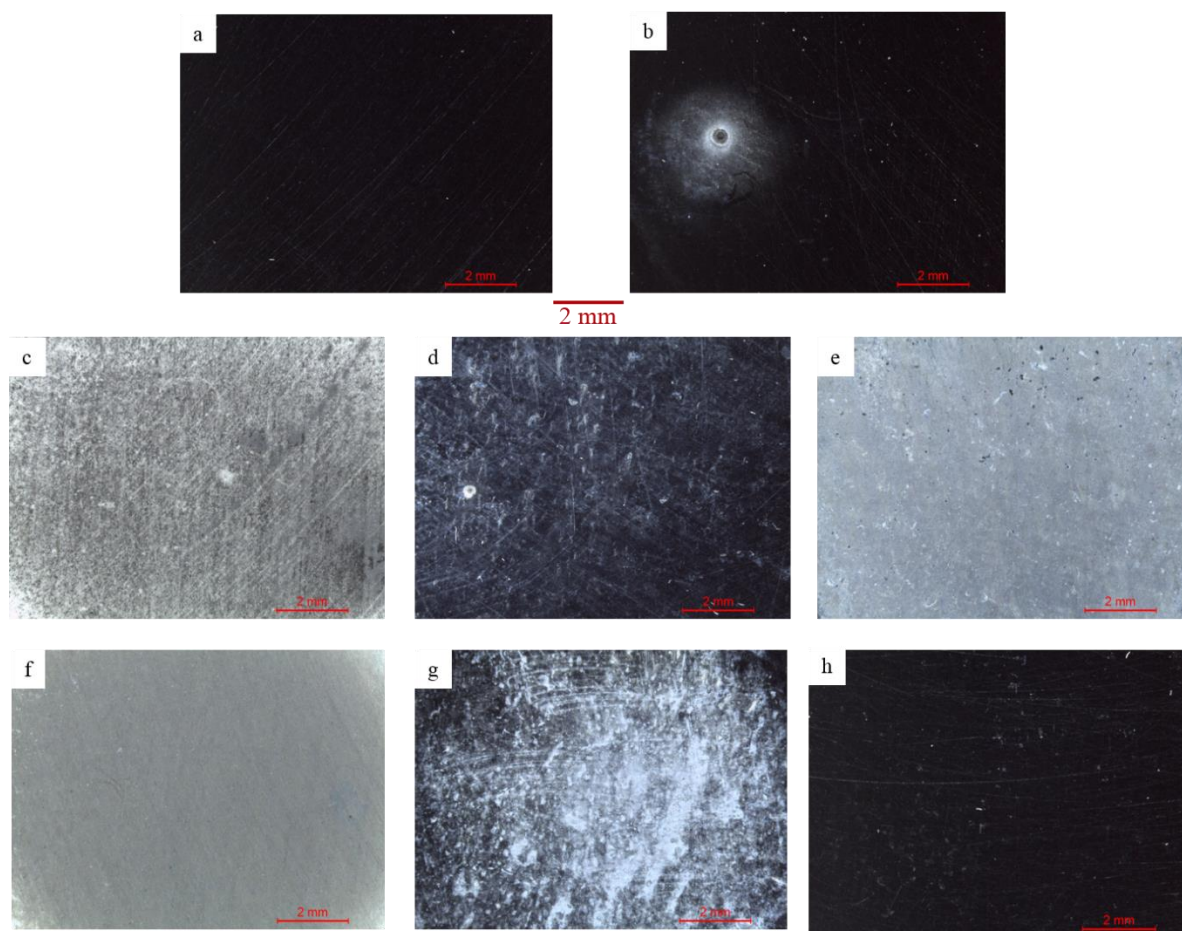


Figure 3: Optical microscope pictures of the zinc samples after cathodic polarization at various potentials. If not otherwise mentioned, the duration of polarization was 17 hours. a) pristine zinc substrate (as reference); b)  $-1.05\text{ V}$  for 1.5 hours; c)  $-1.05\text{ V}$  for 7 hours; d)  $-1.075\text{ V}$ ; e)  $-1.15\text{ V}$ ; f)  $-1.2\text{ V}$ ; g)  $-1.25\text{ V}$ ; h)  $-1.3\text{ V}$ .

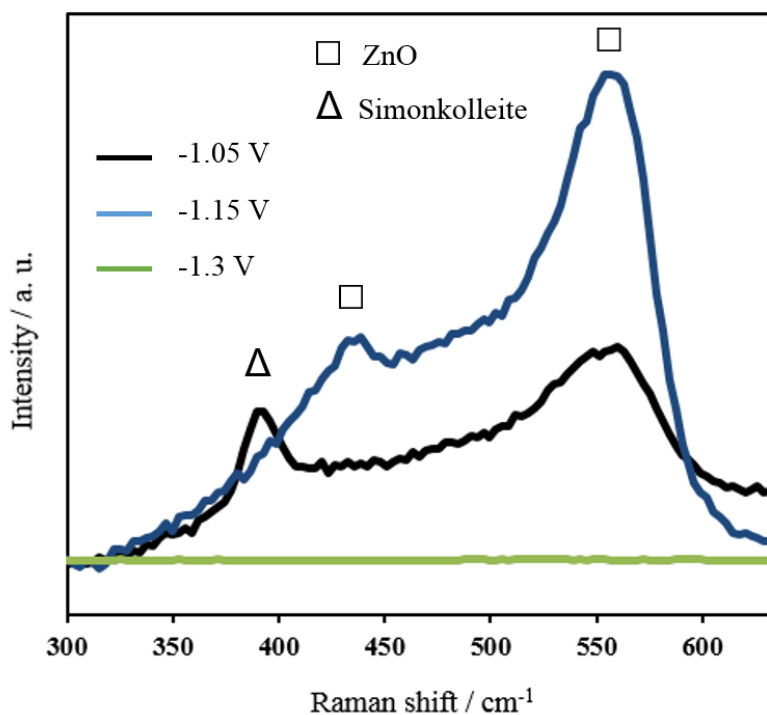


Figure 4: Raman microscopy analysis of the corrosion products for three different potentials.

The chemical analysis of the CP was first done by Raman microscopy in mapping mode. As the maps do not exhibit significant contrast due to the limited number of CP, Figure 4 shows only the typical spectra for each applied potential. ZnO is found on all samples with typical vibrations at  $435\text{ cm}^{-1}$  and  $560\text{ cm}^{-1}$  [18-20], except for the samples polarized at -1.3 V for which the amount of CP was too low to be detected. The zinc specimens that exhibit anodic behaviour (-1.05 V) contain simonkolleite as well, as evidenced by the peaks at  $390\text{ cm}^{-1}$  and at  $3500\text{ cm}^{-1}$  (not shown here) [18-21].



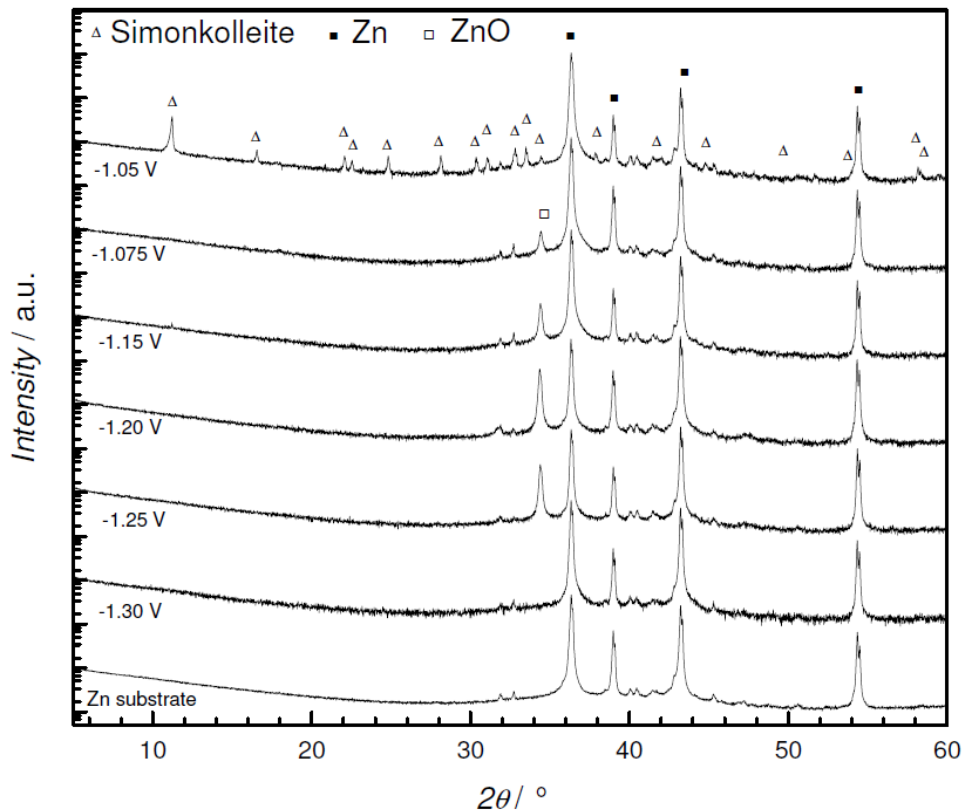


Figure 5: X-ray diffractograms of the zinc samples after 17 hours of potentiostatic polarization (7 hours for the -1.05 V polarization) as a function of the applied potential. Pristine zinc substrate is also shown as reference. Note the logarithmic scale of the y-axis.

X-ray diffraction analysis of the samples after 17 hours of various cathodic polarizations (7 hours for the -1.05 V sample) is presented in Figure 5. Simonkolleite reflections can only be found after polarization at -1.05 V, confirming thereby the Raman microscopy results [18,22-24]. For the other potentials, ZnO is the main crystalline structure (besides that of the zinc substrate). While going towards negative potentials, the intensity of the main ZnO reflection (002) at  $34.4^\circ$  increases till -1.2V and decreases till almost zero at -1.3V. This is in good agreement with naked-eye and optical microscopy observations (Fig. 3) showing that the thickest deposit is obtained at -1.2V.

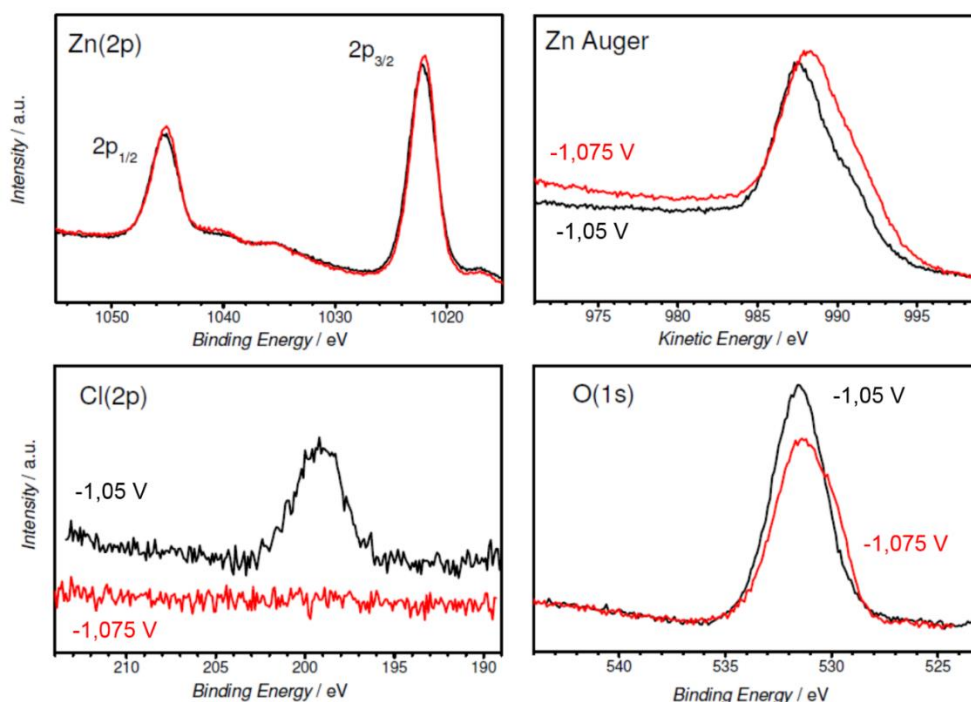


Figure 6: XPS analysis of zinc electrodes polarized at -1.05 V for 7 hours (anodic behaviour, black curves) and -1.075 V for 17 hours (cathodic behaviour, red curves).

In Figure 6, XPS characterization demonstrates clearly the appearance of different chemical species at the surface depending on the electrochemical behaviour (anodic or cathodic). The spectra measured after polarization of -1.05 V are very similar to those observed for simonkolleite-containing heterostructures grown anodically on zinc [18]. The Cl(2p) spectrum exhibits a peak at 199.1 eV close to the simonkolleite data of Duchoslav *et al.* [25]. The single peak localized at 531.5 eV in the O(1s) spectrum is attributed to the oxygen of hydroxides or carbonates. The derived Auger parameter,  $\alpha$ , obtained from the sum of Zn(2p) binding energy and Auger kinetic energy is equal to 2009.7 eV, a value identical to that found for simonkolleite in [18]. The spectra measured on the sample after polarization at -1.075 V display different characteristics. No peak appears on the Cl(2p) spectrum, evidencing thus the absence of simonkoellite on the surface. The O(1s) spectrum shows a complex structure with a clear asymmetric tail at low binding energy. It is explained by the contribution of zinc hydroxide/carbonate components at 531.5 eV and ZnO at about 530 eV. Differentiation of the species present on the surface cannot be achieved on the basis of the Zn(2p) spectrum only. Yet the value of the Auger parameter  $\alpha$  (2010.3 eV) confirms the presence of ZnO [26].

The microstructure of the CP layers has been analysed by FIB-SEM (Fig. 7). The coating produced at -1.05 V with positive current density (Fig. 7a and 7b) exhibits a heterostructure

resembling that recently reported by Prestat *et al.* for zinc anodically polarized at -0.64 V in 0.1 M NaCl [18]. It consists of a “forest” of simonkolleite nanosheets on top of a porous interlayer covering the substrate. The presence of ZnO is evidenced by Raman spectroscopy and XRD (Fig. 4 and Fig. 5). As in [18], the fact that XPS measurements do not detect ZnO (Fig. 6) suggests that the latter is located in the innermost part of the coating (i.e. in the interlayer).

For the cathodic samples, at the sites covered by the CP, the microstructure consists of nanostructured “cone-shaped” features (more clearly visible on the -1.2 V sample, Fig. 7e and 7f) that grow perpendicularly to the substrate. The “cones” have a diameter of ca. 100 nm and are separated by gaps that make the layers rough.

Although it is difficult to assess a growth rate for such layers that are heterogeneous at both the macroscopic and microscopic scales, orders of magnitude can be estimated by measuring the height of the most typical microstructural features. For the polarization at -1.2V, the growth rate is around 20-30 nm/h whereas at -1.075 V, it is rather 2-3 nm/h. Yet this value should be mitigated by the fact that the CP covers only a fraction of the substrates.

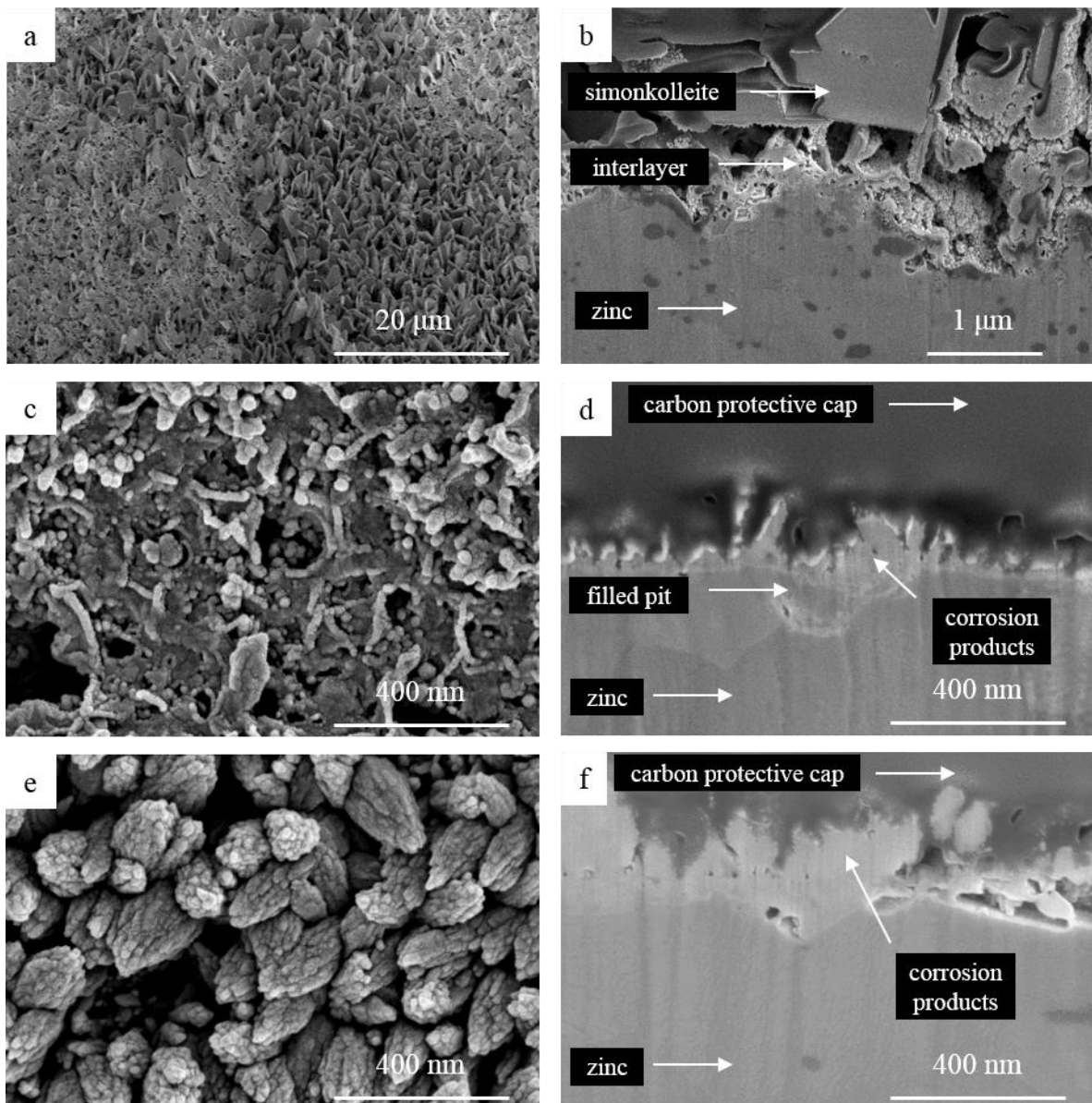


Figure 7: FIB-SEM analysis of the corrosion product layers after polarization at different potentials. Top-view micrographs: a, c, and e; Cross-section micrographs: b, d and f. a,b)  $-1.05\text{V}$  for 7 hours (anodic behaviour); c,d)  $-1.075\text{ V}$  for 17 hours (cathodic behaviour); e,f)  $-1.2\text{ V}$  for 17 hours (cathodic behaviour).

In order to gain understanding about growth mechanism of the ZnO layers, polarization experiments in aerated and deaerated electrolytes were performed for 7 hours (Fig. 8). Under aerated conditions, corrosion products can be observed, mostly as “halos” around pits (Fig. 8b, see also Fig. 9b). Conversely, under deaerated conditions, the decrease of oxygen concentration in the solution (by a factor of 100) considerably reduces the degradation of the zinc substrates (Fig. 8c, see also Fig. 9d) with a lower number of pits, smaller pit sizes, and almost no CP “halos”. The fact that zinc does not completely remains in

its pristine state can be assigned to the first hour of deaerating during which oxygen was still present in the electrolyte and could initiate the degradation process. These findings clearly demonstrate that oxygen reduction plays a key-role in the corrosion of zinc and the deposition of ZnO. Note that the current density under deaerated conditions is not zero and is assigned to water reduction.

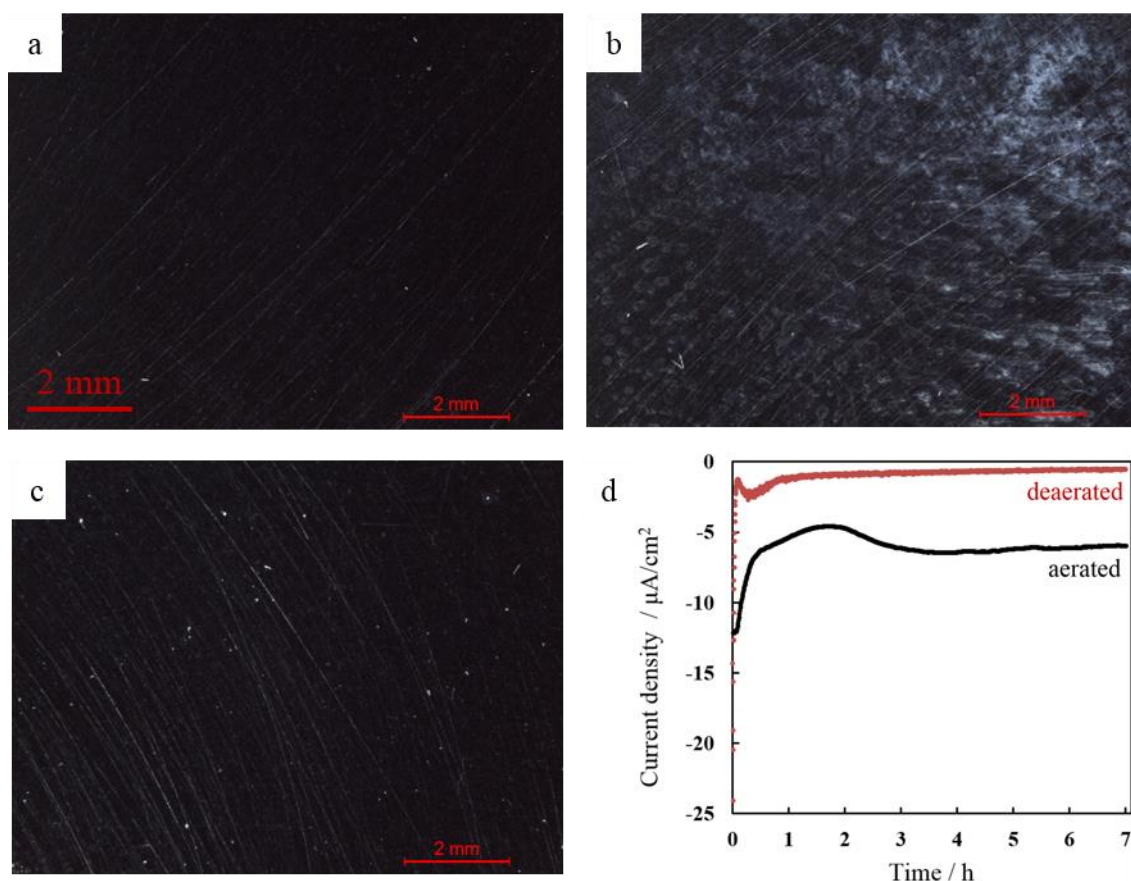


Figure 8: Optical microscopy images of zinc samples after 7 hours of polarization at -1.2 V with various concentration of oxygen: a) pristine zinc substrate (as reference); b) aerated conditions,  $[\text{O}_2] \sim 9$  ppm ( $0.28 \mu\text{mol/L}$ ); c) deaerated conditions,  $[\text{O}_2] < 0.09$  ppm; d) Corresponding chronoamperometry curves.

Conventional SEM was also used to image the pits on substrates that are not fully covered by the CP (Fig. 9). Unfilled pits were more often observed for samples with slow ZnO deposition, e.g. at -1.075 V (Fig. 9a), or undergoing very limited degradation, e.g. at -1.3 V (Fig. 9c) and under deaerated conditions (Fig. 9d). At -1.3 V, ZnO can be reduced to zinc which probably explains the absence of corrosion products. Conversely pits filled with CP were principally (but not exclusively) found at higher deposition rates of ZnO, e.g. at -1.2 V (Fig. 9b). Multiple point-analyses with Raman microscopy confirmed the main corrosion



product was ZnO though traces of simonkolleite could be sometimes found in the pits or in the surrounding CP halos. This SEM analysis indicates that pitting of zinc is possible under cathodic polarization while it has been essentially studied in anodic regimes so far [7,8].

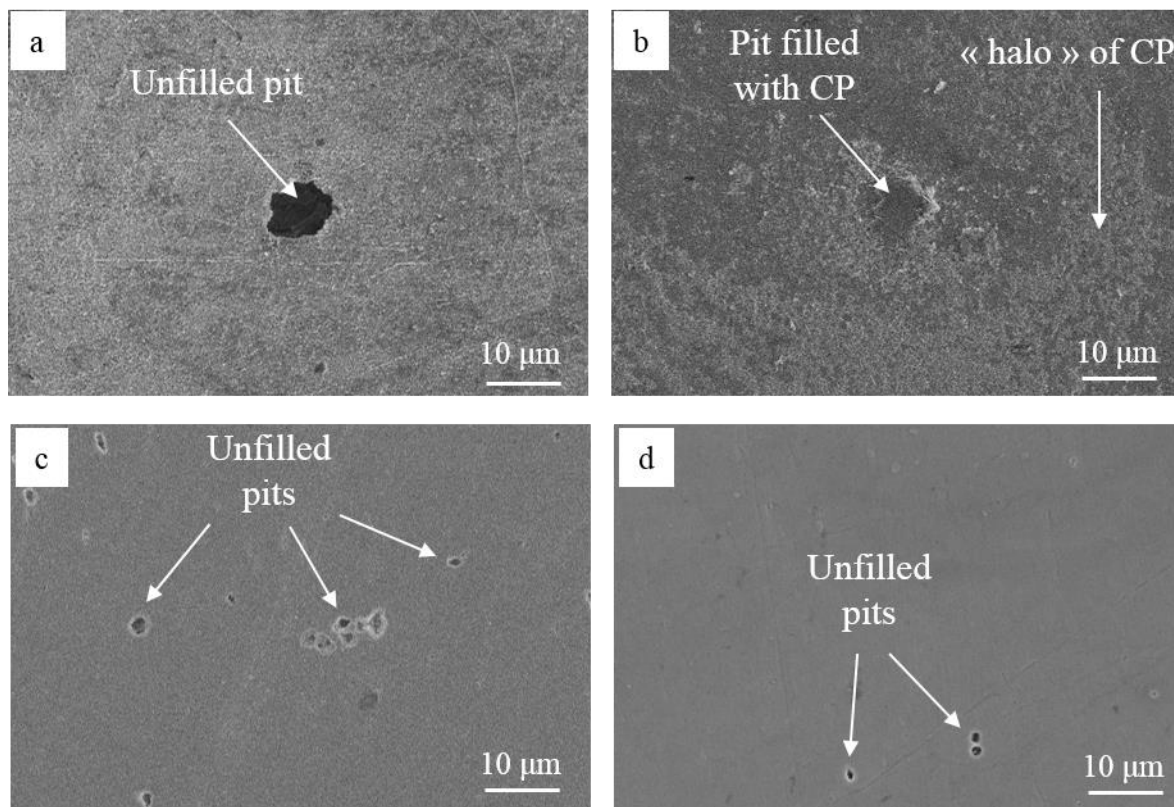


Figure 9: Conventional SEM top-view micrographs of typical pits observed after cathodic polarization in NaCl 0.6 M at various potentials and durations in aerated conditions (except d): a) - 1.075 V for 17 hours; b) -1.2 V for 7 hours; c) -1.3 V for 17 hours; d) -1.2 V for 7 hours (deaerated conditions).

To confirm this finding, the analysis of the solutions was carried out by polarography. The measurements were done after polarization (i.e. after consumption of  $Zn^{2+}$  for forming the ZnO deposit). It cannot account for the local concentration at the electrode/electrolyte interface during the deposition process. Furthermore it does not measure the variation of  $Zn^{2+}$  concentration with time. Hence the results presented here have essentially a qualitative meaning and constitutes only a “snapshot” of the accumulated  $Zn^{2+}$  after 17 hours. A concentration of ca. 0.03 µmol/L (close to the method’s detection limit) was found for the blank sample (as-prepared NaCl solution) while, for the electrolytes after polarization, the concentrations ranged between 0.8 -2.3 µmol/L. Hence, notwithstanding the limitations of the analysis mentioned above, the polarographic measurements unambiguously confirm the

corrosion of the zinc substrate. The possible origin(s) of the transfer of zinc from the substrate to the solution are discussed in Section 2.2.

## 2.2 Discussion

This discussion mainly focuses on the samples with cathodic behaviour. At -1.05 V, the electrochemical response of zinc is mostly anodic. As this applied potential is close to the OCP (ca. -1.038 V), the anodic current is believed to be significant enough to release enough  $\text{Zn}^{2+}$  in the solution to shift the onset of zinc dissolution negatively and trigger the cathodic-to-anodic switch observed after one or two hours (Fig. 1 insert). The anodic behaviour is then self-sustained by the strong oxidation current. The microstructure of the deposits is similar to that of the CP produced at more positive potentials (+0.64 V) [18,22,27] with a typical simonkolleite-interlayer heterostructure on top of the zinc substrates.

The results from the more negatively polarized specimens ( $\leq -1.075$  V) reveal that the zinc undergoes corrosion under cathodic conditions. This degradation is unambiguously evidenced by the formation of pits,  $\text{Zn}^{2+}$  detection in the electrolyte by polarography and ZnO deposits. The ZnO growth rate is rather slow (ca. 2 to 30 nm/h), making thereby this degradation very difficult to observe with the usual short-duration potentiodynamic experiments.

Recently Shkirskiy *et al.* investigated the cathodic (potentiodynamic) polarization of zinc in NaCl 0.5 M with and without addition of L-cysteine using atomic emission spectroelectrochemistry (AESEC) [28]. In the absence of L-cysteine (i.e. in pure NaCl), they observed a hint of a zinc dissolution plateau at moderate negative overpotentials. The current density plateau was enhanced by increasing the concentration of L-cysteine and the complexation of the latter with  $\text{Zn}^{2+}$ . Note that the AESEC technique is based on potentiodynamic polarization in an electrochemical flow cell in which the electrolyte is constantly renewed making difficult the detection of low current density processes. This stands in contrast with the long potentiostatic polarization experiments of the present work allowing for the accumulation of products from sluggish reactions. The two approaches are complementary and, interestingly, they both tend to prove the cathodic dissolution of zinc.

As shown in Fig. 8, there is almost no deposition of ZnO under deaerated conditions. Furthermore, the number of pits observed by optical microscopy is considerably reduced (but not zero). This result is also confirmed by SEM investigations (not shown here). This suggests that the origin of zinc soluble species (that is necessary for ZnO deposition) is linked to the occurrence of oxygen reduction. The latter is likely to enhance the surface alkalinity to

such high levels (pH > 12-13) that the soluble zinc hydroxycomplexes  $\text{Zn(OH)}_3^-$  and/or  $\text{Zn(OH)}_4^{2-}$  are formed [5,6]. On the basis of microscopy observations, it can also be postulated that, under cathodic polarisation (i.e. with a low anodic activity), this type of corrosion occurs only in localized form (pits).

At this point of our research, it is very challenging to establish a detailed mechanism of the ZnO growth due to the high complexity of the electrode/electrolyte interface. The main reasons are:

- The multiple reactions and electroactive species at play, i.e. zinc dissolution and oxygen reduction involving Zn,  $\text{Zn}^{2+}$ ,  $\text{O}_2$ ,  $\text{H}_2\text{O}_2$  (or  $\text{HO}_2^-$ ). Aggressive  $\text{Cl}^-$  ions might also play an important role in the pitting process.

- The ability of both zinc and zinc oxide to reduce oxygen and hydrogen peroxide.

- The lack of fundamental knowledge on mechanisms and kinetics of some of those reactions (e.g. reduction of  $\text{O}_2$  and  $\text{H}_2\text{O}_2$  on ZnO).

- The constantly evolving electrode surface whose chemical composition and morphology change throughout the deposition process.

- The spatially heterogeneous nature of the growth process (as illustrated by Fig. 8b and Fig. 9)

In what follows, two possible frameworks for ZnO growth based on different assumptions of the surface pH (near-neutral and highly alkaline) are exposed. Note that, in view of the spatially heterogeneous growth, it is possible, and even likely, that the two types of growth exist simultaneously at different sites of the electrode.

In the areas around the pits characterized by high pH values, deposition of ZnO may follow the mechanisms proposed by Thomas *et al.* while revisiting zinc passivation in alkaline NaCl solutions [5]. In that model,  $\text{Zn(OH)}_3^-$  and  $\text{Zn(OH)}_4^{2-}$  anions might directly precipitate:



These ZnO deposits might be those forming the “halos” of CP around the pits clearly visible in Fig. 8b and 9b.

In [5], Thomas *et al.* mainly worked with alkaline droplets under free corrosion conditions or in solutions under slightly anodic conditions to produce the CP patinas. The



deposited layers look rather homogeneous and do not seem related to pitting. Thus it seems that, under cathodic conditions, alkaline dissolution of zinc is a more localized process than under anodic conditions. The slow grow rates estimated with FIB-SEM analysis is consistent with the limited supply of  $\text{Zn}^{2+}$  due to pitting.

Some of the  $\text{Zn}(\text{OH})_3^-$  and  $\text{Zn}(\text{OH})_4^{2-}$  anions might subsequently diffuse to the bulk of the solution (that remains near-neutral in view of the post-mortem pH measurements) and re-dissociate as  $\text{Zn}^{2+}$  and  $\text{OH}^-$ . The  $\text{Zn}^{2+}$  cations are then available for participating in a deposition process at sites with limited alkalisation and/or under near-neutral conditions. For such deposition, one can establish an analogy with cathodic electrodeposition since ZnO formation is related to both the ORR and to the presence of  $\text{Zn}^{2+}$  in the electrolyte. ZnO is an oxide of significant relevance for various technological applications, e.g. in solar cells, sensors, and transistors [29]. Thus many reports are dedicated to ZnO thin film deposition techniques, among which electrodeposition is acknowledged for its simplicity, cost-effectiveness and potential for upscaling [30]. It is performed using, among others, soluble zinc nitrate [26, 31-34] or zinc chloride salts [35-41]. The working principle is that oxygen or an oxygen precursor (nitrates, hydrogen peroxide) is reduced into  $\text{OH}^-$  that subsequently reacts with  $\text{Zn}^{2+}$  to yield ZnO. In terms of chemical composition, the electrolyte used in the present study (NaCl 0.6 M with small concentrations of  $\text{Zn}^{2+}$ ,  $\text{O}_2$  and  $\text{H}_2\text{O}_2$ ) is best compared with electrodeposition bath based on chlorides with oxygen or hydrogen peroxide precursors [37,42]. The involved (electro)chemical reactions are:

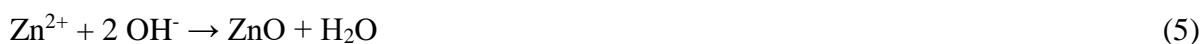
With oxygen precursor:



With hydrogen peroxide precursor:



Subsequent ZnO deposition:



While most of the reports are dedicated to electrodeposition at temperatures higher than ca. 40 °C, some studies also demonstrated that ZnO could be formed at room temperature [34,35]. In electrodeposition, the dissolved zinc precursor salt is equally distributed in the electrolyte. This tends to lead to homogeneous growths and smooth

chronoamperometry curves that are relatively easy to understand and model [26,35,36,39]. In contrast, in the present work, the  $\text{Zn}^{2+}$  cations originate from the substrate due to some pitting-based dissolution process that is stochastic by nature. This generates a spatially heterogeneous distribution of the electroactive species that certainly contributes to the uneven deposition of ZnO on the substrate (Fig. 3d, 3g and 8b). It is therefore not surprising that, unlike classical electrodeposition, the shape of the chronoamperometric curves (Fig. 2) is not steadily reproducible from one trial to another (though staying always in the same current density ranges) and is difficult to interpret.

It is also interesting to analyse the order of magnitudes of ZnO growth rates of this study with those reported for electrodeposition in chloride-based baths. Cross-sectional FIB-SEM analysis (Fig. 7) shows the deposition rates are less than 2-3 nm/h at -1.075V (with a partial coverage of substrate by the CP) and ca. 20-30 nm/h at -1.2 V. With electrodeposition, Pauporté *et al.* and Goux *et al.* reported 1000 nm/h at room temperature and 34 °C, respectively [35,36]. Above 50 °C, Fahoume *et al.* measured deposition rates of 400 nm/h to 1000 nm/h, depending on the pH [39]. All those studies utilized solutions with a  $\text{Zn}^{2+}$  concentration of 5 mM, i.e. three orders of magnitude higher than the values measured after 17 hours of potentiostatic polarization. These comparisons suggest that, in the present study, the slow formation of ZnO is directly related to a sluggish supply of  $\text{Zn}^{2+}$ .

Our findings provide hard evidence for zinc dissolution and ZnO formation. Yet several questions remain open. For instance, it is not understood why the maximal deposition rate is observed at -1.2 V. The two frameworks presented above constitute only a basis for future research and more investigations are needed to fully understand the growth mechanism under cathodic conditions.

The last point of this discussion is cathodic activity in presence of ZnO. As pointed out by Cole's recent review [2], there is an ongoing debate on the still poorly known electrocatalytical properties of ZnO towards ORR with contradictory conclusions [4,16,18,26]. In the present study, it is relevant to focus attention on the samples polarized at -1.2 V with ZnO covering almost fully the zinc substrates. It can be approximated that their electrochemical response is that of ZnO with negligible contribution of zinc. As demonstrated by the FIB-SEM analysis (Fig. 7e and 7f), those ZnO layers are nanostructured and exhibit cone-shaped features with a diameter of ca. 100 nm and with gaps of similar size between them. Moreover, each cone possesses a nanoscaled roughness due to small grains with a size of ca. 20 nm. Due to its fineness, this kind of nanostructure develops a surface area in contact with the electrolyte that is much higher than that of bare zinc substrates. Nonetheless the

current density during potentiostatic polarization (i.e. during the development of the nanostructure) does not increase but remains more or less stable around  $-5 \mu\text{A}/\text{cm}^2$ . This value is slightly lower than that at the start of the experiment (ca.  $-10 \mu\text{A}/\text{cm}^2$ , representing zinc in uncorroded state). Therefore it can be concluded that, under the experimental conditions of the present work, ZnO has a lower activity than zinc towards ORR. Those findings are in line with the recent study of Prestat *et al.* in which zinc patinas were anodically produced in NaCl solutions [18]. While performing ORR measurements, the reduced cathodic activity was assigned to a thin nanostructured ZnO-rich layer covering the zinc substrates.

### 3. Conclusions

Zinc substrates were polarized potentiostatically at moderate cathodic overpotentials for 7 to 17 hours in NaCl solution. The results of this study provide a different picture than that obtained with potentiodynamic measurements. Close to the open circuit potential, at  $-1.05 \text{ V}$ , the samples behave mostly anodically and produce patinas with ZnO and simonkolleite. At  $-1.075 \text{ V}$  (and more negative potentials), the electrochemical response is completely different. The current density remains cathodic and the alkalisation of the substrate surface is believed to bring about zinc dissolution (pitting). The  $\text{Zn}^{2+}$  cations released in the solution are involved in the spatially heterogeneous deposition of nanostructured ZnO. The replacement of zinc by ZnO sites at the electrode/electrolyte interface reduces the cathodic current density. Since the nanostructured ZnO develops a significantly larger surface area than the zinc substrates, it is concluded that, under the experimental conditions of the present work, ZnO is less active than zinc towards oxygen reduction.

In the future, more investigations are needed to acquire a deeper knowledge about the mechanism(s) and kinetics of zinc dissolution and oxygen reduction at ZnO. For instance, the dependence of the ZnO growth rate on the applied potential has not been elucidated and it is not understood yet why the ZnO growth reaches a maximum at  $-1.2 \text{ V}$ . Probe-based methods may also provide relevant insight about the processes at play during polarization. For instance, pH microprobe measurements could bring a direct and *in situ* confirmation of the locally high degree of alkalisation due to ORR [43]. Scanning vibrating electrode technique and scanning electrochemical microscopy investigations might help gain understanding on the formation of pits, notably during the early stages of polarization [44,45]. Finally potentiostatic investigations could be conducted under thin electrolyte layers so as to compare

the results of the present work with those obtained under conditions closer to atmospheric corrosion.

### References

- [01] X.G. Zhang, Corrosion and electrochemistry of zinc, Plenum Press, New York, 1996.
- [02] I.S. Cole, *Materials* **2017**, *10*, 1288.
- [03] H.S. Wroblowa, S.B. Qaderi, *J. Electroanal. Chem.* **1990**, *295*, 153-161.
- [04] S. Thomas, I.S. Cole, Y. Gonzalez-Garcia, M. Chen, M. Musameh, J.M.C. Mol, H. Terryn, N. Birbilis, *J. Appl. Electrochem.* **2014**, *44*, 747-757.
- [05] S. Thomas, I.S. Cole, M. Sridhar, N. Birbilis, *Electrochim. Acta* **2013**, *97*, 192-201.
- [06] S. Thomas, N. Birbilis, M.S. Venkatraman, I.S. Cole, *Corrosion* **2012**, *68*, 015009.
- [07] W. Miao, I.S. Cole, A.K. Neufeld, S. Furman, *J. Electrochem. Soc.* **2007**, *154*, C7-C15.
- [08] F.H. Assaf, S.S. Abd El-Rehiem, A.M. Zaky, *Mater. Chem. Phys.* **1999**, *58*, 58-63.
- [09] M. Mokaddem, P. Volovitch, K. Ogle, *Electrochim. Acta* **2010**, *55*, 7867-7875.
- [10] E.E. Abd El Aal, *Corros. Sci.* **2004**, *46*, 37-49.
- [11] I.M. Ismail, O.E. Abdel-Salam, T.S. Ahmed, A. Soliman, I.A. Khattab, M.F. Al-Ebrahim, *Port. Electrochim. Acta* **2013**, *31*, 207-219.
- [12] M. Mouanga, P. Berçot, *Corros. Sci.* **2010**, *52*, 3993-4000.
- [13] W.J. Tomlinson, D.R. Breary, *Corrosion* **1988**, *44*, 62-63.
- [14] H. Leidheiser, Y. Momose, R.D. Granata, *Corrosion* **1982**, *38*, 178-179.
- [15] H. Leidheiser, I. Suzuki, *Corrosion* **1980**, *36*, 701-702.
- [16] A. Nazarov, E. Diler, D. Persson, D. Thierry, *J. Electroanal. Chem.* **2015**, *737*, 129-140.
- [17] H.J. Flitt, D. Paul Schweinsberg, *Corros. Sci.* **2010**, *52*, 1905-1914.
- [18] M. Prestat, L. Holzer, B. Lescop, S. Rioual, C. Zaubitzer, E. Diler, D. Thierry, *Electrochem. Commun.* **2017**, *81*, 56-60.
- [19] M.C. Bernard, A. Hugot-Le Goff, D. Massinon, N. Phillips, *Corros. Sci.* **1993**, *35*, 1339-1349.
- [20] T. Ohtsuka, M Matsuda, *Corrosion* **2003**, *59*, 407-413.
- [21] S. Khamlich, T. Mokrani, M.S. Dhlamini, B.M. Mothudi, M. Maaza, *J. Colloid Interface Sci.* **2016**, *461*, 154-161.
- [22] J.D. Yoo, P. Volovitch, A. Abdel Aal, C. Allely, K. Ogle, *Corros. Sci.* **2013**, *70*, 1-10.
- [23] J. Sithole, B.D. Ngom, S. Khamlich, E. Manikanadan, N. Manyala, M.L. Saboungi, D. Knoessen, R. Nemitudi, M. Maaza, *Appl. Surf. Sci.* **2012**, *258*, 7839-7843.

- [24] S.R. Tavares, V.S. Vaiss, F. Wypych, A.A. Leitão, *J. Phys. Chem. C* **2014**, *118*, 19106-19113.
- [25] J. Duchoslav, M. Arndt, T. Keppert, G. Luckeneder, D. Stifter, *Anal. Bioanal. Chem.* **2013**, *405*, 7133-7144.
- [26] M. Prestat, F. Vucko, B. Lescop, S. Rioual, F. Peltier, D. Thierry, *Electrochim. Acta* **2016**, *218*, 228-236.
- [27] J.D. Yoo, K. Ogle, P. Volovitch, *Corros. Sci.* **2014**, *81*, 11-20.
- [28] V. Shkirskiy, P. Keil, H. Hintze-Bruening, F. Leroux, P. Volovitch, K. Ogle, *Electrochim. Acta* **2015**, *184*, 203-213.
- [29] Y.B. Hahn, *Korean J. Chem. Eng.* **2011**, *28*, 1797-1813.
- [30] E.M. Elsayed, F.A. Harraz, A.E. Saba, *Int. J. Nanoparticles* **2012**, *5*, 136-148.
- [31] M. Izaki, T. Omi, *Appl. Phys Lett.* **1996**, *68*, 2439-2440.
- [32] M. Nobial, O. Devos, B. Tribollet, *J. Cryst. Growth* **2011**, *327*, 173-181.
- [33] T. Yoshida, D. Komatsu, N. Shimokawa, H. Minoura, *Thin Solid Films* **2004**, *451*, 166-169.
- [34] M. Wadowska, T. Frade, D. Siopa, K. Lobato, A. Gomes, *ECS Electrochem. Lett.* **2013**, *2*, D40-D42.
- [35] T. Pauporté, I. Jirka, *Electrochim. Acta* **2009**, *54*, 7558-7564.
- [36] A. Goux, T. Pauporté, J. Chivot, D. Lincot, *Electrochim. Acta* **2005**, *50*, 2239-2248.
- [37] T. Pauporté, D. Lincot, *J. Electroanal. Chem.* **2001**, *517*, 54-62.
- [38] S. Hori, T. Suzuki, T. Suzuki, S. Miura, S. Nonomura, *Mater. Trans.* **2014**, *55*, 728-734.
- [39] M. Fahoume, O. Maghfoul, M. Aggour, B. Hartiti, F. Chraïbi, A. Ennaoui, *Sol. Energy. Mat. Sol. Cells* **2006**, *90*, 1437-1444.
- [40] R. Salazar, C. Lévy-Clément, V. Ivanova, *Electrochim. Acta* **2012**, *78*, 547-556.
- [41] K. Laurent, B.Q. Wang, D.P. Yu, Y. Leprince-Wang, *Thin Solid Films* **2008**, *517*, 617-621.
- [42] A. Henni, A. Merrouche, L. Telli, S. Walter, A. Azizi, N. Fenineche, *Mater. Sci. Semicond. Process.* **2015**, *40*, 585-590.
- [43] M.G. Taryba, M.F. Montemor, S.V. Lamaka, *Electroanalysis* **2015**, *27*, 2725-2730.
- [44] R.M. Souto, Y. González-García, D. Battistel, S. Daniele, *Chem. Eur. J.* **2012**, *18*, 230-236.
- [45] E. Mena, L. Veleza, R.M. Souto, *Int. J. Electrochem. Sci.* **2016**, *11*, 5256-5266.



Étude de la réduction de l'oxygène sur des films minces de ZnO élaborés par pulvérisation cathodique

**Mots clés :** oxyde de zinc, pulvérisation cathodique, réduction de l'oxygène.

**Résumé :** La corrosion est un processus électrochimique impliquant une réaction d'oxydation (dissolution du métal) équilibrée par une réaction de réduction. La réduction de l'oxygène (ORR, oxygen reduction reaction) est l'une des principales réactions cathodiques en corrosion. L'oxygène peut être réduit directement en ions hydroxyle ou indirectement avec le peroxyde d'hydrogène comme espèce intermédiaire. Dans cette thèse de doctorat, l'ORR a été étudiée sur des couches de ZnO qui est un produit de corrosion commun du zinc, un métal de grand intérêt industriel. Des électrodes modèles (films de ZnO texturés et non texturés) ont été déposées sur des substrats de cuivre en utilisant la technique de pulvérisation cathodique. L'ORR a été étudiée dans un électrolyte alcalin en utilisant une électrode tournante à disque et à anneau. Les courbes de polarisation ont révélé un fissurage des films de ZnO texturés qui s'est avéré être dépendant du potentiel appliqué.

La spectroscopie d'impédance électrochimique a été utilisée pour évaluer plus finement à quel potentiel la dégradation commençait. Les films minces de ZnO non texturés présentaient une stabilité mécanique nettement améliorée et une activité ORR plus élevée par rapport aux films texturés. Un mécanisme de réaction a été proposé pour l'ORR. Ce modèle a permis d'établir quantitativement que la réduction directe est majoritaire sans que la réduction indirecte puisse être négligée. Il a été possible de démontrer que la réduction indirecte ne s'arrêtait pas à la production de peroxyde d'hydrogène et que ce dernier était ensuite réduit en ions OH<sup>-</sup> et/ou décomposé en molécules d'oxygène.

Magnetron sputtered ZnO layers: Synthesis, characterization and oxygen reduction investigations

**Keywords :** zinc oxide, sputtering, oxygen reduction reaction

**Abstract:** Corrosion is a local electrochemical process involving an oxidation reaction that is balanced by a reduction reaction. The oxygen reduction reaction (ORR) is one of the major cathodic reactions in corrosion. The oxygen can be reduced directly into OH<sup>-</sup> ions or indirectly with hydrogen peroxide as intermediate species. In this Ph.D. thesis, ORR has been investigated on ZnO that is one of the most common degraded forms of zinc, a metal of major industrial interest. Model electrodes (textured and non-textured ZnO films) have been deposited on copper substrates using the RF-sputtering technique. The ORR has been investigated in alkaline electrolyte using a rotating ring-disk electrode.

During the measurement of the polarization curves, potential-dependent rupturing of the textured ZnO films was observed. Electrochemical impedance spectroscopy was utilized to detect more finely at which potential the rupture of the film was initiated. Non-textured ZnO thin films exhibited a significantly improved mechanical stability and higher ORR activity compared to textured films. A reaction mechanism was proposed for ORR. The prevalence of the direct reduction was quantitatively established but the parallel indirect reduction was active as well. It was possible to show that indirect reduction pathway did not stop at the production of hydrogen peroxide. The latter was further reduced to OH<sup>-</sup> anions and/or decomposed into oxygen molecules.